PULSED FLOW JET IMPINGEMENT COOLING: EVALUATION OF HEAT TRANSFER PERFORMANCE

by

Michael Hamman

A Thesis Submitted in

Partial Fulfillment of the

Requirements for the Degree of

Master of Science

in Engineering

at

The University of Wisconsin-Milwaukee

December 2017

ABSTRACT

PULSED FLOW JET IMPINGEMENT COOLING: EVALUATION OF HEAT TRANSFER PERFORMANCE

by

Michael Hamman

The University of Wisconsin-Milwaukee, 2017
Under the Supervision of Professor Ryoichi Amano

This thesis presents findings from an experimental and numerical investigation into merits of pulse coolant flow as an improvement to impingement cooling. A series of simulations were conducted at Re=12k and 30k for frequencies up to 20Hz and amplitude ratios up to 70% of mean mass flow and standoff and nozzle spacing equal to three diameters. Square waveforms were found to degrade at low frequencies near 1Hz, rendering the use of square waveforms as an invalid mass flow specifications for inlet boundaries in computational predictions. The Power Consumption Ratio is introduced for comparing pulse and steady flow configuration's energy consumption. Pulse flow was found to decrease heat transfer efficiency for Re=12k, 30k which becomes more pronounced with increase in pulse configuration. Compressibility was shown to decrease the heat transfer efficiency the heat transfer efficiency for increased amplitudes for Re=30k.

To

Jesus Christ

TABLE OF CONTENTS

LIST OF FIGURES

LIST OF TABLES

ACKNOWLEDGMENTS

First, I thank God for giving me the opportunity to pursue graduate studies in mechanical engineering. His love and grace along the way has enabled me to coupe with setbacks and difficulties during my research. He has graciously provided me with encouragement through family and friends (both in and out of academia) during my research.

I thank my advisor, Dr. Ryoichi Amano, for suggesting, funding, and guiding this research. I am also grateful for my many lab and class mates who have encouraged and inspired me during some of my challenging times and cheered me in my achievements.

My family for their love, prayers and encouragement. I could not have completed my research without them. I am also thankful for their many notes, cards, and jokes they sent to cheer me and keep me in good spirits.

I am thankful for my friends that loved, encouraged, and inspired in so many ways. I am especially thankful for my church family at East Side Baptist Church for their love, prayers and encouragement.

Specially thanks to all my instructors who contributed to my development in my undergraduate and graduate studies leading to this research. I specifically highlight the late Dr. Jan Vandever, my first college instructor and a big inspiration and encouragement in my academic pursuits.

I. Introduction

This thesis presents experimental and numerical research which evaluates the merit of pulse coolant flow as a modification to jet impingement cooling. A review of applicable literature is presented flowed by a definition of the pulse jet impingement problem and the limit to which this research seeks to address the merit of pulse impingement cooling.

A. Literature Review

1. Uses of Jet Impingement Heat Transfer

Jet impingement heat transfer is an efficient heat transfer method used in electronics, food processing, paper pulp drying, and turbine engine cooling among other industrial applications. Its usage as a heating and cooling mechanism is due to its high convection transfer rates.

2. Gas Turbine Cooling

In gas turbine technology coolant is supplied from the turbine's compressor and feed into the cooling system for the respective component. The coolant temperature for air coolant is typically around 600^{o}C whereas turbine blade and similar componets may experience gas temperatures near 1400^{o}C. This requires high heat transfer rates to provide adequate cooling of critical components [1].

3. Flow Characterization

Jet impingement achieves high heat transfer rates in the stagnation region of the impinging jet [2]. The heat transfer rates decrease spatially as the distance from the stagnation point increases. In jet impingement heat transfer studies, typically the following parameters are controlled to observe their influence on heat transfer: standoff distance, nozzle spacing, nozzle configuration, nozzle sizes, nozzle shape, and nozzle Reynolds number. The flow of an impingement jet is characterized by a potential core region protruding from the nozzle where

the flow profile is largely influenced by the nozzle. In this region, the jet retains high velocity. In the region near the nozzle the nozzle flow isis considered to be a free jet due to low momentum transfer to the surrounding fluid with shear forces degrading the jet core. Near the impact surface, the jet expands due to the stagnation at the impact surface as the impinging fluid seeks to navigate around the surface [2]. This region is referred to as the stagnation region. A wall jet forms as the coolant navigates away fromt the stagnation location. Figure 1 is a velocity vector plot from a realizable k-ε simulation from a mesh convergence study supporting this research. The overlaid annotation illustrates flow characteristics generally observed in jet impingement research.

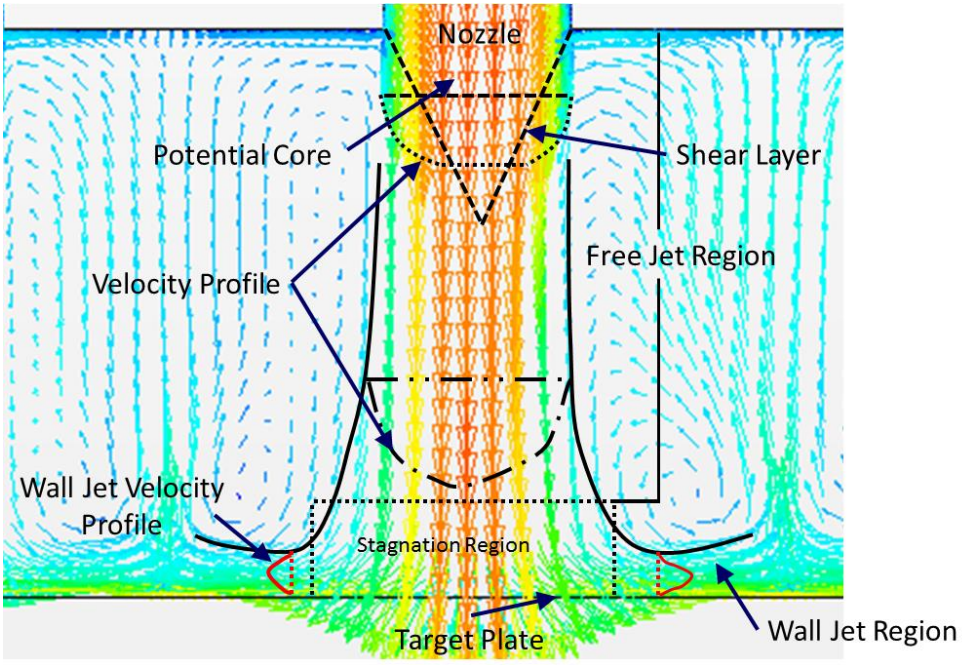

Figure 1: Jet impingement flow behavior illustration; velocity profile and flow region definition

The potential core is observed until approximately 4-6 standoff to nozzle diameter ratio [2]. Flow confined by the presence of nozzle plate or similar geometry is shown to enhance the potential core length by 7% [3]. The local Nusselt number for a single circular jet is seen to be

nearly independent of standoff distance at radial distances greater than 4.5 nozzle diameters distance from the stagnation point [4].

4. Special Conditions Influencing Jet Impingement Flow and Heat Transfer Behavior

Compressibility

Goodro et al [5] studied impingement with the Reynolds number up to 60k and Ma to 0.74, standoff distance equal to three diameters, and nozzle spacing of 8 diameters. These results showed inconsistency with Nusselt number empirical prediction relationships for increased Ma and Re flows. The inconsistencies are likely due largely to misapplication of dimensional analysis in the jet impingement heat transfer community. A new empirical model for Nusselt number dependence on Reynolds number for a specified Mach number little insight into the influence of compressibility on jet impingement cooling was gained. Vinze et al investigated the influence of compressibility on heat transfer performance for single impingement with Mach numbers of 0.3, 0.5, and 0.7 [6]. Incompressible Nusselt number correlations were found to under predict the Nusselt number for stagnation region. A correlation using a Mach number power correction was used to adjust the Nusselt number prediction for extention to incompressible flows. Liu and Feng simulation study into influence of position and Mach configuration on internal cooling of rotor blade leading edge. Their study considered Mach numbers up to 0.7 and found consistent increase in heat transfer with increase in Mach number [7].

Impingement Arrays

Multiple studies in the effect of arrays of nozzles on impingement heat transfer focusing on temperature ratio, nozzle configurations, and transient coolant flow among other parameters.

Espsoito investigated the effect of cross-flow on the heat transfer rate by introducing geometric modifications to reduce the reduction of stagnation Nu by cross-flow [8]. This research flow ranged Re=20k-60k with varied nozzle spacing and standoff distance. Qualitatively, extended ports and corrugated walls were seen to mitigate the effects of cross-flow on stagnation Nu. Schroder et al. explored experimental steady flows effects on jet impingement cooling [9]. This study focused on flows with mass-averaged Re=4k-15k with single and bi-directional flow exit configurations. Steady flow results from a 55-nozzle apparatus indicate the presence of flow instabilities creating a variation of impingement surface contact position. Coolant amplitude showed the negligible effect on time-averaged Nu for low to moderate amplitudes. For high coolant amplitudes degradation was observed for the time-averaged Nu as compared to steady flow Nu. Hai-yong et al. explored the aerodynamics of impingement cooling of staggered arrays in a semi-confined channel [10]. For Re=10,25, 65k cross-flow was found to deflect the downstream jets thereby decreasing the effect of the impingement cooling. Flow dynamics show sensitivity to standoff distance with increase in effect with increase in standoff distance to three diameters. The flow response to standoff distance decreases as standoff approaches five diameters. The discharge coefficient distribution showed decrease with downstream progression due to low standoff distance.

Staggered Arrays

Hai-yong et.al explored the aerodynamics of impingement cooling of staggered arrays in a semi-confined channel [10]. Cross-flow was found to deflect the downstream jets thereby decreasing the effect of the impingement cooling. Lee et el investigated the effect of crossflow on staggered impingement arrays [11]. This research investigated impingement flow ranging Re=8-

50k, standoff distance 1.5-8 diameters, nozzle spacing up to 30 diameters. They concluded for low Reynolds flows, Re=8k, and large nozzle spacing x/d≥30 with y/d=5 and H/d=5 the stagnation Nu influence on averaged Nu decreases. This was also seen for large x/d, Re=20, 30, and 50k with 1.5D standoff. Examination of flow and geometric parameters of this studies shows the jet average velocity is held constant for most cases while the diameter is increased to increase the Reynolds Number. For a given standoff increasing Re while holding the jet velocity constant results in increased area for jet and crossflow interaction making the jet more susceptible to crossflow affects than lower level Re configurations.

Pulsated Flow

Pulsation is also known to affect the heat transfer characteristics of jet impingement [12], [13]. Zimmer, Rutledge, and Knieriem studied pulsation effects at several Reynolds numbers with a frequency of 1Hz and a standoff distance to nozzle diameter ratio of 3. From these studies, several parameters remain to be optimized for maximizing the pulsation benefit of impingement cooling. Among these are the pulse frequency and amplitude. Pakhomov & Terkhov investigated single jet impingement with a square waveform using RSM turbulence model. The standoff ratio varied 1-10, frequency 0-60Hz, Re,ave=4.6(10^3-10^4), and a duty cycle of 0.5. Their research found a decrease in stagnation Nu for frequencies less 5Hz [14]. Mohammandpour et al. investigated the effects of intermittent (square waves), and sinusoidal pulse flows on heat transfer for a single impingement jet on a concave surface using RNG k-ε [15]. Their study showed no enhancement in the stagnation region with local enhancement due to increased turbulence intensity moving radially from the stagnation point. Womack et al

investigated pulse coolant jets for film cooling. For Strouhal numbers of 0.15, .03, and 0.6 they found the presence of pulsed flow not to provide heat transfer enhancement [16].

Power and Pressure Considerations

The most common treatment of system input requirements for impingement flows has been the production of discharge coefficents [5], [17], [18] . Serveral researchers have gone further to evaluate the pressure loss of their impingement schemes, [10], [19], [20], [21]. The static pressure drop approach gives a measure of input cost of impingement flows but still does not give a comprehensive description. Can et al attempted to formulate the input power required for jet impingement flows [21]. The power consumption formulation include only static pressure component of the mechanical energy and did not account for the inertial required to accelerate the flow to the desired flow configuration. For steady flow configurations the omission of the nonviscous requirements of impingement systems is not major issue. If the flow in nonsteady or is expected to cycle frequently the accounting of the inertial requirements of the system becomes increasingly important.

B. Defining the Pulse Impingement Cooling Challenge

The achievement of increased thermal efficiency is clearly the goal in jet impingement research. It is insufficient for a qualitative increase in heat transfer efficiency due to the introduction of pulse coolant to justify the implementation of pulse cooling in gas turbine technologies. The following observations are made to illustrate the quantitative requirements that must be addressed if pulse coolant flow in jet impingement cooling is to be established as a viable cooling method:

1. Pulse impingement cooling must demonstrate a significant quantifiable increase in heat transfer efficiency. Measurable in the sense, that experimental and numerical predictions report temporal area averaged heat transfer representations. The heat transfer efficiency increase must be significant such that the realizable increase accounts for the system consequences of employing pulse instead of steady coolant.
2. Pulse impingement cooling introduces increased geometric and mechanical effects on the heat transfer system:
    a. The presence of the hardware creating the pulse waveform introduces additional drag forces on the flow system requiring either an increase in operating pressure or a reduced friction flow system. Since the pressure in the case of gas turbines is driven by the pressure requirement for turbine operation, a flow system must be constructed that requires special material or an increase in geometric space.
    b. The pulse generation mechanism requires precious design space and presents an additional failure mechanism.
3. The pulse generation mechanism presents additional manufacturing and maintenance lifecycle costs.

This research attempts to address the merit of pulse jet impingement cooling at temporal averaged flows of Re=12,000 and Re=30,000 with frequencies 0-20Hz and pulse amplitudes 0-70%. The geometric characteristics of equal nozzle spacing and standoff distance of 3D for a diameter D=4.76mm. The method for addressing pulse jet impingement coolant flows is as follows:

1. Develop experimental methods with prescribed data analysis.

2. Develop dimensional evaluation parameters.
3. Prescribe simulation methods.
4. Develop appropriate mass inlet boundary conditions.
5. Present steady and transient simulation studys with comparison to experimental results
6. Present and discuss Simulation results.

A discussion is given on the relevance of published experimental and simulation results followed by a summary of the resulting conclusions of this study.

II. Methods

The following is a discussion of the development of the experimental apparatus and methods, general evaluation methods, uncertainty, simulation methods, and pulse flow boundary specification.

A. Experimental

This section describes the experimental apparatus, methods, and data analysis used in generation and evaluation of the experimental data used for validating the CFD mesh and physical treatment for CFD results presented by this study. First, the apparatus is presented, followed by an energy analysis of the apparatus impingement zone, and an experimental procedure is given for mitigation of experimental error sources.

1. Overall System

The test system simulates jet impingement through impinging coolant air on a heated stainless steel foil surface. The impinging jets strike the heated surface orthogonal to their initial direction of flow. The impinged coolant air migrates through a confined channel out two symmetrical exits into the ambient shop atmosphere. Figure 2 gives an overview of the testing system.

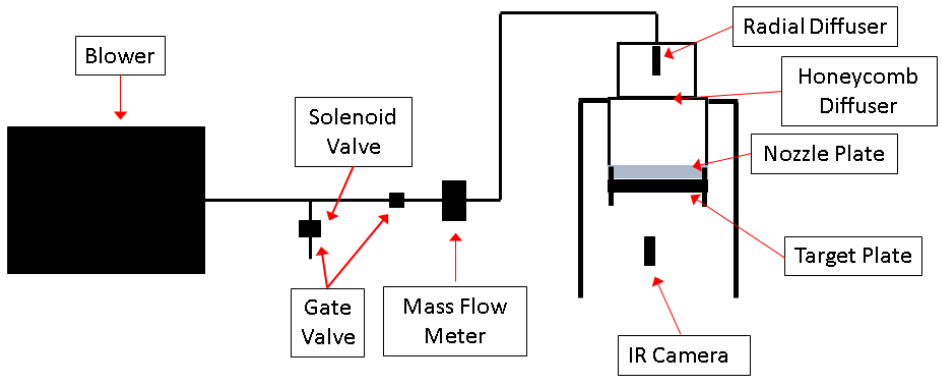

Figure 2: Coolant system

Jet impingement cooling can be classified per the order of flow confinement. Jet impingement flows always involve an impingement surface; the flow may also be confined along the plane of origin or radially from the direction of flow. In this experiment, partially confined flows will be considered where the flow is confined along the nozzle plate and two parallel surfaces forming a bi-directional impingement channel, Figure 3.

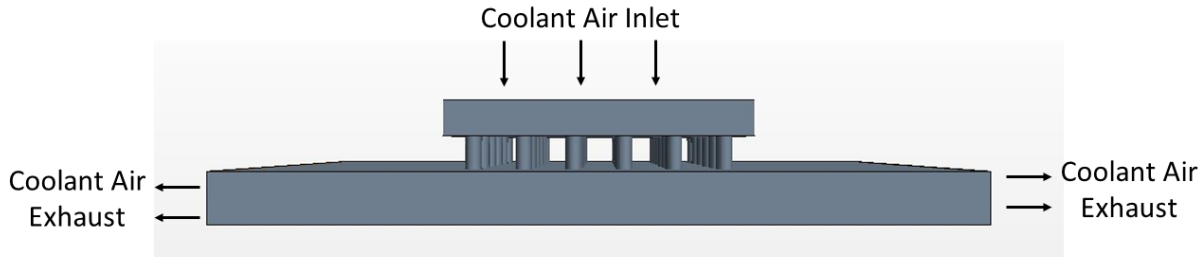

Figure 3: Symmetric exhaust configuration

Figure 4 depicts the physical interaction of the test domain. H and D are the standoff distance and nozzle diameter respectively.

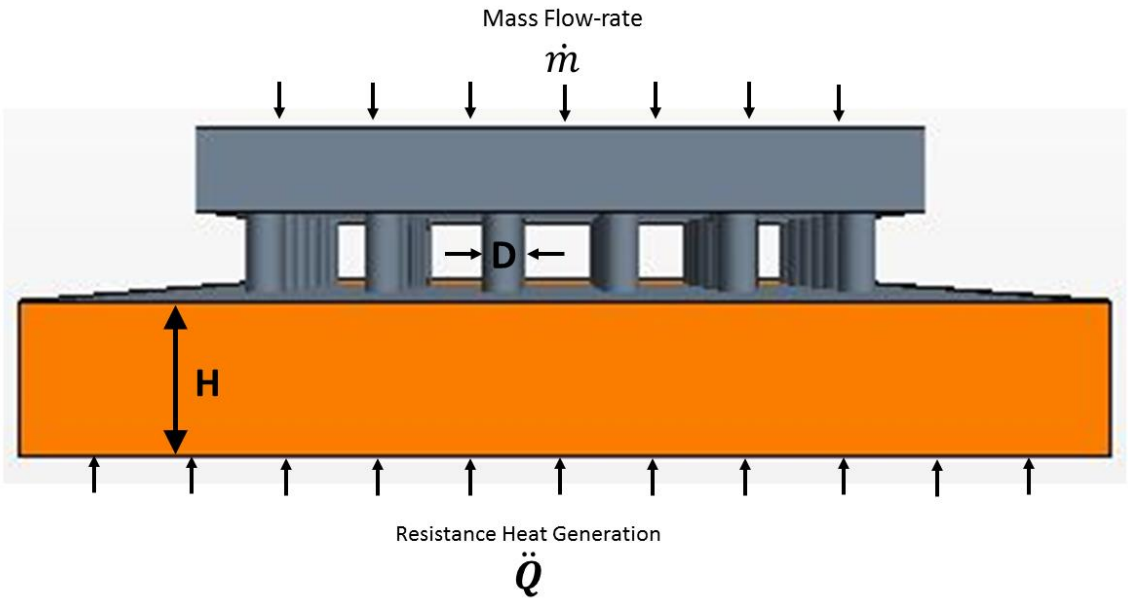

Figure 4: Experimental parameter definition

Heat Source and Measurement System

The apparatus employs an indirect heat source utilizing resistance heating by passing electrical current through the impingement surface. This method allows for simple measurement of thermal generation by means of measuring the voltage drop across an electrical current flowing through the impingement surface. A schematic of the electrical layout is given in Figure 5.

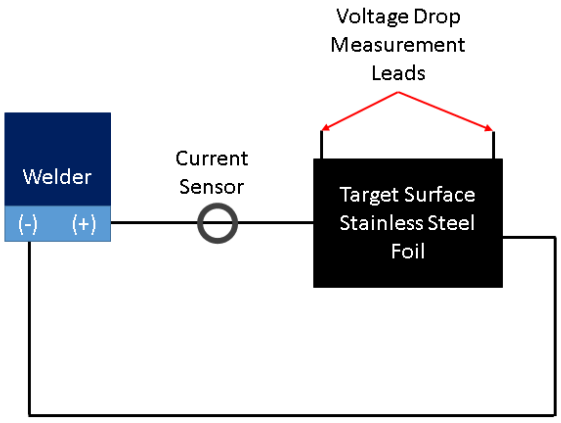

Figure 5: Heat source power circuit schematic

Power was supplied using Amico Power DC-160A welder inverter allowing selection of target currents. The current was measured using a Hall Effect Current sensor provided by Flex-Core, CTL-101/50. The sensor signal was condition using Flex-Cores CTA201. The output signal was collected using an NI 9215 DAQ card. The voltage drop was measured by soldering electrical leads to the impingement surface and connecting the remaining ends to the NI 9215 DAQ card. A LABVIEW code was created to record the current and voltage drop signals for post-processing. A sampling rate of 1-1.2k/s was used to accurately resolve the signal waveforms for both the current and voltage drop. The power leads were connected to bus bars in an effort to distribute the current along the foil clamp interface. Figure 6 shows a view of one exhaust exists. The foil tensioner pretensions the foil in attempt to mitigate deflection of the foil while under thermal and jet loading during the experiment.

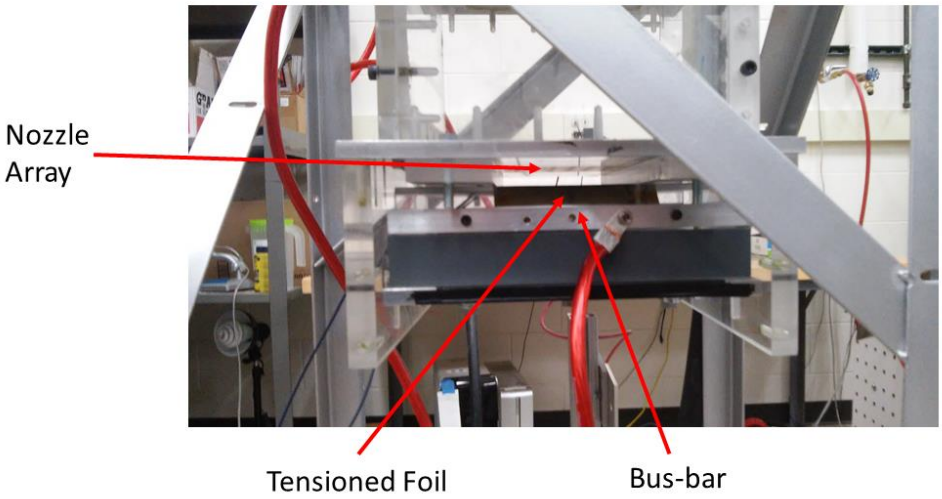

Figure 6: Test Section; electrical power connection

Impingement Surface

Stainless steel foil (304 SS) was used for the impingement surface due to its' high electrical resistivity which leads to moderate thermal generation. The foil is painted with KRYLON ULTRA-

FLAT black paint on one surface to provide a high emissivity distribution for capturing the foil temperature distribution with the Infrared camera. The ULTRA-FLAT black paint is Acrylic based and provides a high emissivity. The paint was applied to a premeasured area that was cleansed using Isopropyl Alcohol. Several coats were applied to create a uniform distribution. The paint was inspected visually using a light source to ensure no unpainted surface was present. The electrical leads for the voltage drop were soldered to the underside of the foil at marked locations outside the Infrared Imaging area. The dimensional parameters as indicated in Figure 7 were measured and recorded for post-processing. The current and voltage drop through and across the foil is measured for establishing the heat transfer characteristics of the respective impingement configuration. Figure 7 shows the three critical areas of measurement. L1 & L2 may be recorded for a foil configuration. L3 & L4 may also be recorded for a foil surface but require the camera being configured to capture the geometric definition for assigning area values to the pixel distribution. This method was employed for the assignment of heat flux per pixel.

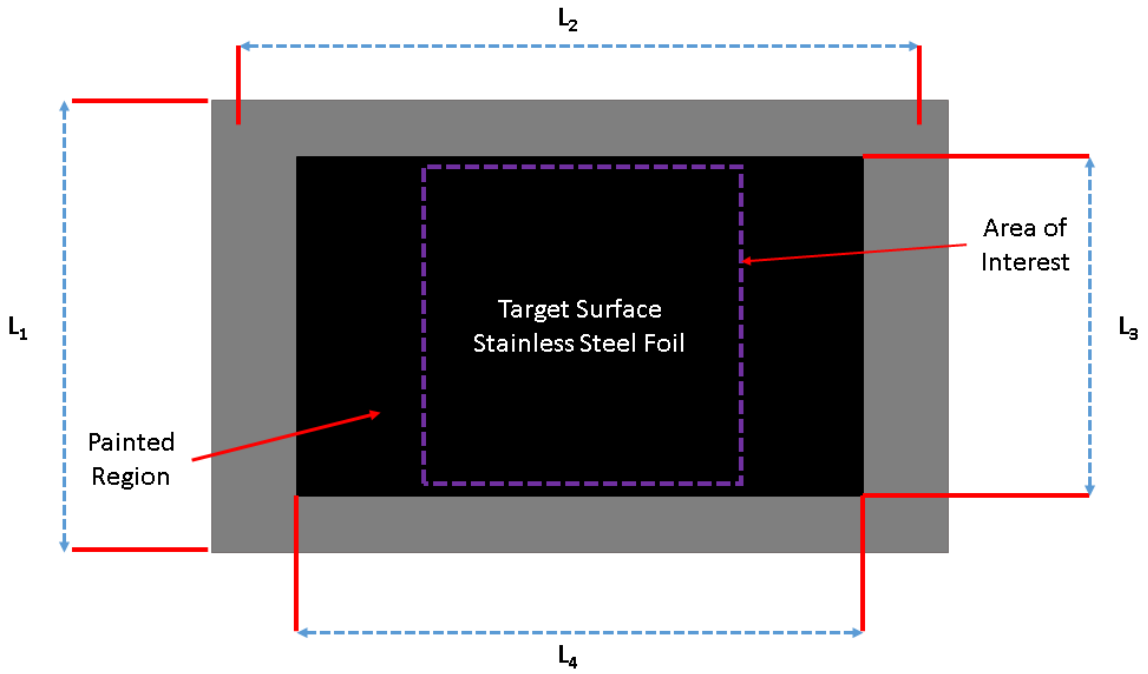

Figure 7: Target surface heat source analysis dimensions

Infrared Imaging

FLIR's A35 thermal imaging system and ResearchIR 3.0 software were used to capture thermal plots of the temporal behavior of the underside of the impingement surface. The following procedures/provisions were implemented to provide accurate temperature distributions;

1. A semi-stationary mounting system was constructed to provide uniformity in position and orientation.
2. Calibration for image distortion was performed for post-processing of experimental images. Details of camera calibration are given in section VII Appendix A.
3. Emissivity was calibrated for the actual test surface.
4. The lens was cleaned per manufacturing instructions prior to data collection [22].

Coolant Measurement and Control

The coolant air is supplied from a centrifugal blower with air intake from a shop atmosphere. The mean mass flow-rate is controlled using and gate valve upstream of the mass flow meter. Excess air is discharged from the system to achieve the desired mean mass flow-rate. For pulse flows the waveform is obtained by discharging air from the system through a solenoid valve. The valve is controlled using an Arduino board and a relay board sending square wave signals to the solenoid valve.. The wave amplitude is controlled by adjusting a gate valve downstream of the solenoid valve. As indicated in Figure 2, the mass flow rate was measured downstream of the solenoid valve system so that the flow behavior of the impinging jet could be more accurately represented. The mass flow rate was measured using ALICAT SCIENTIFIC's M-5SLPM-D/5M flow meter. The mass flow, temperature, and pressure output were recorded using LABVIEW 2015 software and a manufacturer's customizable code.

2. Energy Balance

In jet impingement cooling applications, a finite heated surface is cooled by the impingement of coolant air through means of forced convection. The geometric and thermal characteristics of the impingement surface present influence the heat transfer behavior of the jet impingement system. This research considers a fundamental impingement configuration with a smooth impingement surface that is orthogonal to the jet's direction. The development of methods for analyzing the experimental data begins with a representation of the heat transfer configuration as shown in Figure 8. Forced convection, $\dot{q_{fc}}$ provided by impinging jets and coolant cross flow is transferred from the upper surface of the foil.

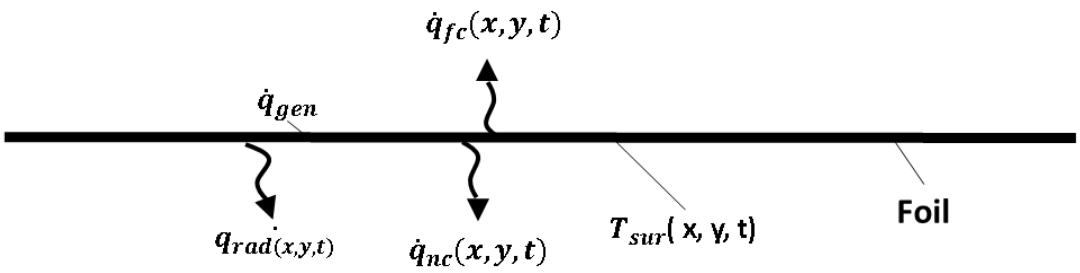

Figure 8: Heat transfer diagram for heated foil

Natural convection, $\dot{q_{nc}}$, occurs on the underside of the foil due to gravitational effects on the ambient air. The temperature distribution, $T_{sur}(x, y, t)$, results from the heat transfer response to the heat generated, $\dot{q_{gen}}$, by the electrical current flowing through the foil. A small but important component of the heat transfer is the radiation from the foil, $\dot{q_{rad}}$. Beginning with the assumption of a sufficiently thin foil for target such that the effect of a thermal gradient between the upper and lower surfaces and 2D heat transfer analysis may be performed for the foil. This assumption was validating through performing a lumped sum analysis for the foil and upper lower convective surfaces. The analysis showed Bi>0.1 indicating no appreciable temperature gradient exists in the heated foil. Figure 9 gives the local heat transfer balance on a elementary or pixel volume basis.

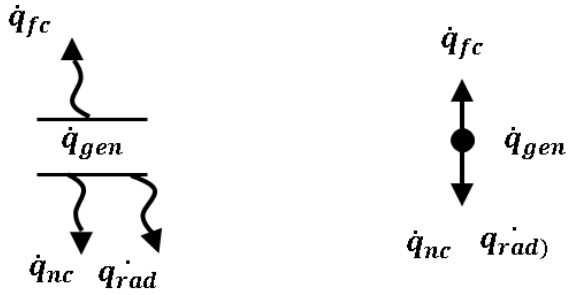

Figure 9: Local heat transfer balance

The energy balance on the foil is written as, equation (1).

$$\frac{dE}{dt} = \dot{q}_T + \dot{q}_{\text{gen}} \tag{1}$$

Where the time derivative for E is the internal energy of the foil and subscripts T and gen are, the total heat transferred through the surfaces and thermal generation respectively. Expanding the total heat transferred through the surfaces first into upper and lower surfaces, and then into the individual heat transfer components is given equation (2).

$$\dot{q}_T = \dot{q}_u + \dot{q}_l = \left[\dot{q}_{rad,U} + \dot{q}_{FC}\right] + \left[\dot{q}_{rad,L} + \dot{q}_{NC}\right] \tag{2}$$

Since Joule heating is used to provide the heating effect the thermal generation is given as, equation (3).

$$\dot{q}_{\text{gen}} = \Delta V * \frac{I}{L_1 L_2} \tag{3}$$

Where ΔV and I are, the voltage drop across the target and the current flowing through the target plate respectively.

Natural Convection and Radiation

Radiation and natural convection were calculated using known correlations. Nusselt number for natural convection was calculated using an empirical correlation for horizontal surfaces with lower side cooling presented by [23], and is valid for Ra of (10^5,10^{11}) equation (4).

$$Nu = 0.27 * Ra^{1/4} \tag{4}$$

Where Ra is the Rayleigh number given by equation (5).

$$Ra = \frac{g * \beta * (Ts - T\infty) * Lc^3}{v^2} * Pr \tag{5}$$

Where g, β, T_s, T_∞, L_c, P_r, and υ are the gravitational constant, thermal coefficient of air, foil surface temperature, global ambient temperature, foil dimensional length, Prendtl number of air, and kinematic viscosity of air. $\dot{q}_{NC}$ is then calculated using equation.

$$\dot{q_{NC}} = h_n * (Ts - T\infty) \tag{6}$$

Where the coefficient of natural convection transfer is written as (7)

$$h_{nc} = \frac{Nu * k}{Lc} \tag{7}$$

With the conduction coefficient of air k. The natural convection coefficient h is calculated using equation (8)

$$Nu, nc = \frac{hD}{k} \tag{8}$$

Radiative heat transfer occurs on the lower and upper surfaces of the impingement surface. The radiative flux through the lower and upper surfaces of the impingement foil on a local (pixel) basis is given in equations (9) and (10) respectively.

$$\dot{q_{rad,L}} = A_p \sigma \varepsilon_{sur} (T_{sur}^4 - T_{inf}^4) \tag{9}$$

$$\dot{q_{rad,\ U}} = A_p \sigma \left(\frac{1}{\varepsilon_{sur}} + \frac{1}{\varepsilon_n} - 1 \right)^{-1} (T_{sur}^4 - T_n^4) \tag{10}$$

Where A_p, σ, ε_{sur}, and ε_n are the pixel area, Stefan-Boltzmann constant, and emissivity of painted surface. Ts, Tinf, and Tn are the foil, ambient, and nozzle plate temperatures respectively.

Forced Convection Flux

The forced convection flux is found through applying quasi-equilibrium to the equation (1) , substituting equation (2) into equation (1), and solving equation (1) for the heat flux transferred to the coolant flow through forced convection, equation (11).

$$\dot{q}_{FC} = \dot{q_{gen}} - \dot{q}_{rad,L} - \dot{q}_{rad,U} - \dot{q}_{NC} - \frac{dE}{dt} \tag{11}$$

Where the time derivative for the internal energy of the foil is neglected due to preliminary analysis which showed changes in averaged temperature over the data collected resulted in a negligible change in thermal energy, a fraction of the average thermal energy removed through convection. This is intuitive since the target temperature was raised to reach operating temperature before thermal imaging began. Additionally, the impingement was conducted at steady coolant conditions for the steady-state case and at 1Hz for a pulse case which was averaged over several cycles.

3. Procedure

The assembled apparatus and subsystems are evaluated to ensure proper testing operation and reduce experimental error:

1. Coolant System. The coolant system connections are examined while the blower is operating to ensure no air leaks occur downstream of the mass flow meter. The solenoid valve pulsation is initiated, and flow measurements are taken. The mass flow data is examined to ensure the wave frequency corresponds to the programed microcontroller frequency.
2. Heat Source and Measurement System. Power is supplied to the apparatus and measurements of the current and voltage drop are recorded. The recorded data is evaluated to ensure the desired current is recorded.
3. Thermal Imaging System. The imaging system is permitted to warm up for a minimum of 5 minutes per manufacturer instructions. The imaging parameters are inputted into ResearchIR software interface including emissivity, lens to impingement surface distance, atmospheric temperature, and relative humidity. The real-time image is examined to ensure the target features are properly captured.
4. The target plate. The foil is heated to above the testing temperature, and then the current is removed. The tensioning bolts are tightened until the foil experiences a pretension force sufficient to keep the foil from deflecting during the testing operation.

The following sequence is used for data collection:

1. Coolant System manipulation. The coolant system is set to the respective mean Reynolds number, frequency, and wave amplitude.

2. The Heat Source adjustment. The current is slowly adjusted until the stagnation temperatures reach the desired testing temperature (min of 25k above ambient temperature).
3. Data Recording.
    a. Initialization
        i. Heat Source
        ii. Mass Flow
        iii. Thermal Imaging
    b. Stopping. The system is permitted to cycle for a minimum of 5 cycles after the Thermal Imaging recording begins before beginning the shutdown process.
        i. Thermal Imaging
        ii. Mass Flow
        iii. Heat Source
4. Apparatus Shut-Down. The current supply is removed before shutting down the coolant system. A minimum time lag of 30 seconds following removing the current before shutting down the coolant system to allow the apparatus to cool down.
5. Image Processing. The images were analyzed using a MATLAB, [24], a script developed through the course of this research and is described in section VIII, Appendix B.

B. Dimensional Analysis Treatment

1. Flow Characterization –Reynolds Number

To establish the Reynolds number in the experiment, the total mass flow through the impingement jets nozzles was measured, and then jet Reynolds number was calculated based on the total number of jets and jet impingement nozzle area as showed below.

$$Rej = \frac{4 * \dot{m}}{N * \pi * \mu * D} \tag{12}$$

Where $\dot{m}$, N, μ_a, and D the total mass flow rate of all impinging jets, number of jets, dynamic viscosity of air, and the nozzle diameter.

2. Nusselt Number Definition

How the Nusselt number is defined is of immense importance. Formally Nu is the ratio of the convective heat transfer to the idealized conductive heat transfer that would occur if the fluid were static and only conductive heat transfer occurred. Typically, Nu is defined as equation (13).

$$Nu = \frac{hl}{k} \tag{13}$$

Where l is a characteristic dimension of the system. Though often this is a good representation of the convective and conduction relationship there are cases where the system is complex and convective heat transfer is influenced by many different parameters. In these cases it is not always easy to set a standard Nu definition, or the research has been tainted with the tradition of using a diameter for the characteristic dimension when it should not be used. Jet impingement cooling is such a complex heat transfer field where it is no longer acceptable to define Nu in such an elementary way without considering the consequence of the definition. Use of standard Nu with the diameter as the characteristic dimension leads to skewed or bias

in data representation towards the impingement system with the larger diameter. Paz and Jubran point this out in their simulation work in turbine vane impingement cooling [25]. To illustrate this point consider the work of Goodro et el [5] which investigates jet impingement array cooling for Mach number and Reynolds number influence. As part of the study, the Mach number is held constant while Re is increased by increasing the diameter of the nozzles and the mass flow rate. In this part of the analysis two Nu numbers were compared to see the effect of Re. Two configuration with Re=6400, 8200 with D=3.5,4.5 (mm) respectively and held at Ma=0.1 by means of constant average velocity. The problem is by changing the diameter from D=3.5mm to 4.5mm the Nu numbers no longer represent the same relationship between convection and conduction. The Nu for the 4.5mm will now have nearly a 28.6% bias towards reporting a higher Nu. While the Nu plots given for the variation in Nu showed perhaps a 15% increase in heat transfer efficiency the increase is less than the bias and consequently show a 13.6% decrease in effective heat transfer efficiency.

To avoid or limit fallacious interpretation of jet impingement data a different and more adequate Nu model is needed. The following attempts to remove some of the inaccuracies through developing a new Nu model. Beginning with the definition of the Nusselt numer as given in equation (14).

$$Nu = \frac{Convective\ Heat\ Transfer}{Conductive\ Heat\ Transfer} = \frac{\dot{q_{conv}}}{\dot{q_{condu}}} \tag{14}$$

Since the convective heat transfer is measure through experiment or simulation results a formulation of the system's ideal conductive heat transfer is need for statisfying the Nu definition. The idealized conduction may clearly be defined when considering the impingement

domain and imaging the non-existence of the nozzles. Figure 10 shows an ideal representation corresponding to the removal of the nozzles. In this idealization the coolant in the impingement is brought to a rest such that no convective heat transfer occurs. No radiative heat transfer is considered to occur in the channel and uniform coolant properties exist throughout the fluid channel. Considering the system to reach an equilibrium the temperature profile from the impingement surface to the nozzle plate will be linear.Typically, the idealized lower temperature is constructed assuming T_L to be uniformly equivalent to the T_j.

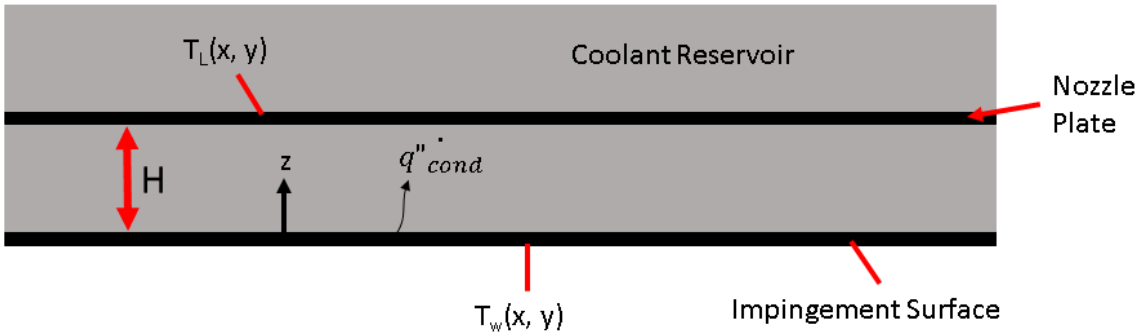

Figure 10: Conduction idealization

The conductive heat transfer law is envoked in flux form and is given as equation (15).

$$\dot{q_{cond}} = -k\frac{dT}{dz} \tag{15}$$

Since the temperature profile in the impingement channel is linear the gradient with respect to z direction will be constant. This permits the separation of the temperature profile gradient variables and integration with respect to position and temperature as given in equation (16). The integrated result is given in equation (17) and after evaluation at the taget surface and nozzle plate the conduction is given in equation (18).

$$\int_{z=0}^{z=H} \dot{q_{cond}} dz = -\int_{T=T_w}^{T=T_j} k dT \tag{16}$$

$$\dot{q_{cond}} z|_0^H = -kT|_{T_w}^{T_j} \tag{17}$$

$$\dot{q_{cond}} = \frac{k(T_w - T_j)}{H} \tag{18}$$

After inserting the conduction formulation in equation (18) into equation (14) and rearranging the new Nu formulation for jet impingement is given as equation (19).

$$Nu = \frac{\dot{q_{fc}}}{\dot{q_{cond}}} \frac{\dot{q_{fc}}}{\dot{q"_{cond}}} = \frac{\dot{q_{fc}}}{-\frac{k(TL-Tw)}{H}} = \frac{H\dot{q_{fc}}}{k(Tw-TL)} \tag{19}$$

Addapting this Nu model corresponds to the observed change in heat transfer performance due to increase or decrease of standoff distance. Additionally, using the standoff distance permits the easy comparison of heat transfer results from impingement sytems with nozzle diameter variation, array type, spacing variation, and flow type among other parameters with limited scaling. For a specific case with constant nozzle diameter Nu be rewritten through acknowledging the relationship of H and D. Since H = 3D for this research, Nu becomes, equation (20). The conductive coefficient k, is evaluated at the bulk fluid temperature which is defined as the average of jet temperature and the average target surface temperature.

$$Nu = \frac{3D\dot{q_{fc}}}{k(Tw - TL)} \tag{20}$$

Where equation (20) is defined, and computed directly for simulation studies, and calculated during post experimental data processing for experimental cases.

3. Accounting for Influence of Thermal Capacity – Stanton Number

The Nu number gives a basis for evaluating the effectiveness of jet impingement cooling through comparison to static conduction. While this provides a level of usefulness for

measuring the merit of heat transfer configurations it falls short of providing a basis for evaluating the effectiveness of convective heat transfer in its' actual configuration. The Stanton heat transfer number fills this evaluation gap by comparison of the heat transferred to the fluid to the thermal capacity of the fluid flow. For this study, a global Stanton (Sta) number is defined as, equation (21).

$$Sta = \frac{Nu}{Re * Pr} \tag{21}$$

Where Nu and Re are obtained using equations (20) and (12) respectively. The Prandtl number, *Pr*, is taken at bulk fluid temperature taken as the average of the jet and mean impingement temperatures.

4. Representing the Vortex Behavior – Strouhal Number

Jet impinging flows are known to have complex flow structures including vortex generation, enhancement, and pairing. The Strouhal number (Str) provides a means of evaluating the flow system in regard to its' oscillatory behavior. The Strouhal number is given as, equation (22).

$$Str = \frac{f * L}{U} \tag{22}$$

Where f is vortex shedding frequency, L is the characteristic length, and U is the characteristic velocity. In pulse impingement research f is typically treated as the pulse/mass flow frequency, L is set equal to D, and U is the mass averaged nozzle velocity.

5. Heat Enhancement Ratio

The heat transfer enhancement ratio is the ratio of the temporal /area average Nu for the pulse flow case to the temporal/area average Nu for the steady flow condition.

$$ER = \frac{Nu_p}{Nu_s} \tag{23}$$

Where subscripts p and s indicate pulse and steady flow conditions respectively.

6. Power Consumption Ratio

It is no longer acceptable to evaluate jet impingement heat transfer systems merely on the basis of the efficiency at the heat transfer surface. Jet impingement flows are complex with pressure drops associated with frictional losses unique to the expansion of coolant through nozzles. The frictional losses require minimal flow energy be supplied to the system to support the impingement cooling. Elementarily the increase in fluid velocity increases the frictional losses of any flow system. With the addition of pulse, coolant flows in jet impingement it is increasingly important to consider the energy requirements since the pulse peaks have higher velocities and corresponding pressure losses. Compounding the higher velocity issue is the high accelerations due to the small-time step with each wave cycle. The Power Consumption Ratio (PCR) is introduced to account for this gap and provide a comprehensive picture of jet impingement efficiency. PCR represents the ideal change in mechanical power required to produce a pulse flow jet impingement system. The PCR is defined relative to the respective steady flow configuration for the mass mean Re level and is given in equation (24).

$$PCR = \frac{W_p}{W_s} \tag{24}$$

Where W_p and W_s are the required power for the pulse and corresponding steady impingement configurations. The work for each configuration is defined as equation (25).

$$W_i = \dot{m}_i * \left(\frac{\Delta P_i}{\rho_{ave}} + \frac{{v_i}^2}{2}\right) \tag{25}$$

Where ΔP, $\dot{m}$, v_i, and ρ_{ave} are the maximum measured pressure drop (magnitude), mean mass flow rate, maximum inlet velocity, and coolant density at maximum mass flow rate respectively. The index i specifies the individual flow configuration either steady or pulse flow. The maximum measured pressure drop occurs at the peak mass flow rate is used since the periodic reduction in mass flow is caused by periodic upstream pressure losses. This would indicate that the maximum measure pressure drop best represents the minimum required head loss for producing the pulse flow. The inlet velocity, v_i, is calculated from the mass flow rate using equation (26).

$$v_i = \frac{\dot{m}_i}{\rho A} \tag{26}$$

C. Uncertainty Analysis

The error for Nu was computed using the perturbed method for single sample experiments as presented in equation (27), [26].

$$\delta Nu = \{\sum_{i=1}^{N} (C_i)^2\}^{1/2} \tag{27}$$

Where C_i is the difference of the reference Nu and the perturbed Nu and is given in equation (28

$$C_i = Nu_o - Nu_i \tag{28}$$

The parameters monitored during the experimental for the Re=2070 steady flow experimental case are given in Table 1.

Table 1: Experimental directly measured parameters for Nu uncertainty

Experimental Measured Parameters

D (m)	A_p (m^2)	L_1 (m)	L_2 (m)	T_s (k)	T_j (k)	T_∞ (k)	V (V)	I (A)	L_c (m)	ε_p (-)

Manufacturer calibration uncertainties were used for when provided. Conservative estimates were used for individual parameters when uncertainties were not given. The resulting approximation of uncertainty in Nu was calculated to be nearly 4.0%. Neglecting the uncertainty in dynamic viscosity the uncertainty in Re may be derived analytically as, equation (29) [17].

$$\delta Re = \left[\left(\frac{4}{\pi * N * D * \mu} * \delta\dot{m}\right)^2 + \left(-\frac{4\dot{m}}{\pi * N * D^2 * \mu} * \delta D\right)^2\right]^{1/2} \quad (29)$$

Where $\delta\dot{m}$ is the uncertainty in the mass flow rate as specified by the manufacturer and δD is the uncertainty of the nozzle diameter given through a conservative estimate. The resulting uncertainty in Re is 2.7%.

D. Simulation Methods

This section describes the geometric, numerical, and physics modeling of the experimental setup.

1. Geometric Conditions

The computational boundaries are given in Figure 11.

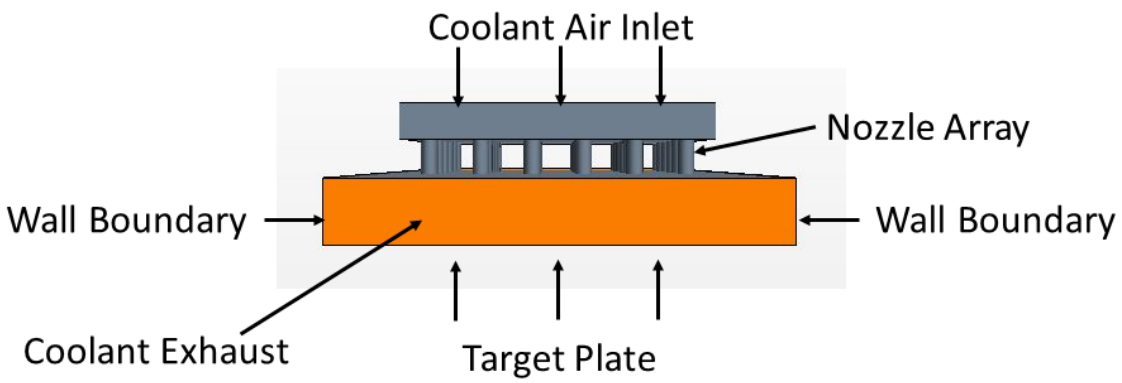

Figure 11: Computation domain diagram

Figure 12 gives the boundary conditions for mesh study. The coolant air inlet was treated as a mass flow inlet allowing the velocity profile to develop through the nozzle region.

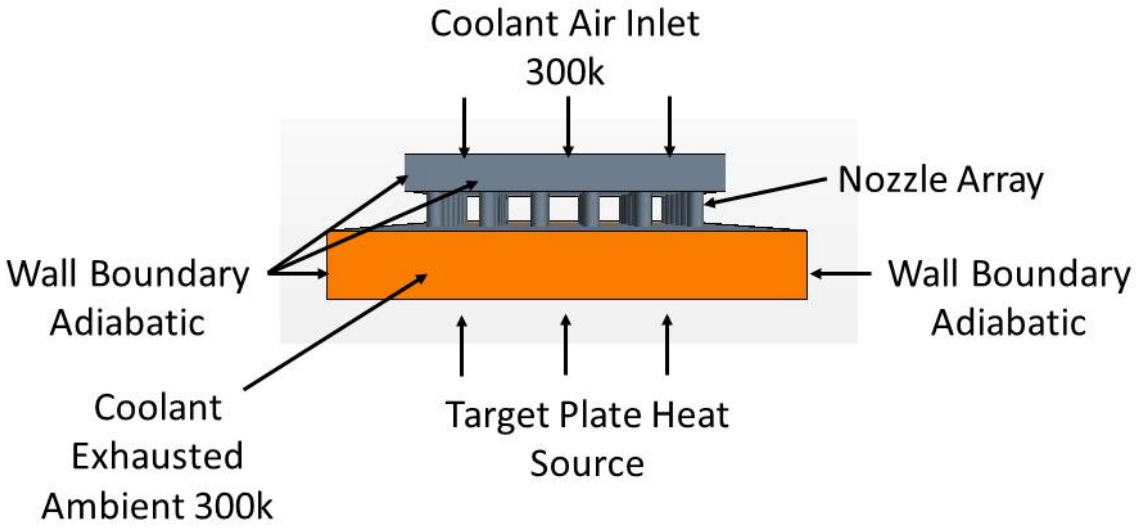

Figure 12:Simulation boundary conditions

2. Mesh Conditions

Trimer and prism layer mesh models were used to discretize the computational domain. Figure 13 shows the typical mesh definition. The geometry was meshed using StarCCM+ 11.04.012 internal mesher.

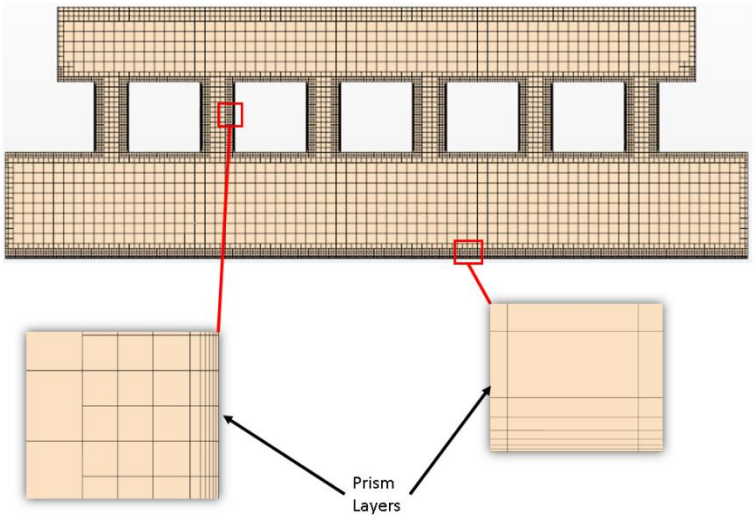

Figure 13: Mesh scheme (4) description

3. Turbulence Modeling

StarCCM+ 11.04.012 [27] was used to model the turbulence and heat transfer interaction of the jet impingement study cases for this research. The Unsteady Reynolds Stress Model with blended elliptical wall treatment was employed for turbulence modeling.

Reynolds Stress Transport Equation

The transport equation for the specific Reynolds stress tensor, $\boldsymbol{R} = \overline{v'v'}$ is given in equation (30).

$$\frac{d}{dt}\int_v \rho \boldsymbol{R} dV + \int_A \rho \boldsymbol{R}(v - v_g)\cdot da = \int_A D \cdot da + \int_V \left[\boldsymbol{P} + \boldsymbol{G} - \frac{2}{3}\rho \boldsymbol{I}\gamma_M + \underline{\emptyset} + \underline{\epsilon} + \boldsymbol{S_R}\right] dV \tag{30}$$

Where the terms on the right-hand side are diffusion D, turbulent production **P**, buoyancy production **G**, turbulent dissipation $\underline{\varepsilon}$, dilation dissipation γ_M, pressure strain $\underline{\Phi}$, and the specified source $\mathbf{S_R}$,. For the linear Pressure Strain and Quadratic Pressure Strain models, the dissipation is represented as equation (31).

$$\underline{\varepsilon} = 2/3\rho\mathbf{I} \tag{31}$$

Reynolds Stress Diffusion

The Reynolds-Stress Diffusion is modeled assuming isotropic turbulent diffusion and given in equation (32).

$$D = \left(\mu + \frac{\mu_t}{\sigma_k}\right)\nabla \boldsymbol{R} \tag{32}$$

Where the turbulent Schmidt number is σ_k=0.82 and the turbulent viscosity is computed as equation (33).

$$\mu_t = \frac{\rho C_\mu k^2}{\varepsilon} \tag{33}$$

With the turbulent kinetic energy *k* defined as equation (34).

$$k = \frac{1}{2} tr(\boldsymbol{R}) \tag{34}$$

The Generalized Gradient Diffusion Hypothesis formulation is shown in equation (35).

$$D = \mu\nabla \boldsymbol{R} + C_s \tau(\boldsymbol{R}\cdot\nabla)\boldsymbol{R} \tag{35}$$

Where C_s=0.2 and τ=k/ε.

Turbulent Production

The turbulent production is obtained using equation (36).

$$P = -\rho(\boldsymbol{R} \cdot \nabla \boldsymbol{v}^t + \nabla \boldsymbol{v} \cdot \boldsymbol{R}^T) = -\rho(\boldsymbol{R} \cdot \nabla \boldsymbol{v}^T + \nabla \boldsymbol{v} \cdot \boldsymbol{R}) \quad (36)$$

Buoyancy Production

For constant density flows the Boussinesq approximation is used to model the buoyancy production as given in equation (37).

$$G = \beta \frac{\mu_t}{\sigma_t} (\boldsymbol{g} \otimes \nabla T + \nabla T \otimes \boldsymbol{g}) \quad (37)$$

Where β is the coefficient of thermal expansion, g is the gravitational vector, σ_t is the turbulent Prandtl number, and ∇T is the temperature gradient vector. For flows with varying density the buoyancy production is given by equation (38).

$$\boldsymbol{G} = \frac{\mu_t}{\rho \mu_t} (\boldsymbol{g} \otimes \rho + \nabla \rho \otimes \boldsymbol{g}) \quad (38)$$

Where $\nabla \rho$ is the density gradient vector.

Turbulent Dissipation Rate

The isotropic turbulent dissipation rate is obtained from a transport equation analogous to the K-Epsilon model (and with identical boundary conditions) as given in equation (39).

$$\begin{aligned} &\frac{d}{dt}\int_V \rho \varepsilon dV + \int_A \rho \varepsilon (v - vg) \cdot da \\ &\quad = \int_A \left(\mu + \frac{\mu_t}{\sigma_t}\right) \nabla \varepsilon \cdot da \\ &\quad + \int_V \left\{\frac{\varepsilon}{k}\left[C_{\varepsilon 1}\left(\frac{1}{2} tr(\boldsymbol{P}) + \frac{1}{2} C_{\varepsilon 3} tr(\boldsymbol{G})\right) - C_{\varepsilon 2} \rho \varepsilon\right]\right\} dv \end{aligned} \quad (39)$$

Where $C_{\varepsilon 1}$ and $C_{\varepsilon 2}$ are specified coefficients and $C_{\varepsilon 3}$ is determined as in the Standard K-Epsilon model. The coefficient $C_{\varepsilon 1} = 1.44$. The coefficient $C_{\varepsilon 2} = 1.92$ when the linear pressure-strain

term is used, and has the value 1.83 when the quadratic pressure-strain term is used. A two-layer formulation, which solves for k but prescribes ε algebraically with distance from the wall, is available for use with the linear pressure-strain model. Which is identical to the two-layer formulation using in the K-Epslion models.

Dilatation Dissipation Rate

The dilation dissipation Y_M is modeled as in the K-Epsilon model and is given in equation (40).

$$\Upsilon = \frac{C_M k\varepsilon}{c^2} \tag{40}$$

Where c is the speed of sound and C_M=2.

Linear Pressure-Strain Model

The linear model (Gibson and Launder) for the pressure-strain term comprises five terms; these are the rapid part, the slow part, and their respective wall-reflection terms are given in equation (41).

$$\underline{\Phi} = \underline{\Phi}_s + \underline{\Phi}_r + \underline{\Phi}_{r,b} + \underline{\Phi}_{1w} + \underline{\Phi}_{2w} \tag{41}$$

The slow pressure-strain term$\underline{\Phi}_s$ is modeled as in equation (42).

$$\underline{\Phi}_s = -\frac{C_1\rho\varepsilon}{k}(\mathbf{R} - \frac{2}{3}k\mathbf{I}) \tag{42}$$

The rapid pressure-strain term $\underline{\Phi}_r$is modeled in equation (43).

$$\underline{\Phi}_r = -C_2[\boldsymbol{P} - \frac{1}{3}\mathbf{I}tr(\mathbf{P})] \tag{43}$$

The buoyancy contribution $\underline{\Phi}_{r,b}$ is modeled as (44).

$$\underline{\Phi}_{r,b} = -C_3[\mathbf{G} - \frac{1}{3}\mathbf{I}tr(\mathbf{G})] \tag{44}$$

$$\underline{\Phi}_{1w} = \frac{\rho C_{1w}\varepsilon}{k}\left[(\mathbf{R}\colon\mathbf{N})I - \frac{3}{2}(\mathbf{R}\cdot\mathbf{N} + \mathbf{N}\cdot\mathbf{R})\right] f_w \tag{45}$$

Where:

$$f_w = \min\left(\frac{k^{\frac{3}{2}}}{C_{l\varepsilon}d}, f_w^{max}\right) \qquad f_w^{max} = 1.4 \tag{46}$$

d is the wall distance, and the tensor **N** is given in equation (47).

$$N = \boldsymbol{n}\otimes\boldsymbol{n} \tag{47}$$

And the wall-normal unit vector **n** is defined as negative in the wall direction.

Elliptic Blending Model

The Elliptic Blending Model blends a near-wall and quadratic pressure-strain models for the pressure-strain and dissipation and is given as, equation (48).

$$\underline{\emptyset} - \underline{\varepsilon} = (1-\alpha^3)\left(\underline{\emptyset^w} - \underline{\varepsilon^w}\right) + \underline{\alpha^3}(\underline{\emptyset^h} - \underline{\varepsilon^h}) \tag{48}$$

Where α is the blending parameter as given by equation (49)

$$\alpha - L^2\nabla^2\alpha = 1 \tag{49}$$

A quasi-linear model is used for the outer region, equation (50).

$$\begin{aligned}\underline{\emptyset^h} = {} & -[C_1\rho\varepsilon + C_{1s}tr(\boldsymbol{P}+\boldsymbol{G})]\boldsymbol{A} + \left(C_3 - C_{3s}\sqrt{\boldsymbol{A}\colon\boldsymbol{A}}\right)\rho k\boldsymbol{S} \\ & + C_4\rho k\left(\boldsymbol{S}\cdot\boldsymbol{A} + \boldsymbol{A}\cdot\boldsymbol{S} - \frac{2}{3}\boldsymbol{A}\colon\boldsymbol{S}\boldsymbol{I}\right) + C_5\rho k(\boldsymbol{W}\cdot\boldsymbol{A} + \boldsymbol{A}\cdot\boldsymbol{W}^{\boldsymbol{T}})\end{aligned} \tag{50}$$

While in the near-wall layer as given by equation (51)

$$\underline{\emptyset^w} = -\frac{5\rho\varepsilon}{k}[\boldsymbol{R}\cdot\boldsymbol{N} + \boldsymbol{R}\cdot\boldsymbol{N} - \frac{1}{2}\boldsymbol{R}\colon\boldsymbol{N}(\boldsymbol{N}+\boldsymbol{I})] \tag{51}$$

Where the wall-normal vector n, is defined by, equation (52).

$$\boldsymbol{n} = \frac{\nabla\alpha}{\sqrt{\nabla\alpha \cdot \nabla\alpha}} \tag{52}$$

The outer region dissipation rate is given as, equation (53)

$$\underline{\varepsilon^h} = \frac{2}{3}\varepsilon \boldsymbol{I} \tag{53}$$

The wall-region dissipation rate is given by, equation (54)

$$\underline{\varepsilon^w} = \boldsymbol{R}\frac{\varepsilon}{k} \tag{54}$$

The turbulent time and length scales are defined respectively as equation (55) and equation **(**56**)**.

$$\tau = \max\left(\frac{k}{\varepsilon}, C_t\sqrt{\frac{\nu}{\varepsilon}}\right) \tag{55}$$

$$L = C_l \max\left(\frac{k^{\frac{3}{2}}}{\varepsilon}, C_\eta \frac{\nu^{\frac{3}{4}}}{\varepsilon^{\frac{1}{4}}}\right) \tag{56}$$

E. Coolant Flow Response and Waveform

The influence of coolant waveforms has been studied by researchers [15], [14]. Though intermittent/square waves show excellent performance in CFD studies it is doubtful such waveforms could be accurately replicated in an empirical environment. As part of this research several sets of mass flow data were collected from this study's apparatus to evaluate waveform of pulse flow. Intermittent/square waves signal was sent to the solenoid valve controlling the coolant waveform. The mass flow meter measured the waveform downstream of the bleed-off point. Figure 14 shows the waveform for a 0.244Hz square wave signal. Note that the square wave features begin to deteriorate at this low frequency.

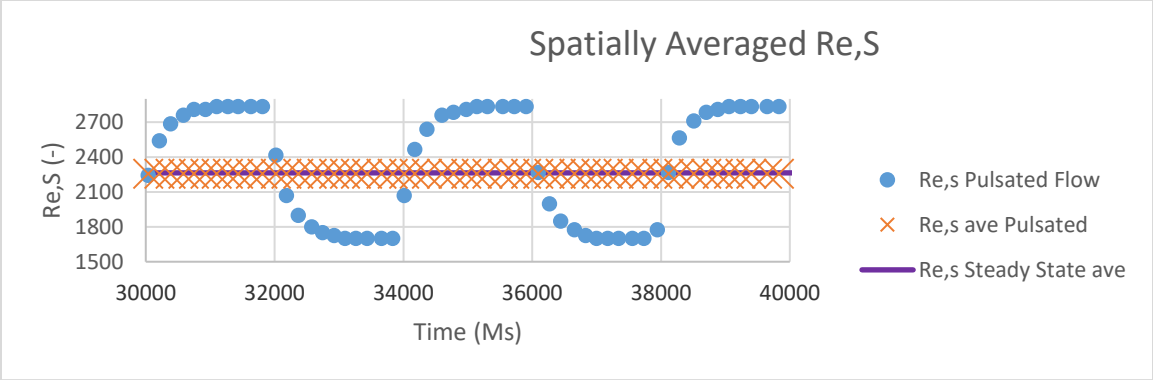

Figure 14:Fluid Response; 0.244Hz pulse frequency

As the frequency is increased to 0.5Hz the square waveform has lost most of its' features as shown Figure 15.

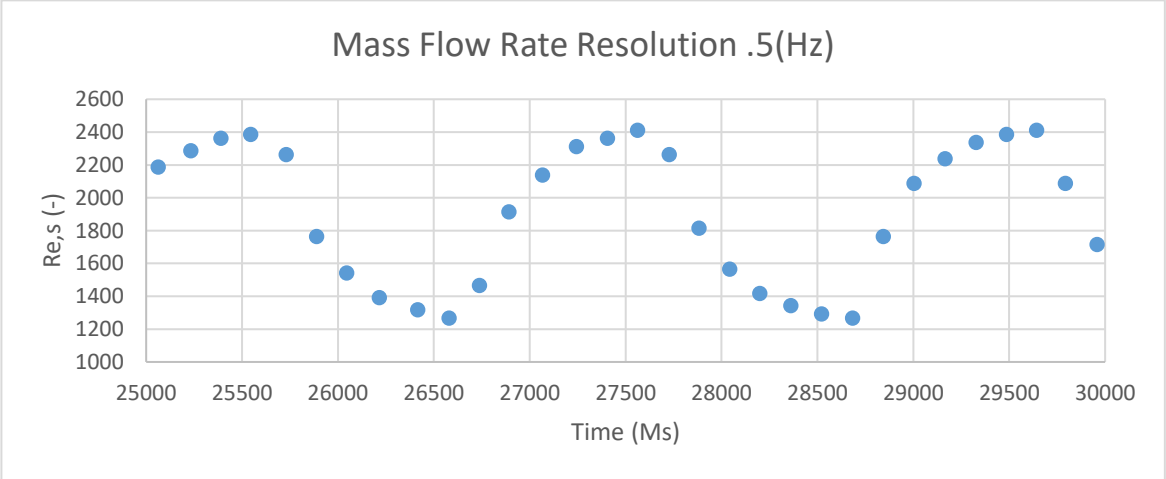

Figure 15: Fluid Response; 0.5Hz pulse frequency

The frequency is increased to 1Hz and resembles more of saw tooth wave than the intermittent signal, Figure 16.

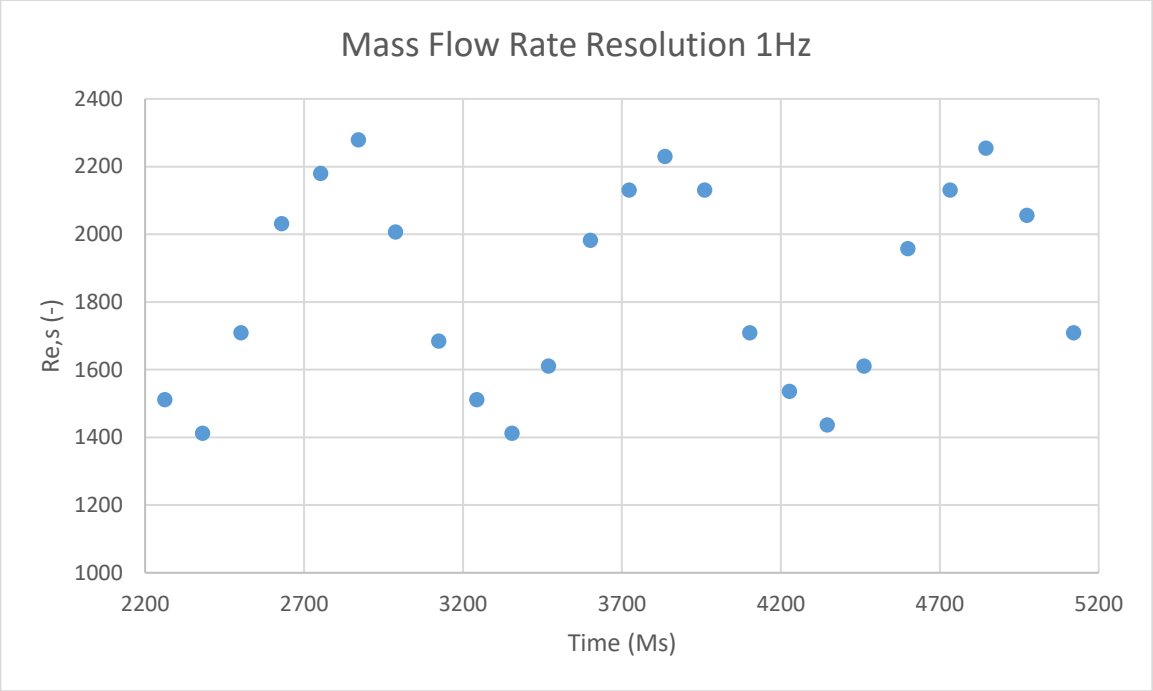

Figure 16:Fluid Response; 1Hz pulse frequency

With the rapid deterioration of the intermittent waveform a different coolant inlet waveform must be set to achieve realistic simulation results. A single wave was extracted from an 1Hz pulse mass flow data and replicated to create a typical waveform set. The waveform was curve fitted using MATLAB's Curve Fitting Toolbox [24]. A third order Fourier Series was used to fit the data set, Figure 17.

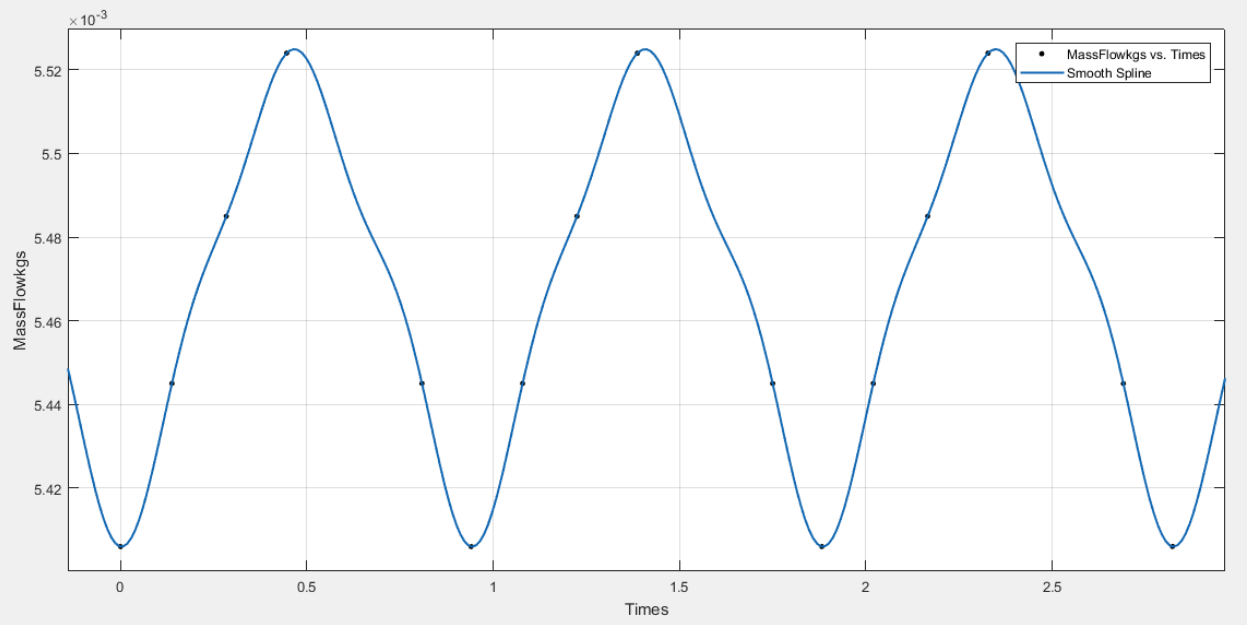

Figure 17: Third-order Fourier series fit of experimental based waveform

The resulting Fourier Series for the coolant flow is given in equation (57). The RMSE is 4.32e-18 and a goodness of fit SSE=1.497e-6.

$$\dot{m}(t) = A_0 + A_1\cos(W*f*t) + B_1\sin(W*f*t) + A_2\cos(2W*f*t) + B_2\sin(2W*f*t) + A_3\cos(3W*f*t) + B_3\sin(3W*f*t) \quad (57)$$

Where f and t are the pulse frequency and time respectively. The Fourier Series coefficients are presented in Table 2.

Table 2: Fourier Series Coolant flow representation

COEFFICIENT	VALUE	CONFIDENCE INTERVAL
A0	Specified mean coolant flow (kg/s)	NA
A1	-5.229e-5 (kg/s)	(-0.004501,0.004397)
B1	0 (kg/s)	(-0.007935, 0.007935)
A2	-4.467e-6 (kg/s)	(-0.003309,0.0033)
B2	-1.211e-6 (kg/s)	(-0.006441, 0.006438)
A3	-7.165e-6 (kg/s)	(-0.002937, 0.002923)
B3	0 (kg/s)	(-0.00156, 0.00156)
W	6.677 (rad)	(6.677,6.677)

For convenience, the pulse amplitude is referenced by a mass flow Amplitude Ratio (AR). The AR is defined by equation (58). Where $\dot{m}_a$ and $\dot{m}_m$ are the mass flow rate amplitude and mean mass flow rate respectively. $\dot{m}_a$ is defined as the maximum variance from $\dot{m}_m$.

$$AR = \frac{\dot{m}_a}{\dot{m}_m} \tag{58}$$

III. Numerical and Temporal Validation

A series of simulations were conducted using experimental conditions for validating the mesh and temporal schemes.

A. CFD Boundary Conditions

The boundary conditions are illustrated in Figure 12. The coolant mass flow rate is specified by the respective mass flow rate corresponding to the Re of the experimental test. The pulsed cased used a mass flow input generated using equation (57). Heat flux was specified at the impingement surface as given in Table 3.

Table 3: Experimental conditions for CFD boundary conditions

Re (-)	F (Hz)	va/vm (%)	q"(W/m)
2070	0	0	4620
2390	1	0.6	5796

B. Mesh and Temporal Sensitivity Study

1. Mesh Validation

A mesh scheme to accommodate high coolant flow of Re_{ave}=30,000 was developed first at the experimental conditions this study presents and then at the higher Re number case and compared to published experimental results. Table 4 gives the mesh parameters and conditions used for an initial mesh refinement study.

Table 4: Mesh scheme mesh resolution study parameters

Cases	No. Cells (-)	Base Size(-)	Target Surface Size (%)	Min Surf. Size (%)	No. Prism Layer	PL Stretch.	PL Thck. (%)	Target PL Thickness (m)	TI (%)	TL (m)
1-1	3082129	0.0016	20	15	10	1.2	10	0.00028	10	0.01
1-2	2869395	0.0016	20	15	5	1.2	10	0.00028	10	0.01
1-3	2560476	0.0017	20	15	5	1.2	10	0.00028	10	0.01
1-4	2305866	0.0017	35	20	5	1.2	10	0.00028	10	0.01

Temporal and Span-wise averaged Nu distributions for experimental and numerical cases are presented in Figure 18. A comparison with experimental span-wise averaged Nu for a jet impingement array with a steady flow of Re_{ave}=2230 by Zimmer et al. [28] shows this study's experimental span-wise averaged Nu to be acceptable. Adjusting for the difference in Nu determination Zimmer's data roughly gives a Nu range 72-84 for Nu peaks at the stagnation locations and Nu minimums near 50. Noting the reduction in a number of prism layers from 1-1 to 1-2 mesh scheme produces a negligible increase in Span-wise averaged Nu distribution the refinement due to increased prism layers does not improve the matching of experimental with predictive numerical results. Increasing the mesh base size from 1.6mm to 1.7mm results in a small reduction of in Span-wise Nu while simultaneously reducing the cell count approximately 300k. A further change in mesh conditions by increasing the target surface size and range of surface size resulted in an increase in Span-wise Nu distribution and consequently increased the difference between experimental and predictive results.

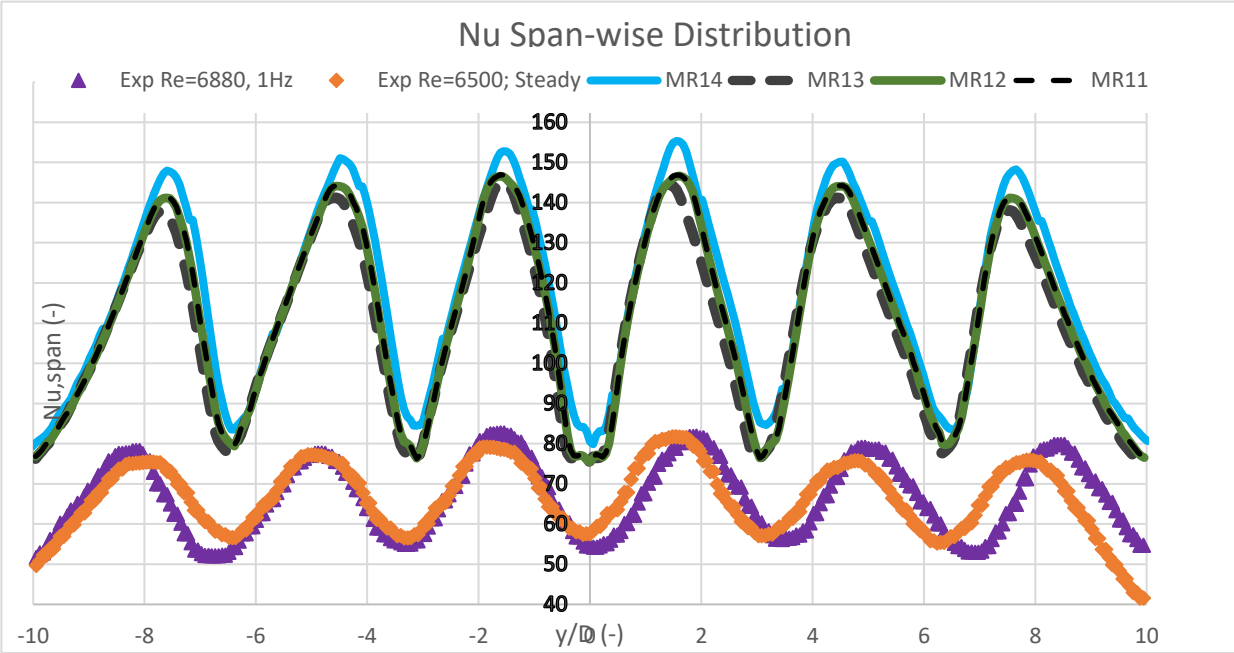

Figure 18: High Flow Mesh validation; Re=2070, Steady flow; CFD time step 5e-5 s

The 1-3 mesh configuration is chosen as the basis for further mesh refinement in the following section. Figure 19 (a)&(b) compares the temporal averaged Nu for Experimental and 1-3 simulation results. The presence of local Nu minimums is seen in both experimental and simulation. The temporal averaged Courant Number is presented in Figure 20. A maximum convective Courant Numbercourant number of nearly 0.7 which indicates sufficient temporal resolution at the target surface for resolving the heat transfer at the target surface. Figure 21 gives the y+ distribution with the maximum y+ of nearly 2.3 at Re=2070 ensures adequate resolution of the Reynolds Stress in the near wall region at the target surface. Since the y+ is proportional to the shear velocity as Re increases the y+ will also increase. Consequently, as Re is increased to mean of Re the prism layer at the target plate surface will be required to be reduced to maintain y+<3. A span-wise section plot of the Courant Number is given in Figure 22. The span-wise Courant Number distribution shown in Figure 22 gives the maximum Courant

Number less than 2 with much of the distribution near or less than value of 2. Figure 23 displays a Span-wise velocity plot with flow features including deflection of downstream jets and wall jets that rollup into entrained vortices. A Span-wise sectional view of the pressure distribution is given in Figure 24. The location of the stagnation zones are shown by the increased static pressure along the target surface. The stagnation pressure of the downstream jets decreases which correlates to the locally reduced Nu at the downstream jets as indicated in Figure 18

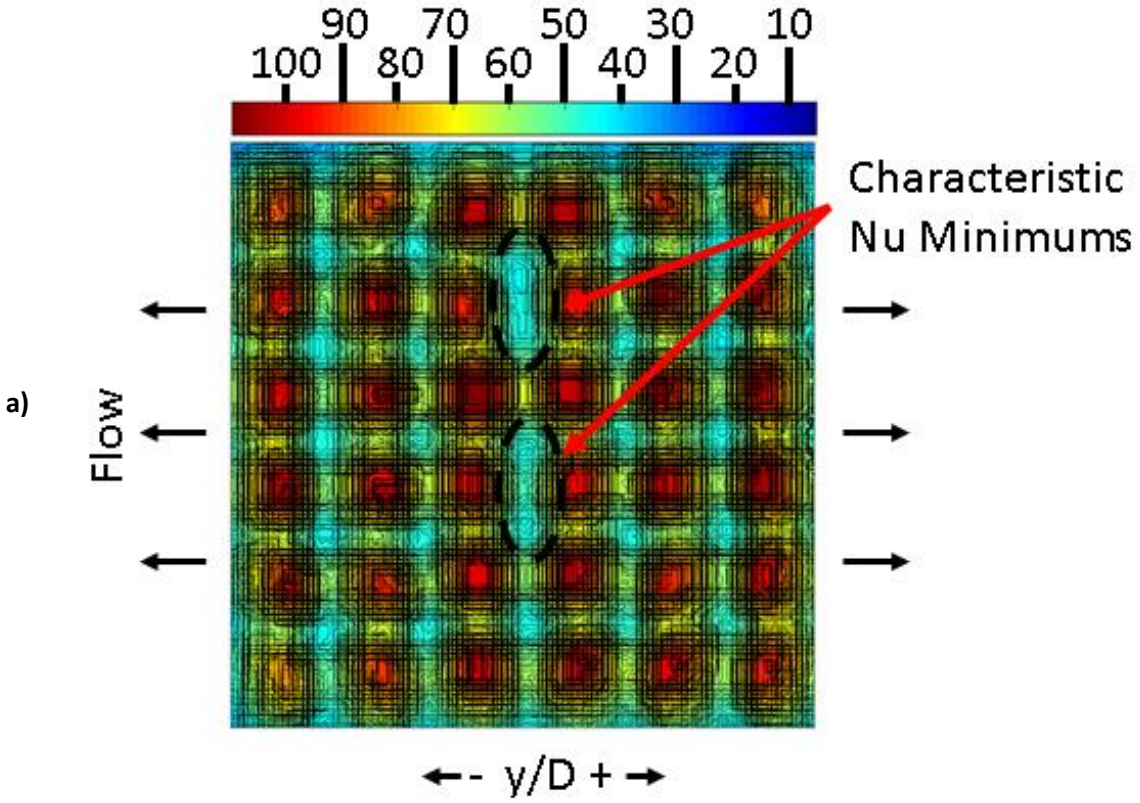

b)

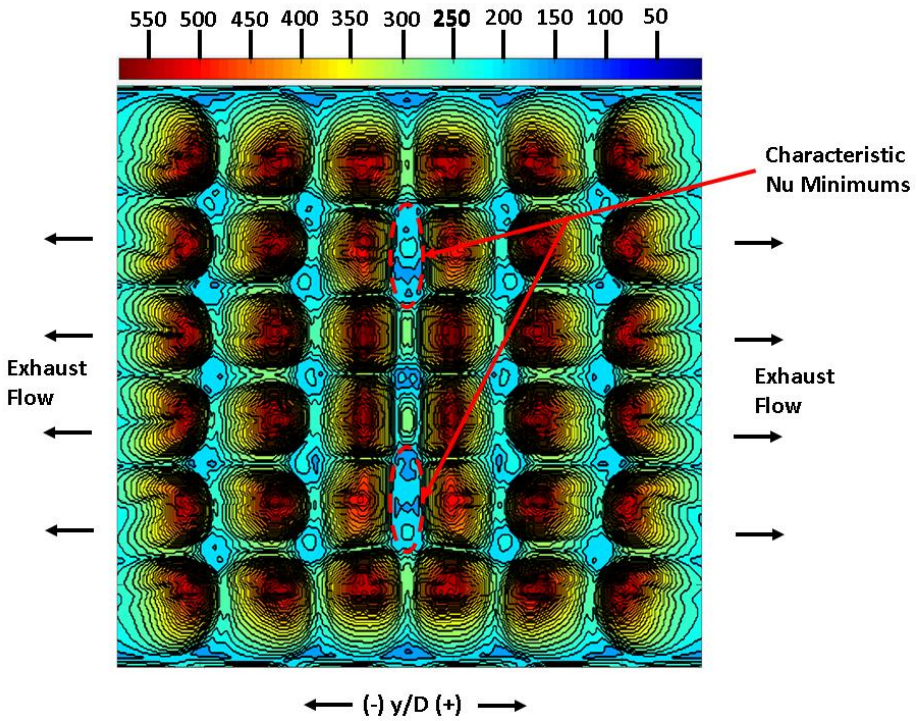

Figure 19: Comparison of Temporal Averaged Nu, Re=2070 steady coolant flow; (a) experimental, (b) CFD

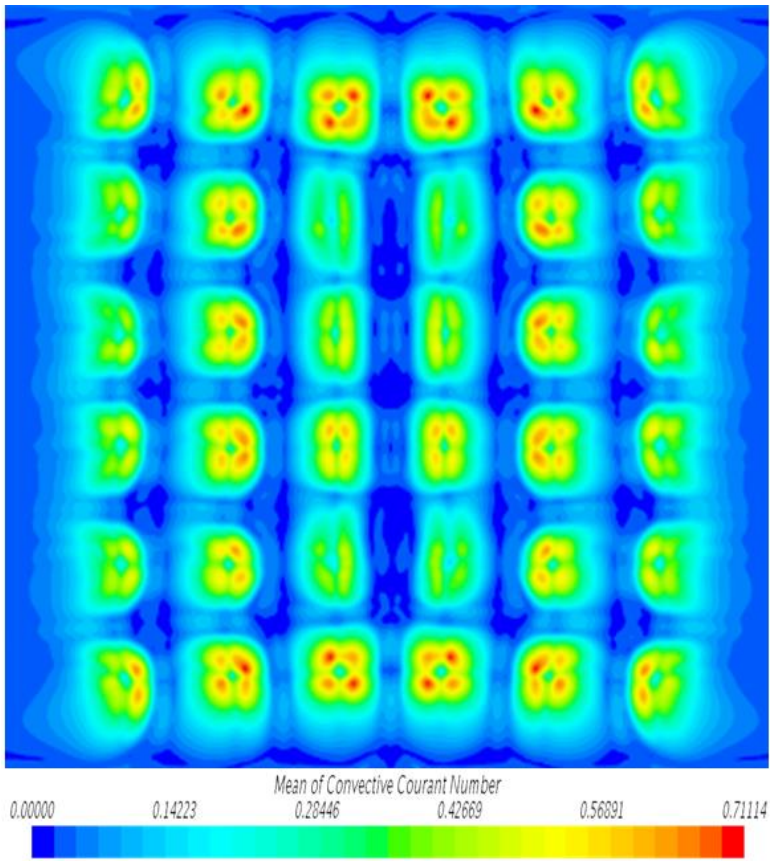

Figure 20: 1-3 time averaged Courant Number plot

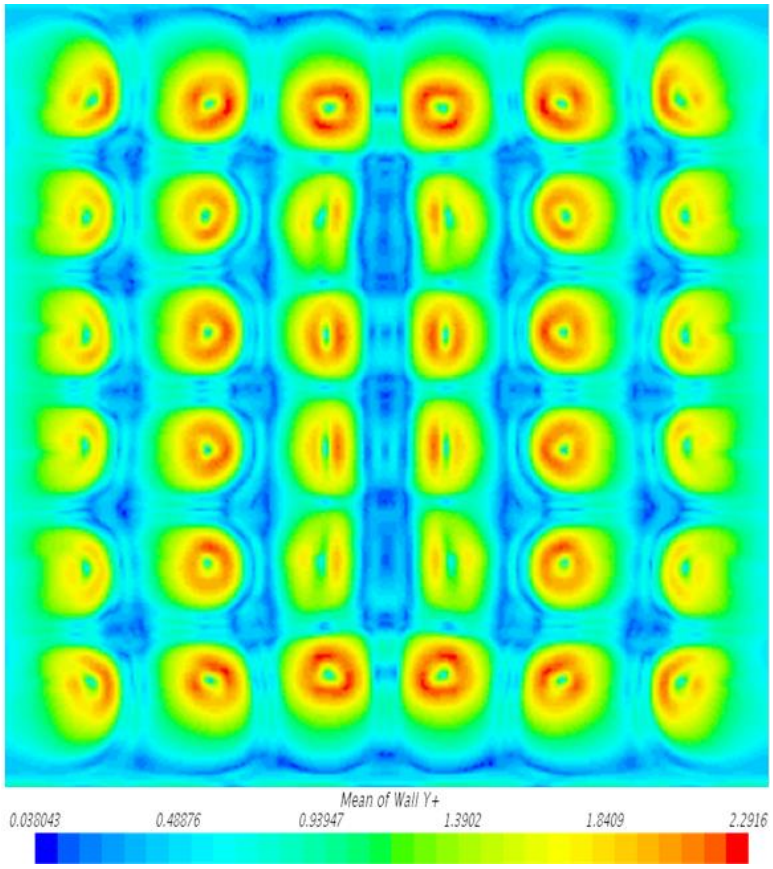

Figure 21:1-3 time averaged y+ distribution

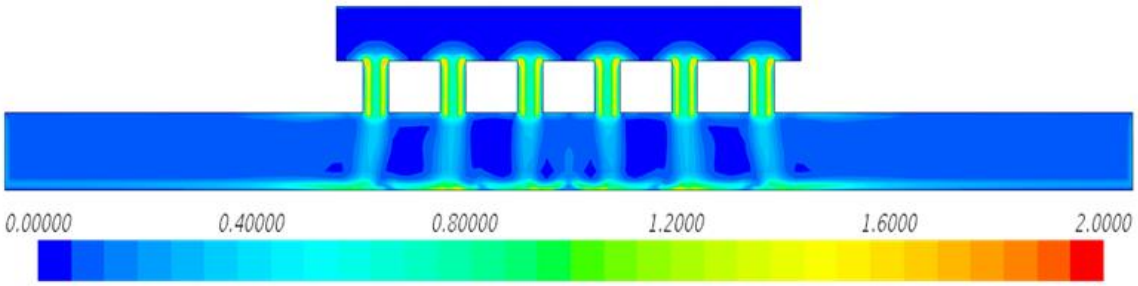

Figure 22: 1-3 sectional time averaged courant number

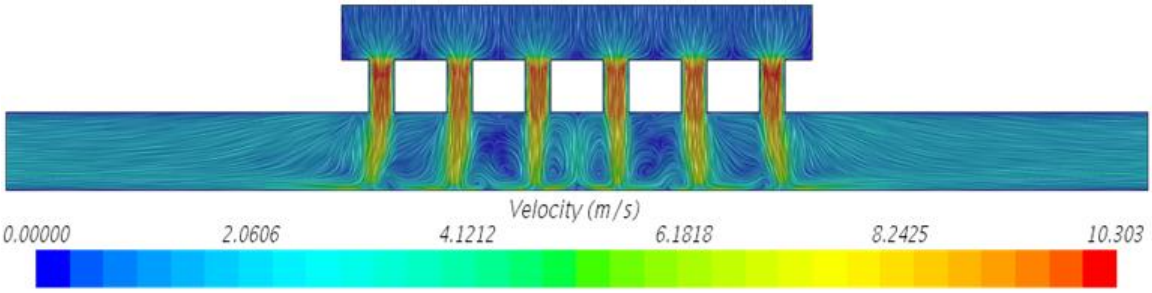

Figure 23: 1-3 Section velocity distribution

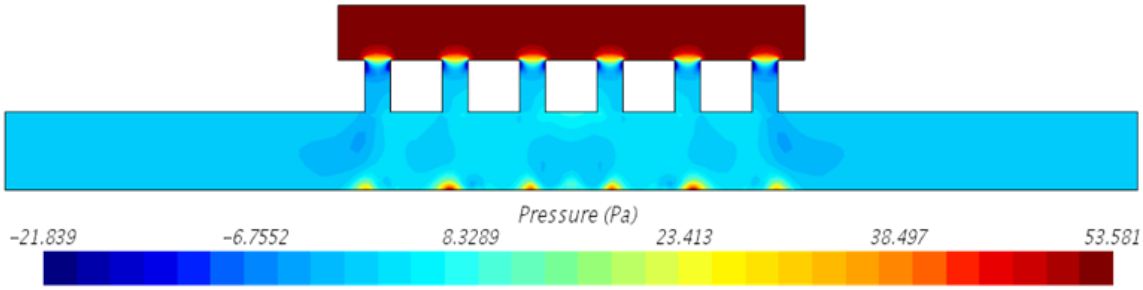

Figure 24: 1-3 Sectional pressure distribution

2. Turbulence Boundary Conditions and Material Property Refinement

Figure 25 gives a Span-wise averaged Nu distribution for further refinement of physic and numerical treatment for matching experimental results. The variations of mesh, turbulence conditions, and fluid thermal properties are given in Table 5. Simulations 2-1 and 2-2 use Turbulence Intensity (TI) and Turbulence Length Scale (TL) specification based on the inlet free stream average velocity and nozzle diameter. Increasing the mesh base size to 1.8mm from 1.7mm results in lower upstream span-wise averaged peaks compared to downstream span-wise averaged peaks as shown in Figure 25. The higher peaks observed for downstream span-wise Nu in 2-1 is not observed in this research experimental data, and therefore the increase of mesh size does not result in improved physical prediction. Reducing the TI over an order of magnitude from simulation 2-2 to 2-3 results in a negligible change in temporal and span-wise Nu distribution, therefore, turbulence intensity does not significantly influence the heat transfer prediction. A reduction of the TL by an order of magnitude in the lowering of the temporal span-wise averaged Nu in 2-4. Since some locations target plate showed elevated temperatures, nearly 100^{o}C above inlet temperature, Sutherlands Laws (SL) were used for dynamic viscosity and thermal conductivity of air. A polynomial fit for constant specific heat

was used for defining the specific heat of air. Changing the thermal properties in 2-5 resulted in increased temporal span-wise Nu distribution and consequently increased difference in prediction and experimental results.

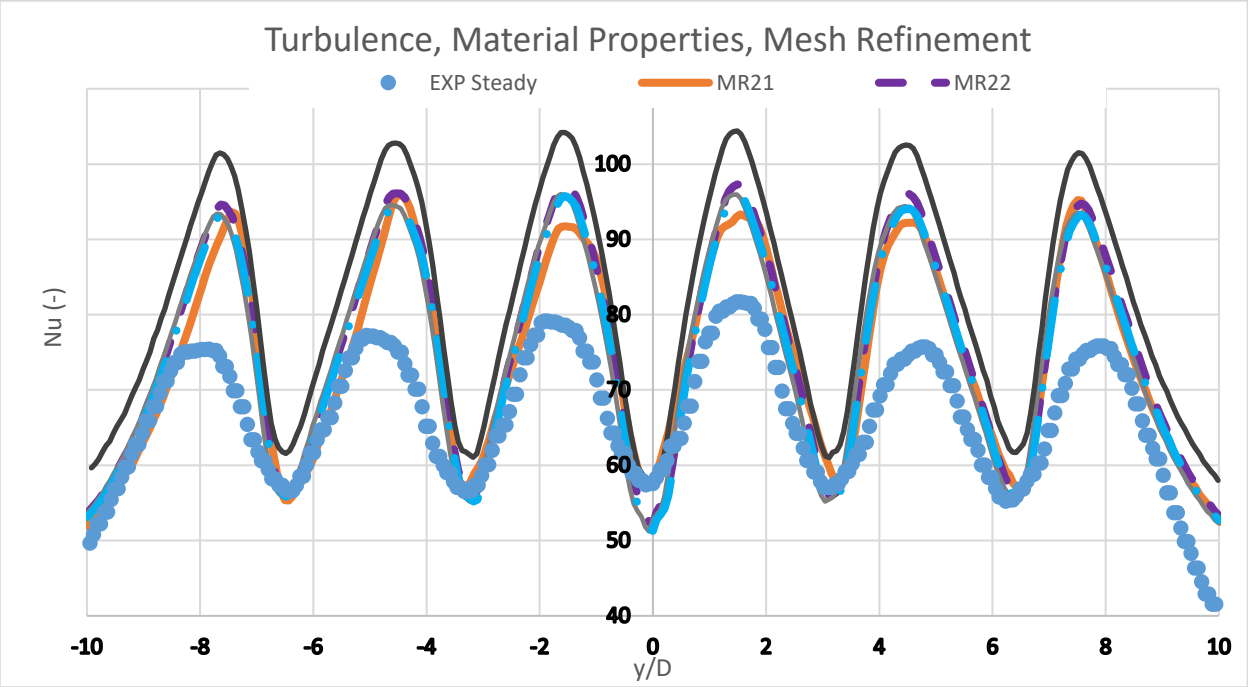

Figure 25: Inlet Turbulence Specification and Material Properties

Table 5: Mesh, Turbulence and Material Specification for refining experimental matching

Cases	No. Cells (-)	Base Size(-)	Target Surface Size (%)	Target PL Thickness (m)	TI (%)	TL (m)	Mu (Pa-s)	Cp (J/kg-k)	K (W/m-K)
2-1	2629005	0.0018	20	0.00028	12.2	0.0048	1.86E-05	1003.62	0.026305
2-2	2922441	0.0017	20	0.00014	12.2	0.0048	1.86E-05	1003.62	0.026305
2-3	2922441	0.0017	20	0.00014	0.5	0.0048	1.86E-05	1003.62	0.026305
2-4	2922441	0.0017	20	0.00014	0.5	0.0005	1.86E-05	1003.62	0.026305
2-5	2922441	0.0017	20	0.00014	0.5	0.0005	SL	Poly in T(k)	SL

Figure 26 gives the temporal span-wise averaged Nu distribution with its' characteristic Nu minimums between the upstream jets.

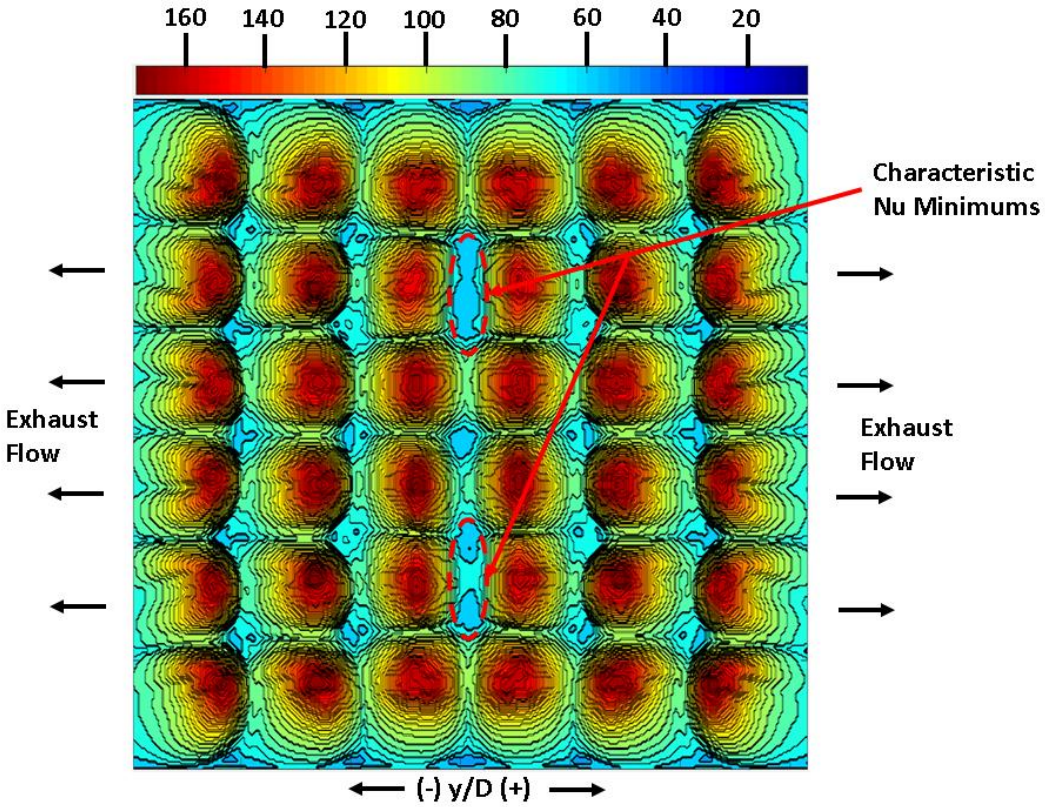

Figure 26: 2-5 Nu Distribution

The 2-5 Convective Courant Number is presented in Figure 27 and shows a maximum Convective Courant number nearly 0.7. The maximum target surface y+ value nearly 2.3 as shown in Figure 28.

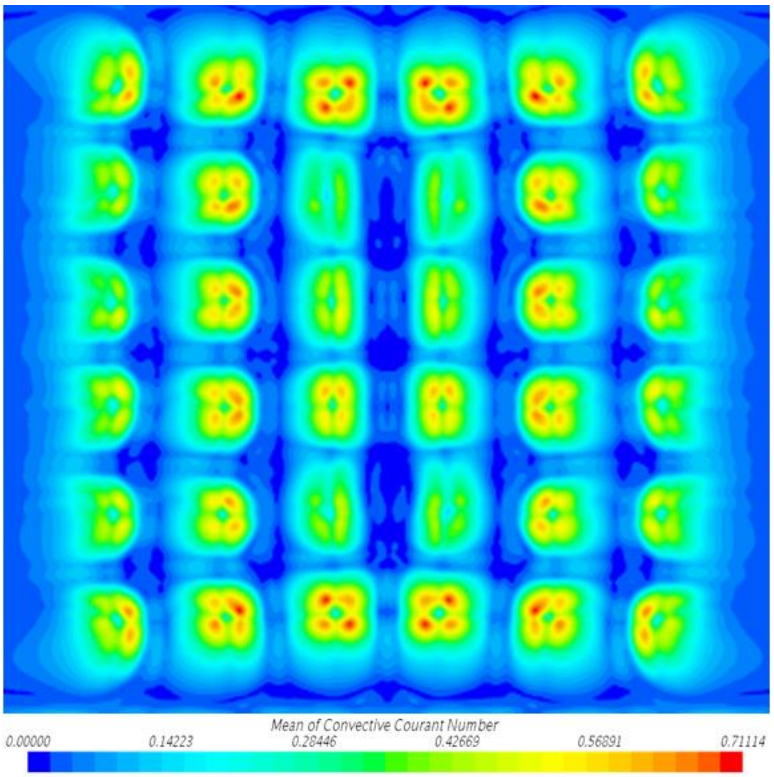

Figure 27: 2-5 Mean Convective Courant Number

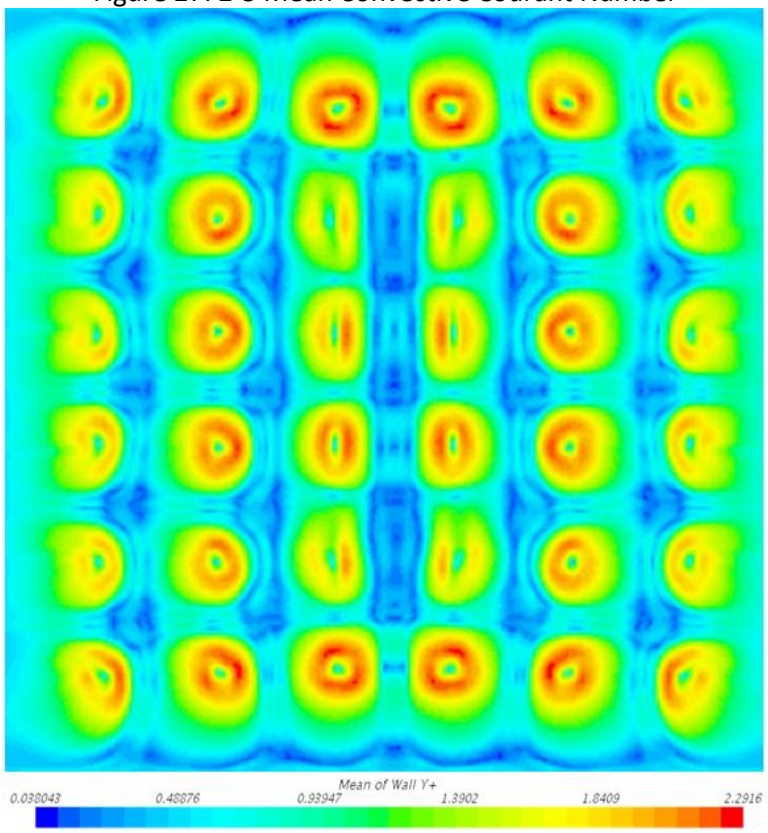

Figure 28: 2-5 Mean y+ distribution

A span-wise sectional plot of the convective courant number is given in Figure 29. Figure 30 presents a sectional plot of the velocity. The pressure distribution is plotted for a stream-wise sectional in Figure 31.

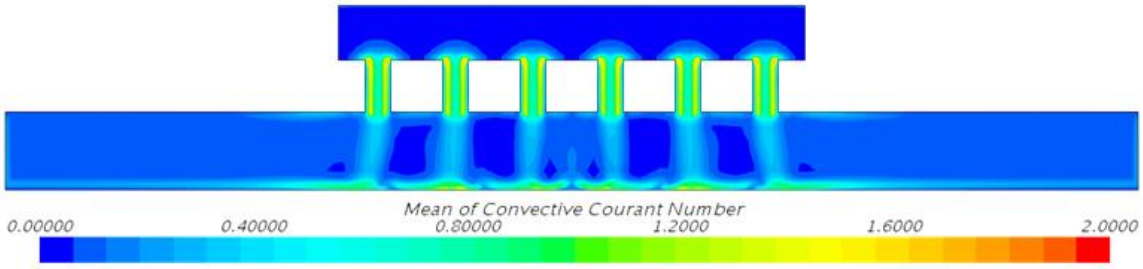

Figure 29: 2-5 Sectional Convective Courant Number

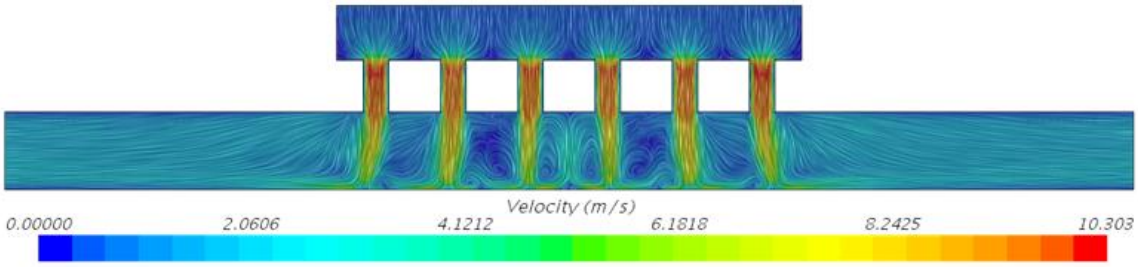

Figure 30: 2-5 sectional velocity plot

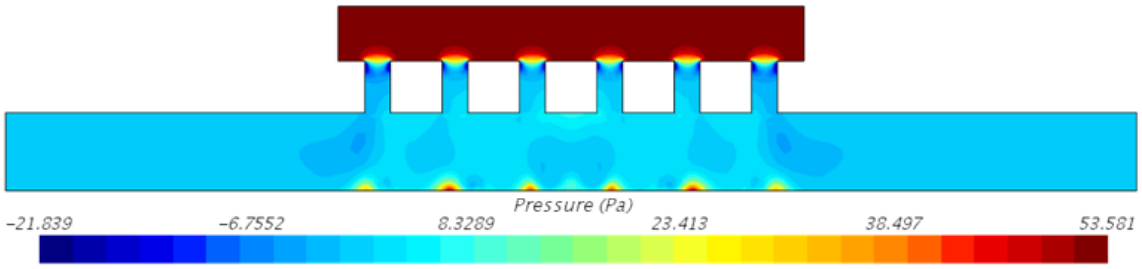

Figure 31: 2-5 sectional pressure plot

3. Temporal Sensitivity

Increasing the mass flow to an Re_{ave}=30,000 increases the wall shear stress leading to increased y+ values on the impingement surface. Maintaining an average y+ below 2 is crucial for assuring the Reynolds shear stresses as resolved and not model in the shear layer, particularly for pulse impinging flows where high fluid accelerations occur as the jets reach their peak velocities.

The mesh refinement scheme 2-5 given in Table 5 is used for the remaining simulations in this report. Three temporal schemes explored for optimization of computation resources while providing sufficient temporal resolution for physics modeling. Figure 32 gives temporal and span-wise averaged Nu distributions for the time steps ts=8e-6,9e-6, and 1e-5. A small but noticeable increase in Nu for the 8e-6 case while the Nu distribution for 9e-6 and 1e-5 show negligible distinction.

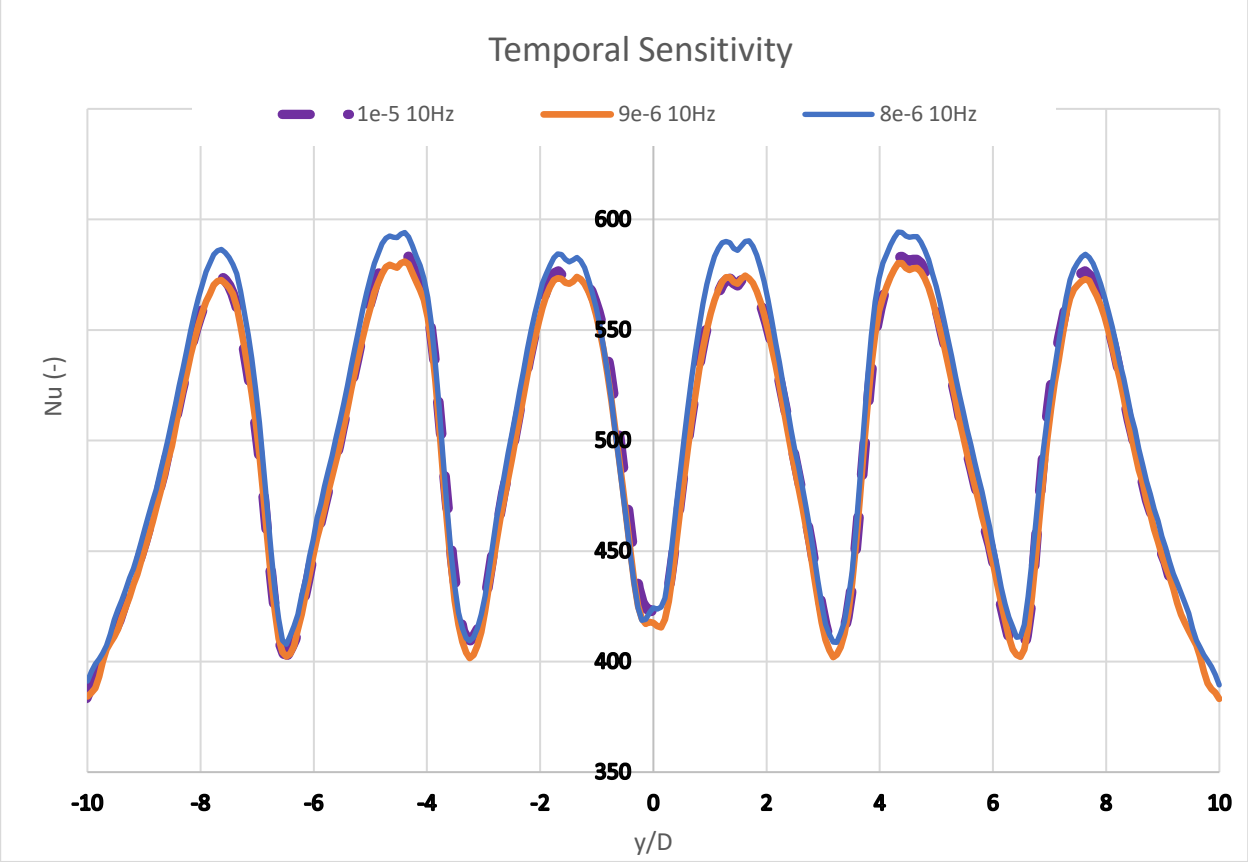

Figure 32: Time sensitivity for Re=30k

Temporal averaged plots of impingement surface y+ and convective courant number are given in Figure 33 and Figure 34 respectively for ts=1e-5. The temporal averaged max y+ near 2.3 ensures the resolving of Reynolds stresses in the near wall region of the impingement surface which is crucial with the heat flux coupled with the complex fluid flow due to the impinging jets.

The maximum temporal averaged convective courant number less than 1.2 indicates more than adequate temporal resolution at the impingement surface for resolving the viscous layer fluid behavior. Consequently ts=1e-5 is chosen to since it optimizes computation resources while providing reasonable Nu prediction.

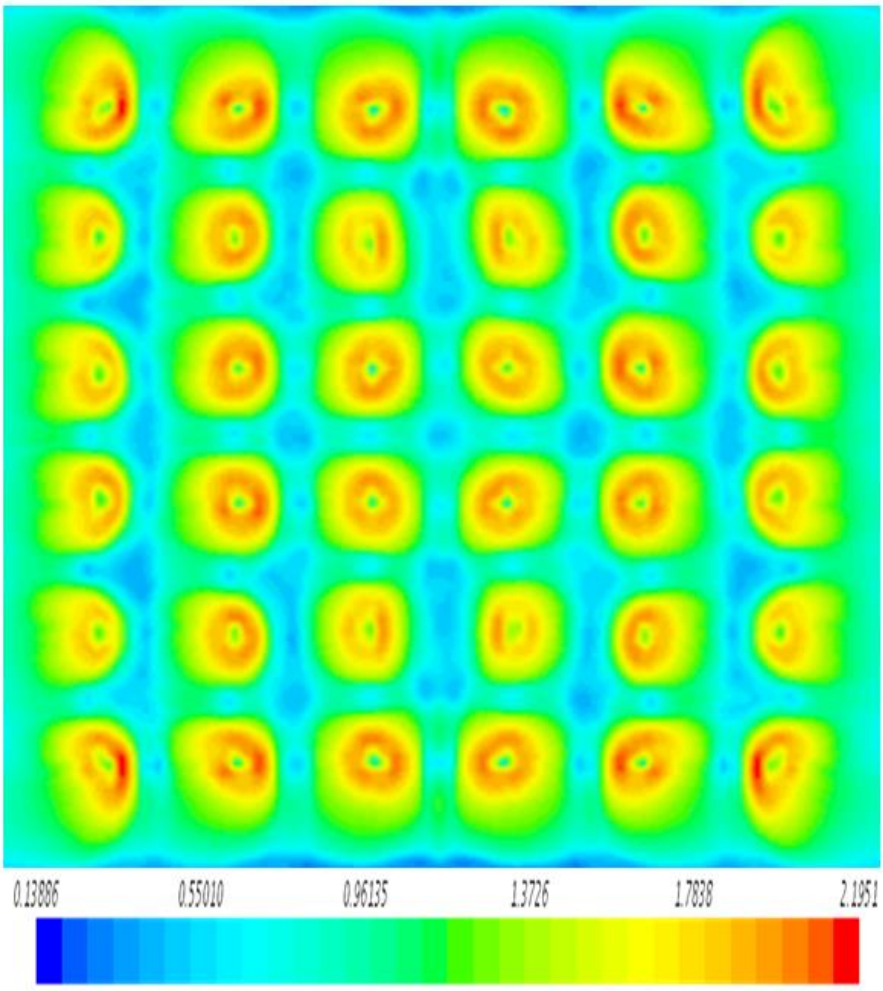

Figure 33: Impingement y+ plot; Re=30k, steady flow, Mesh 2-5 TS=1e-5

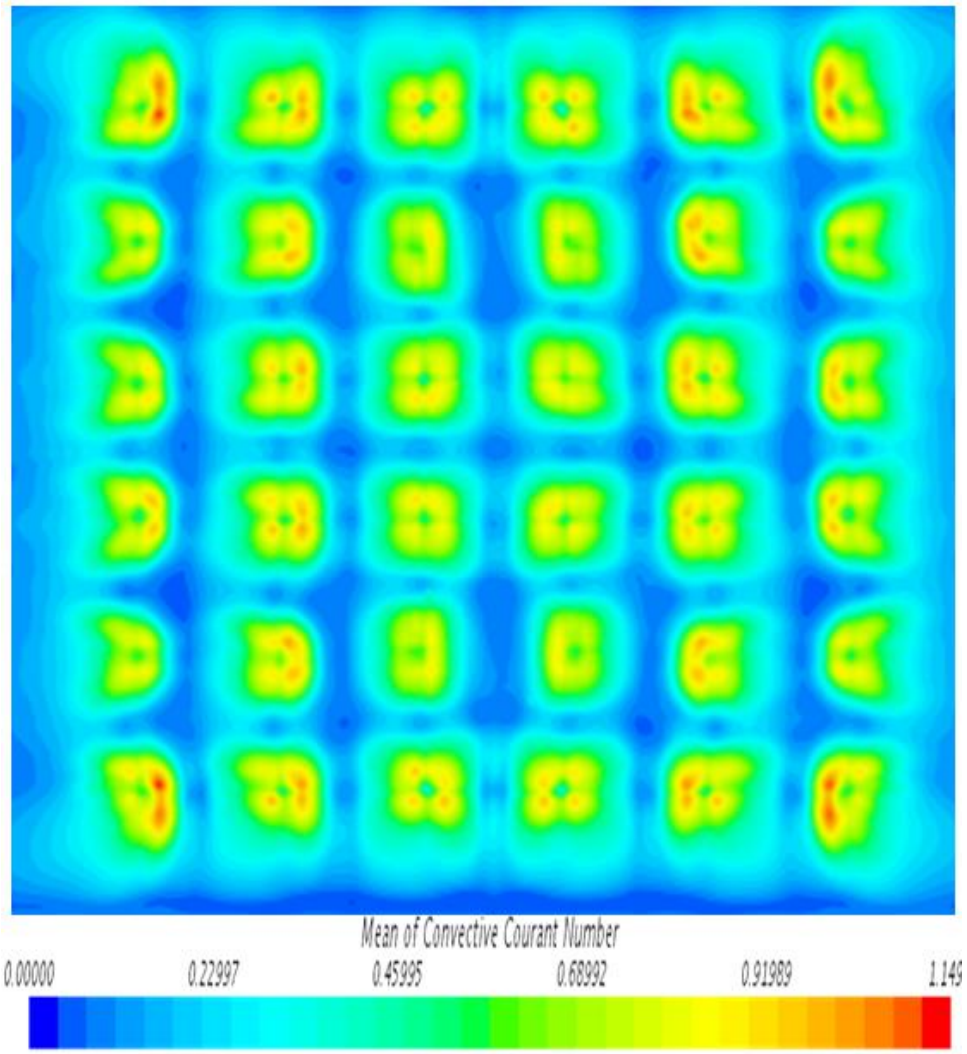

Figure 34: Impingement Courant Number plot; Re=30k, steady flow, Mesh 2-5

A span-wise sectional plot of the temporal averaged convective courant number is given in Figure 35. Though the plot shows the maximum convective courant number nearly 4.5 the plot shows majority of the jets and viscous layer to have convective courant values less than 2.5. This indicates adequate temporal resolution for resolving the free-stream fluid structures that directly influence the behavior of the jets and indirectly influence the flow behavior of in the viscous layer.

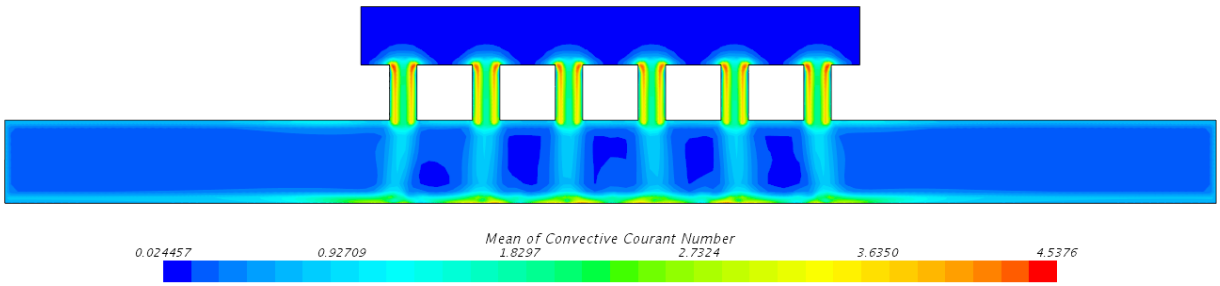

Figure 35:Span-wise Convective Courant Number distribution; Re=30k, steady coolant flow TS=1e-5

The temporal averaged Nu of the impingement boundary for the impingement region is plotted in Figure 37. The presence of stream-wise periodic regions of Nu minimums are noted between the center jet columns. It is interesting to note the alternating of strong jet pairs with high stagnation Nu and weak jets with lower stagnation Nu distributions. This behavior is seen in this study's experimental results as shown in Figure 19. This periodic Nu minimum behavior is also seen to occur near the upstream jet columns in the experimental work reported by Keenan [29] and Zimmer [28].

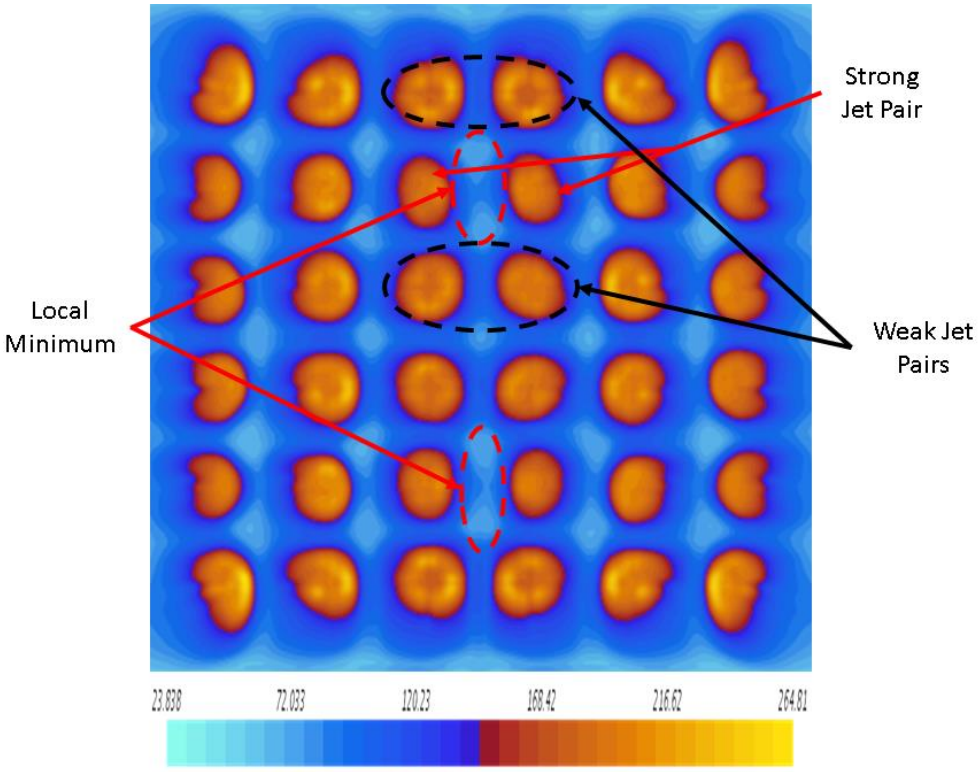

Figure 36: Impingement Surface Temporal Averaged Nu distribution; Re=9550, steady coolant flow, M32P3, TS=1e-5

IV. CFD Studies

These sections present CFD results at temporal averaged Re numbers or 12,000 and 30,000 for various coolant amplitudes and frequencies configurations.

A. Results at Re=12,000

The basic computational parameters varied for the temporal mean flow characterization of Re=12k is given in Table 6.

Table 6: Re=12k CFD study conditions

Cases	Re_{ave} (-)	f (Hz)	AR (%)	x/D (-)	y/D (-)	z/D (-)	q" (W/m	T_i (k)
Re12k 10Hz AR(70)	12,000	10	70	3	3	3	5.80E+03	300
Re12k 10Hz AR(34.6)	12,000	10	34.6	3	3	3	5.80E+03	300
Re12k 10Hz AR(17.3)	12,000	10	17.3	3	3	3	5.80E+03	300

Re12k 20Hz AR(17.3)	12,000	20	17.3	3	3	3	5.80E+03	300
Re 12k 5Hz AR(17.3)	12,000	5	17.3	3	3	3	5.80E+03	300
Re 12k 2Hz AR(17.3)	12,000	2	17.3	3	3	3	5.80E+03	300
Re 12k Steady	12,000	0	0	3	3	3	5.80E+03	300

1. Influence of Frequency

Four coolant flow frequency variations are compared to steady coolant flow conditions for determining the effectiveness of frequency on heat transfer efficiency. Coolant flow frequencies of 2Hz, 5Hz, 10Hz, and 20Hz are presented with steady flow in Figure 37.

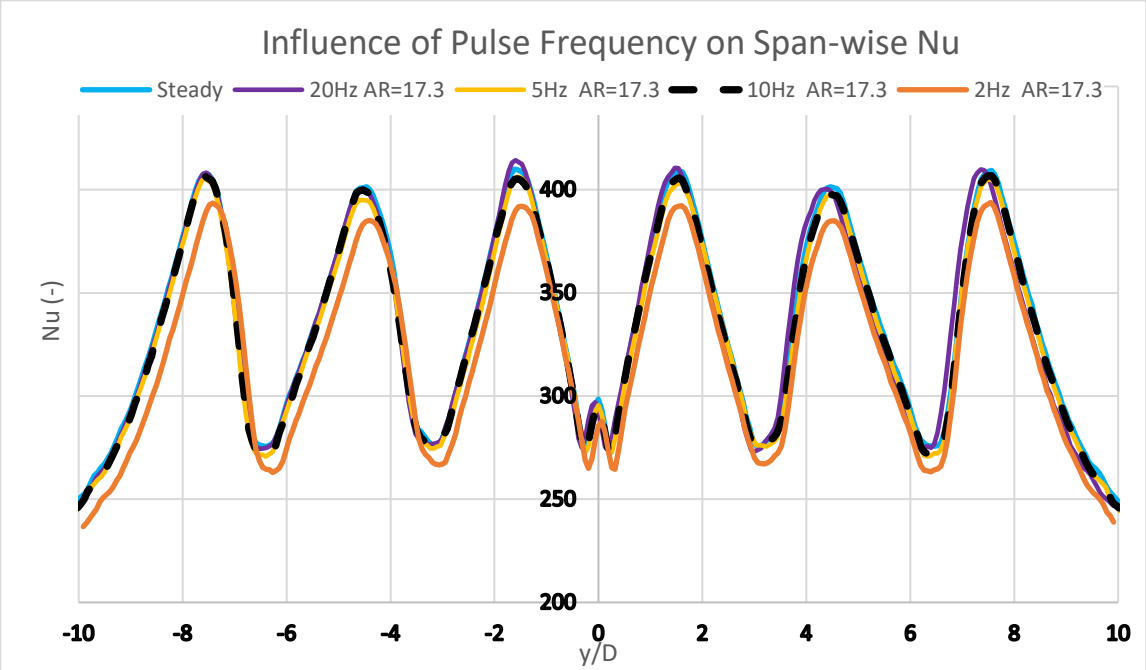

Figure 37: Influence of frequency at Re=12k; Span-wise Nu

The temporal and span-wise average Nu distribution shows the presence of pulse flow negatively impacts the heat transfer efficiency for frequencies less than 20Hz with negligible increase with a pulse frequency of 20Hz to a Nu value less than the steady flow configuration.

This decrease in heat transfer efficiency is observed to become more pronounced with low coolant flow frequencies near 2Hz. The power consumption ratio is seen to increase with the addition of pulse flow by 37% for 5&10 Hz case and 36% for the 20Hz case.

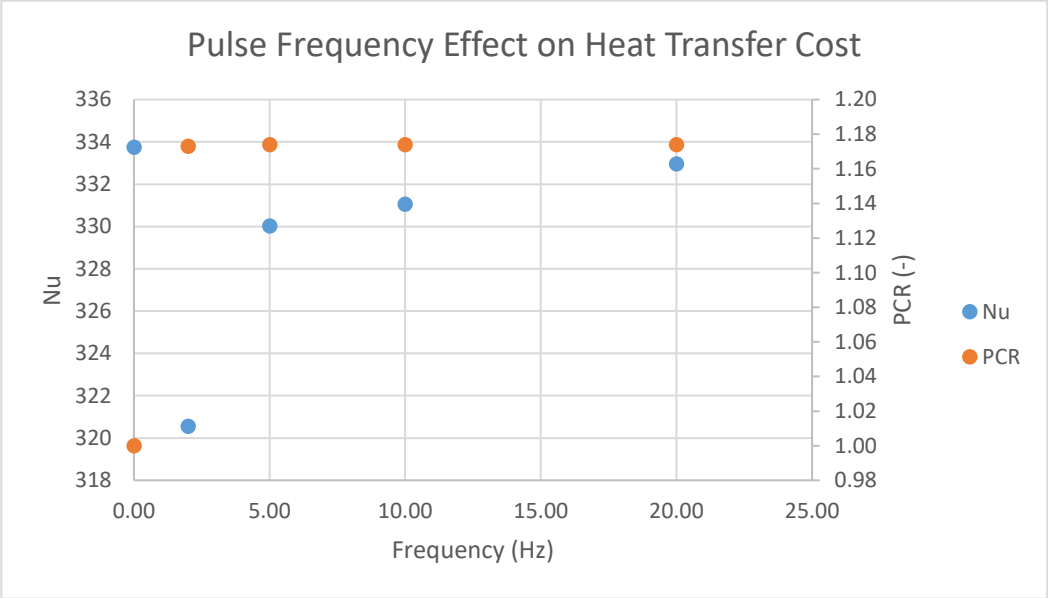

Figure 38: Frequency variation influence on convective heat transfer; Re=12k, AR=17.3

Figure 39 plots the ER as a function of Str. The addition of pulsed flow is seen to negatively impact the heat transfer nearly 4% at 2Hz and then approach steady flow heat transfer efficiency. The temporal averaged Nu plots for varied frequencies 0-20 are given in Figure 40 (a)-(e). Each Nu plot shows the characteristic minimums between strong upstream jets with adjacent weak jets. Though the flow periodicity in location among the stream-wise jet rows Figure 40 (e) shows the dispersion is semi-random which is intuitive due the presence of instabilities in the flow.

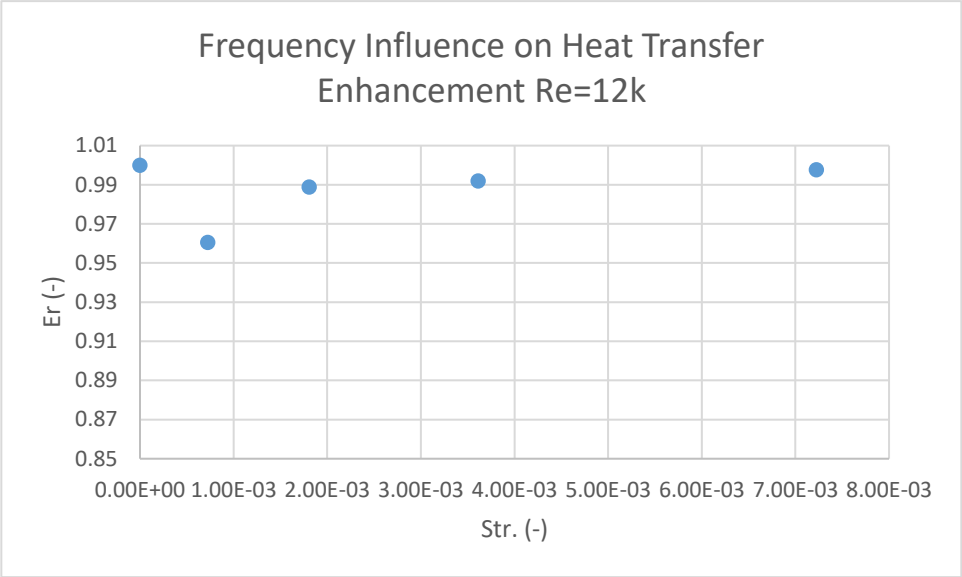

Figure 39:Pulse influence on heat transfer enhancement

a)

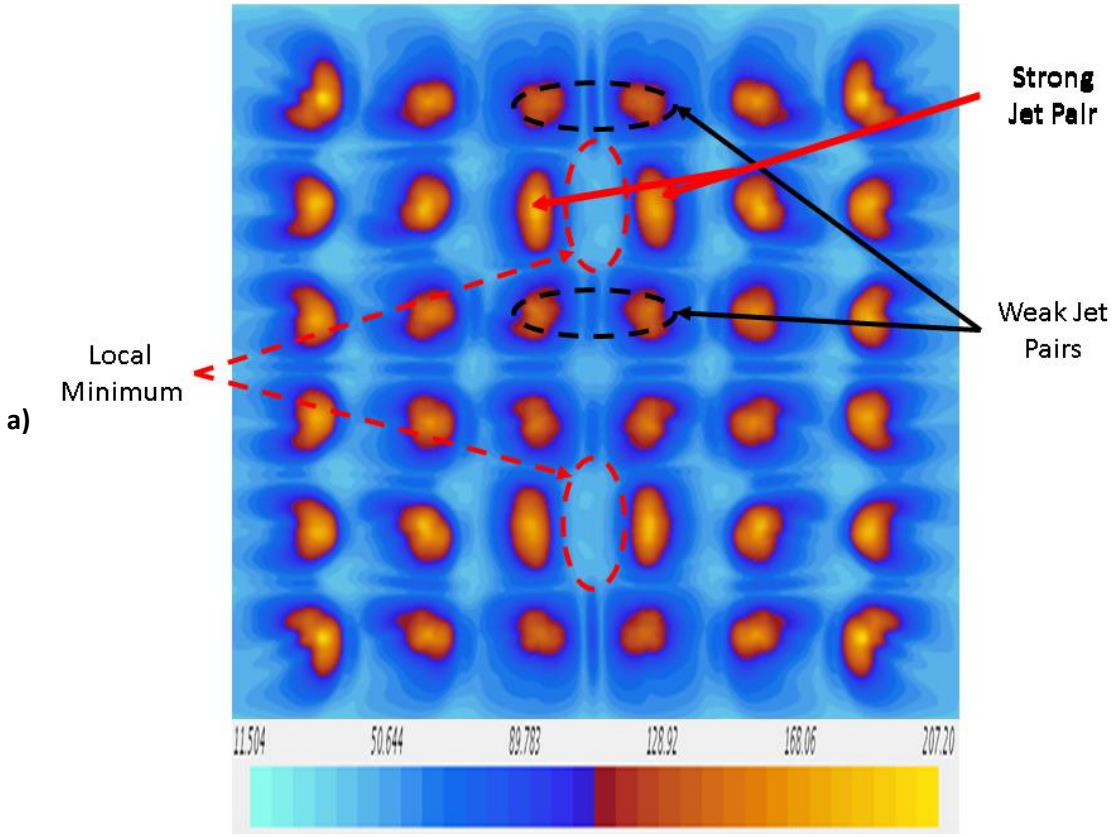

b)

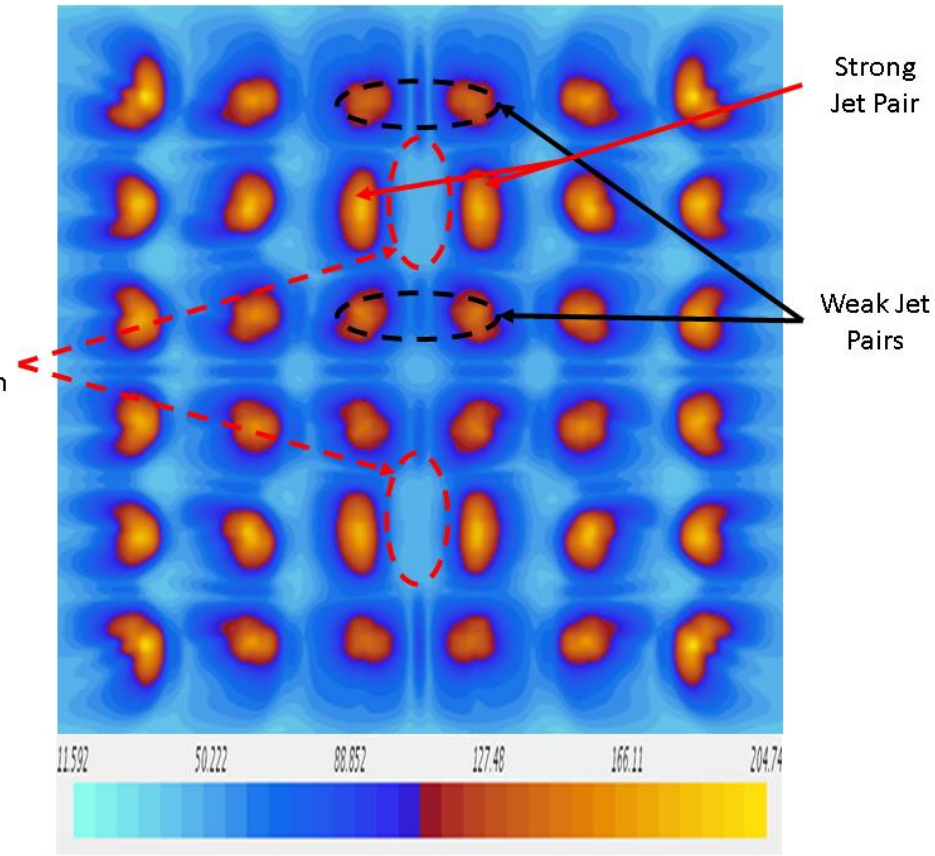
Strong
Jet Pair
Weak Jet
Pairs
Local
Minimum
11.592
50.222
88.852
127.48
166.11
204.74

c)

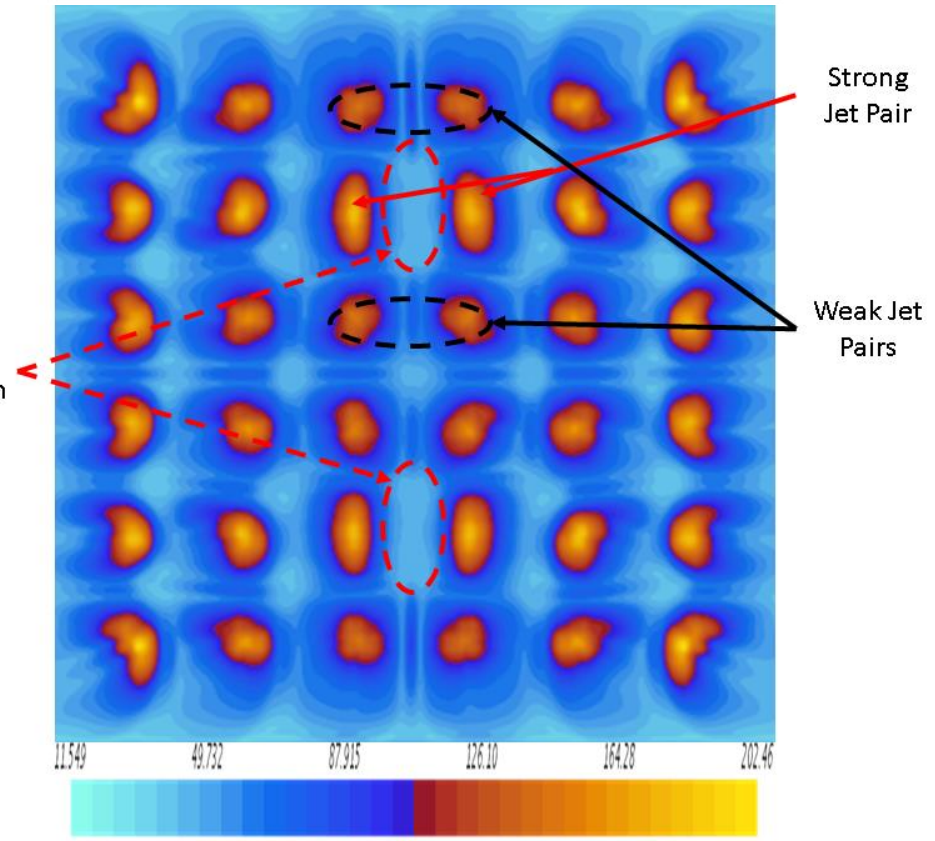
Strong
Jet Pair
Weak Jet
Pairs
Local
Minimum
11.549
49.732
87.915
126.10
164.28
202.46

d)

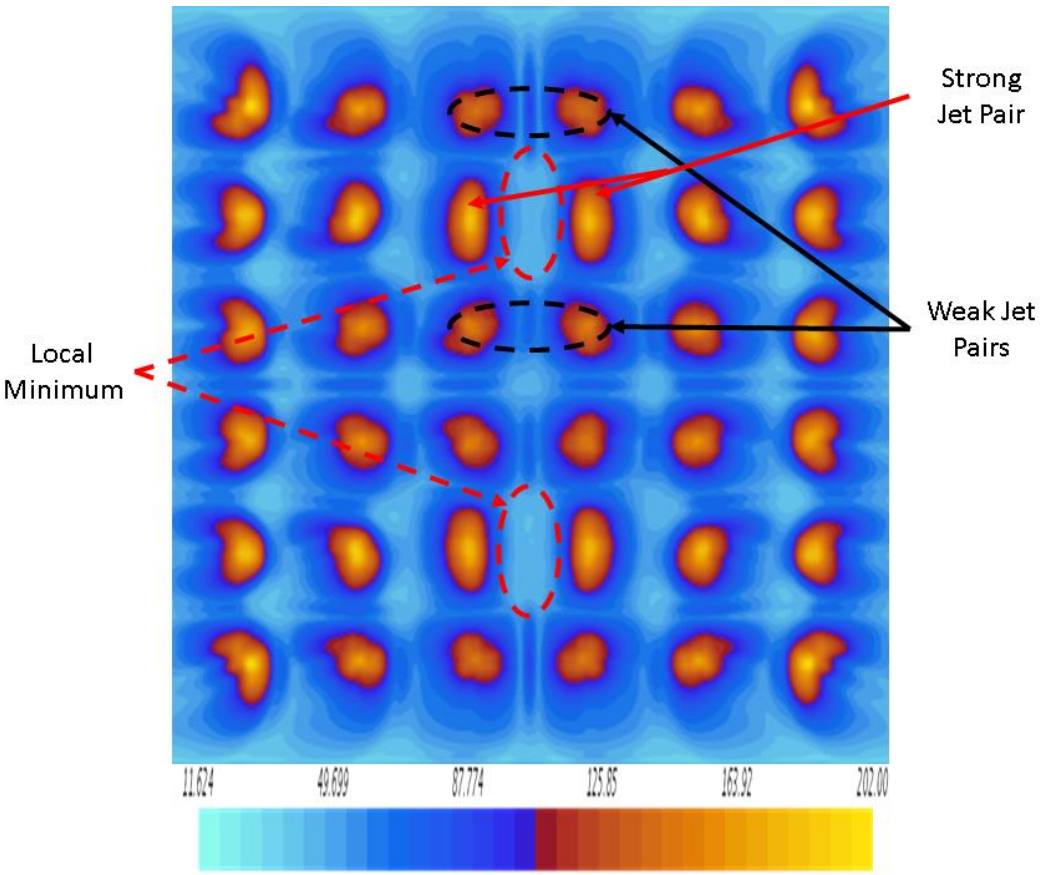
Strong
Jet Pair
Weak Jet
Pairs
Local
Minimum
11.624
49.699
87.774
125.85
163.92
202.00

e)

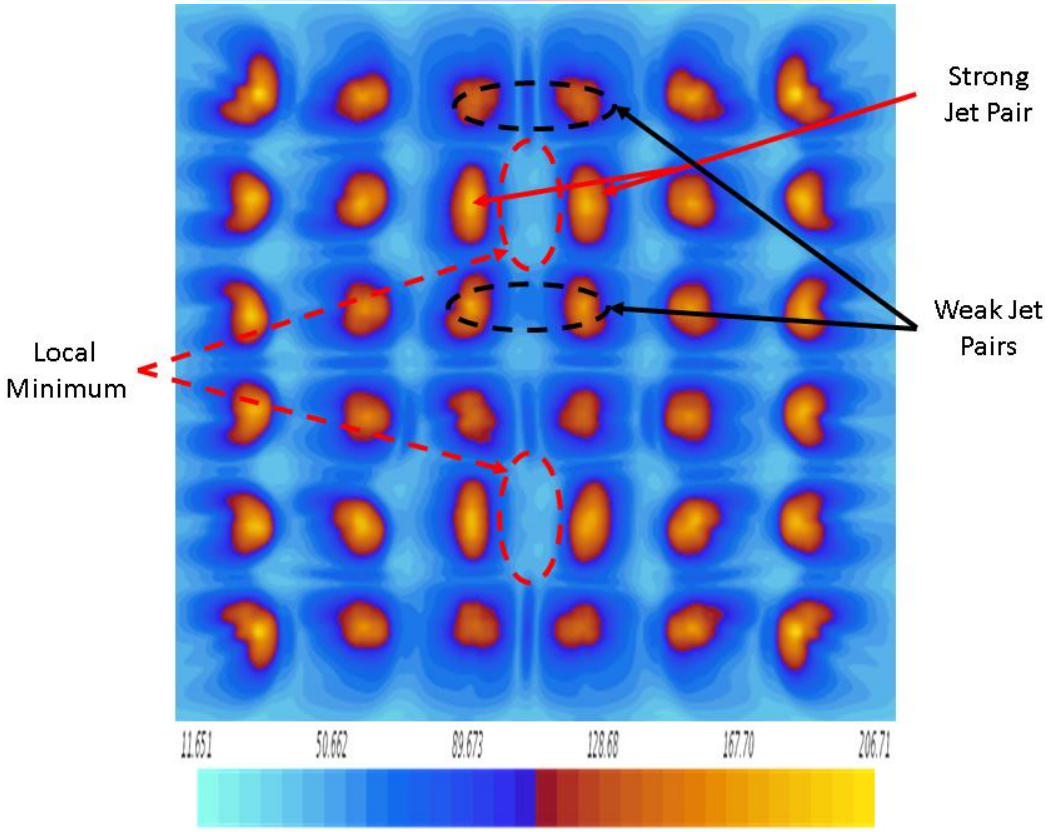
Strong
Jet Pair
Weak Jet
Pairs
Local
Minimum
11.651
50.662
89.673
128.68
167.70
206.71

Figure 40: Temporal average Nu plots for varied frequencies; Re=3820 (a) Steady coolant flow, (b) 2Hz, (c) 5Hz, (d) 10Hz, and (e) is 20Hz with frequency flows taken with an amplitude ratio va/vm=17.3

2. Influence of Amplitude

Three simulation cases with varied amplitude ratios are compared with steady coolant flow to evaluate the influence of flow on impingement heat transfer. Amplitude ratios of 17.3, 34.6, and 70. The amplitude studies were performed at a pulse frequency of 10Hz and are compared on a temporal average Nu basis for a span-wise average distribution as shown in Figure 42. Plotted on the secondary independent axis is the minimum required power ratio for producing the flow configuration. The addition of pulsed flow is seen to negatively impact the convective heat transfer and is exacerbated with the increase in pulse amplitude. Pulse flow is further complicated by the increase in power consumption ratio with the presence of pulsed flow that increase nonlinearly with the increase in pulse amplitude. The span-wise temporal averaged Nu is included in Figure 41.

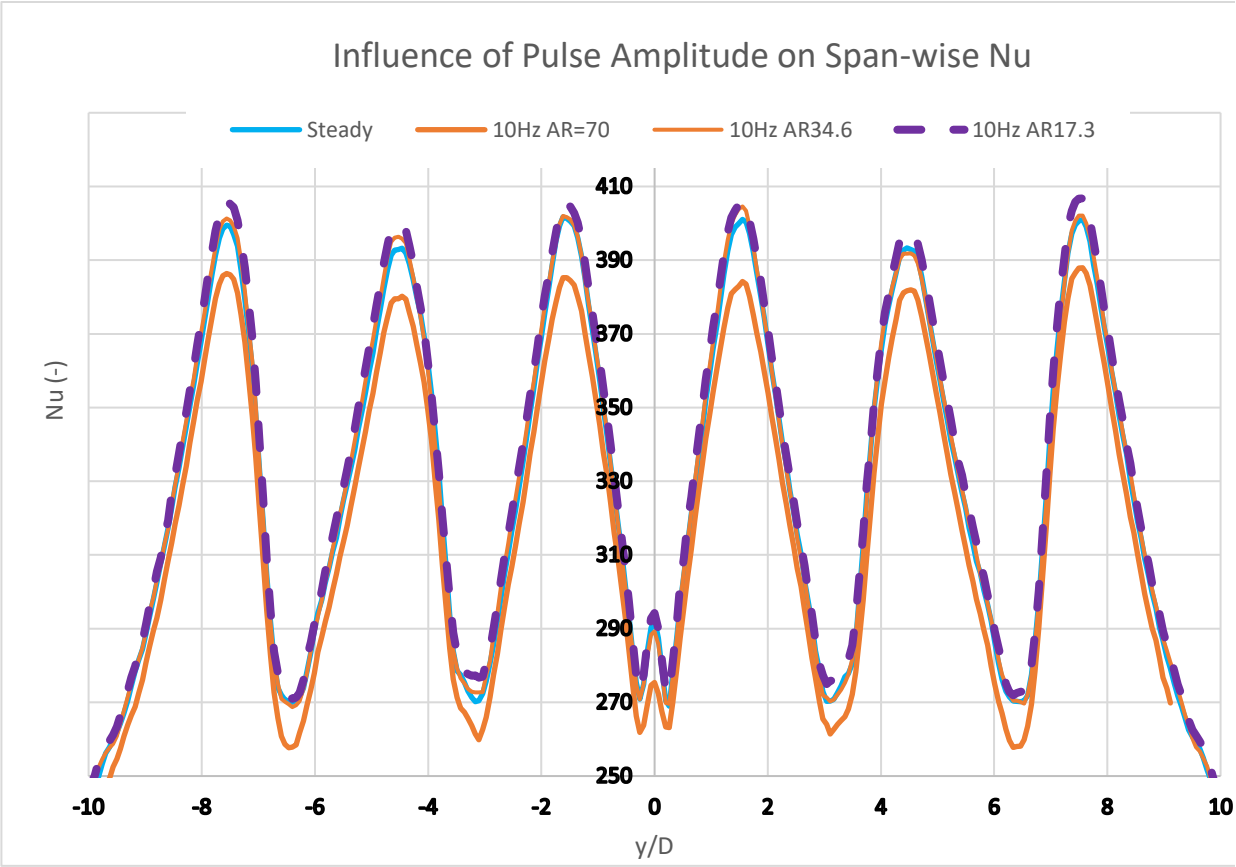

Figure 41: Influence of Pulse Amplitude on Span-wise Nu

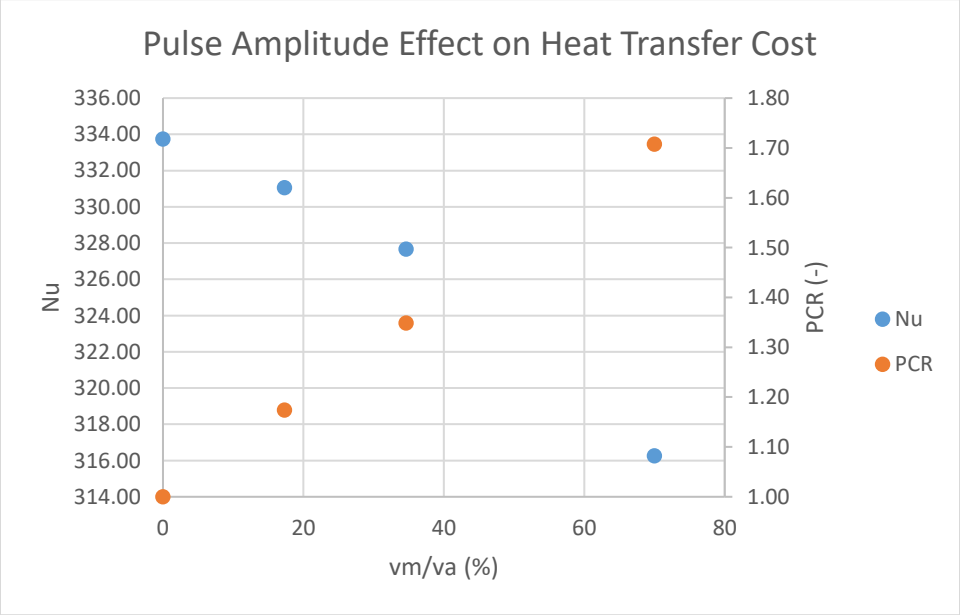

Figure 42: Influence of Coolant Amplitude for Re=12k; Span-wise Nu

The span-wise averaged Nu distribution shows the increase in coolant amplitude leads to a decrease in heat transfer efficiency. The temporal averaged Nu plots for amplitude dependence are given in Figure 43 (a)-(d) for amplitude ratios 0-70%. The Nu minimums between upstream strong jets with adjacent weak jets are observed in each amplitude configuration. Figure 43 (d) shows Nu minimums separated by two rows of weak jets contrasted to a single row in Figure 43 (a)-(c).

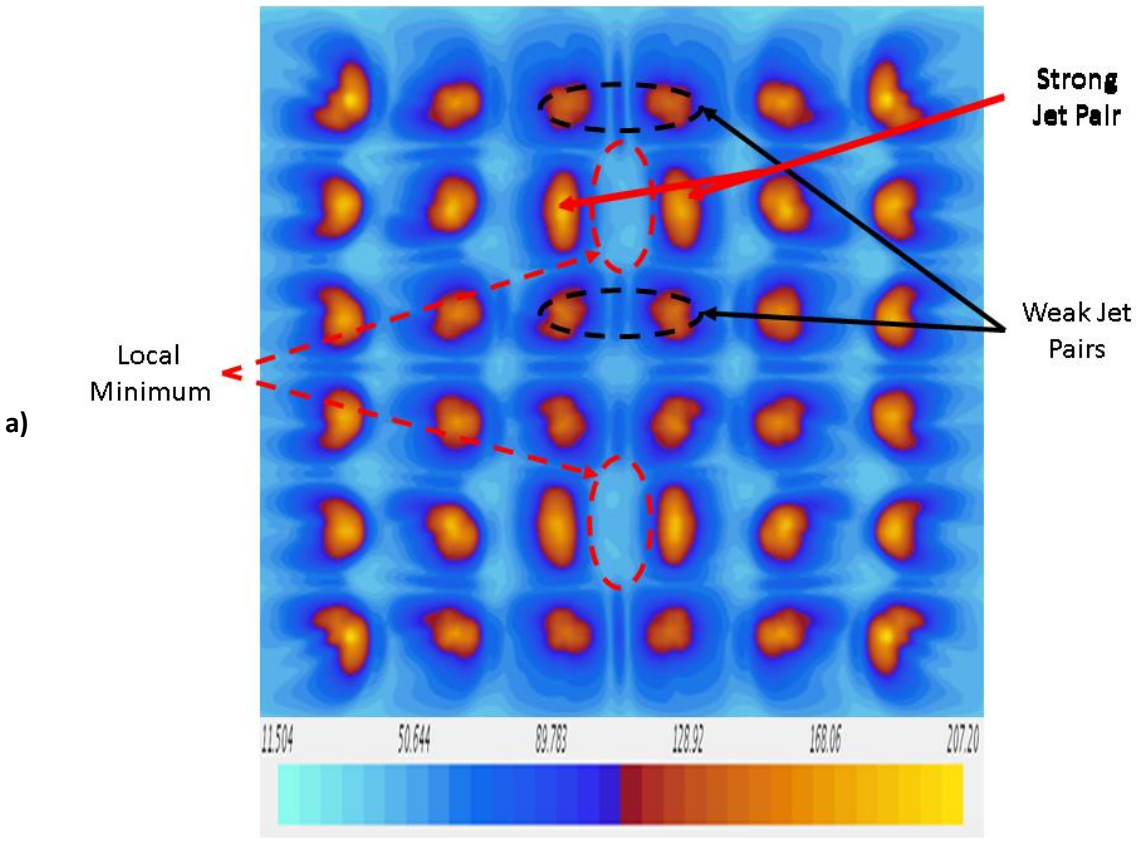

a)

b)

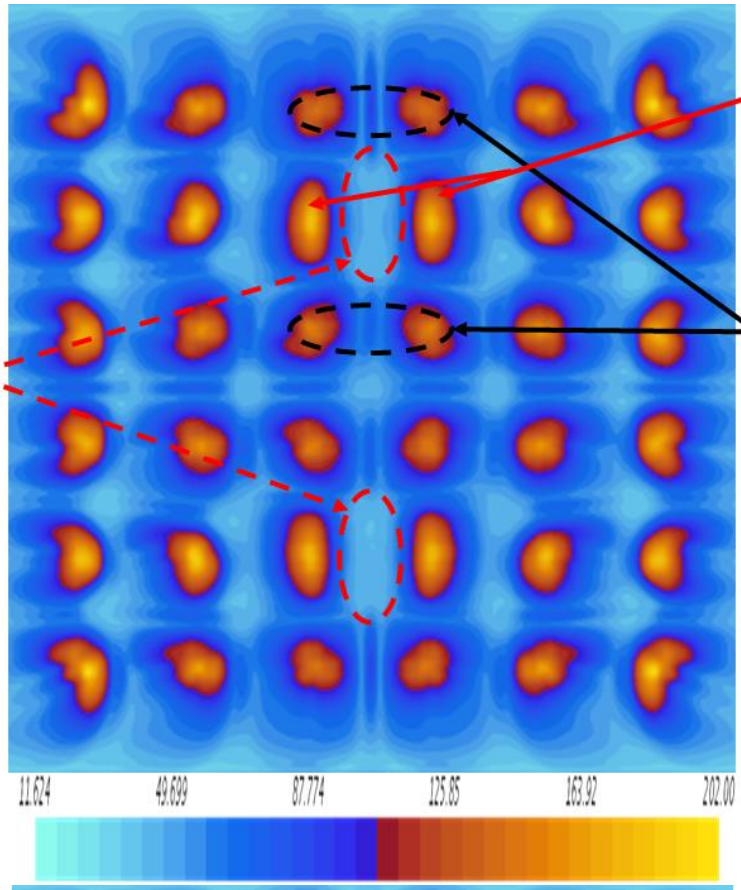
Strong
Jet Pair
Weak Jet
Pairs
Local
Minimum
11.624
49.639
87.774
125.85
163.92
202.00

c)

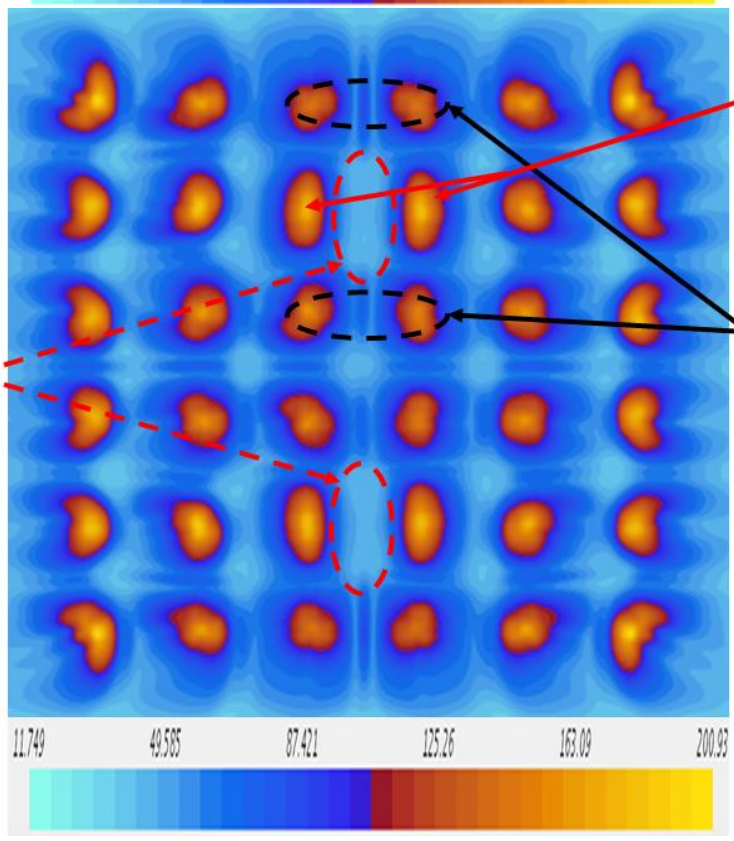
Strong
Jet Pair
Weak Jet
Pairs
Local
Minimum
11.749
49.585
87.421
125.26
163.09
200.93

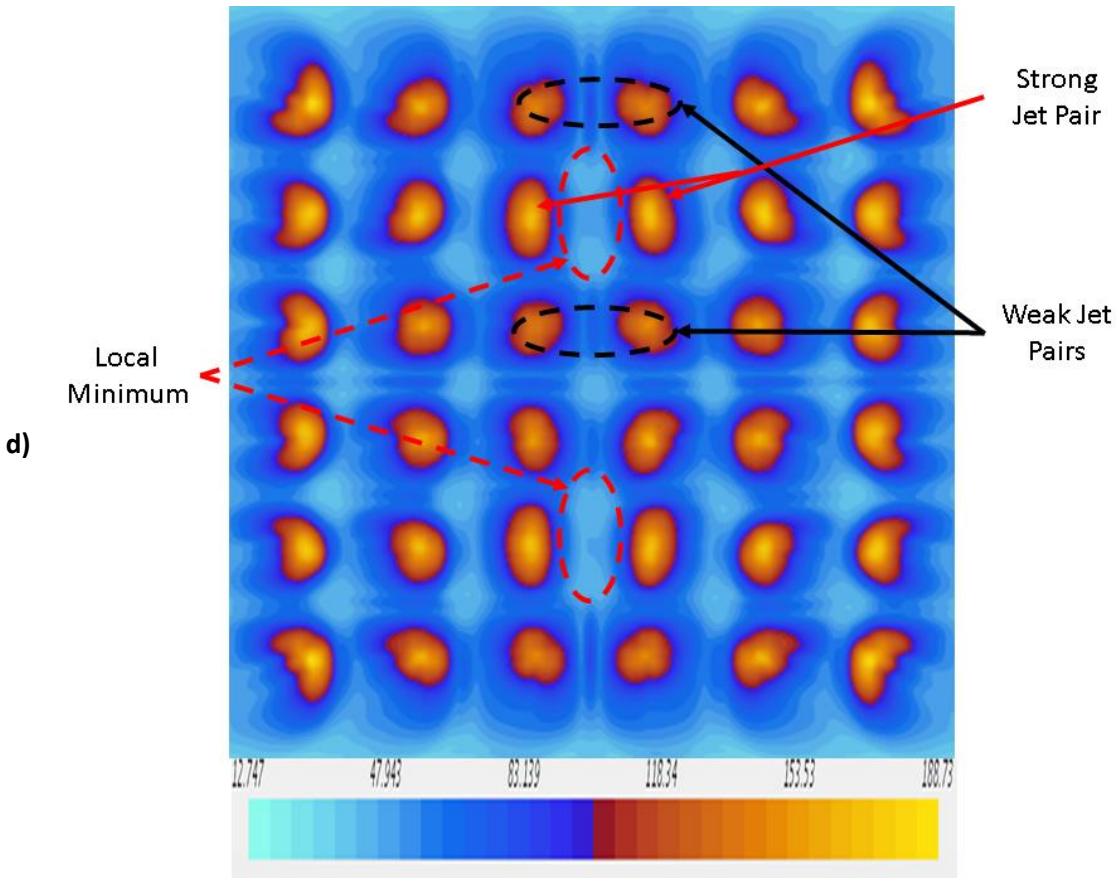

Figure 43: Temporal averaged Nu with varied amplitudes, Re=3820; 10Hz for frequency flows (a) Steady flow, (b) AR(17.3), (c) AR(34.6), and (d) AR(70)

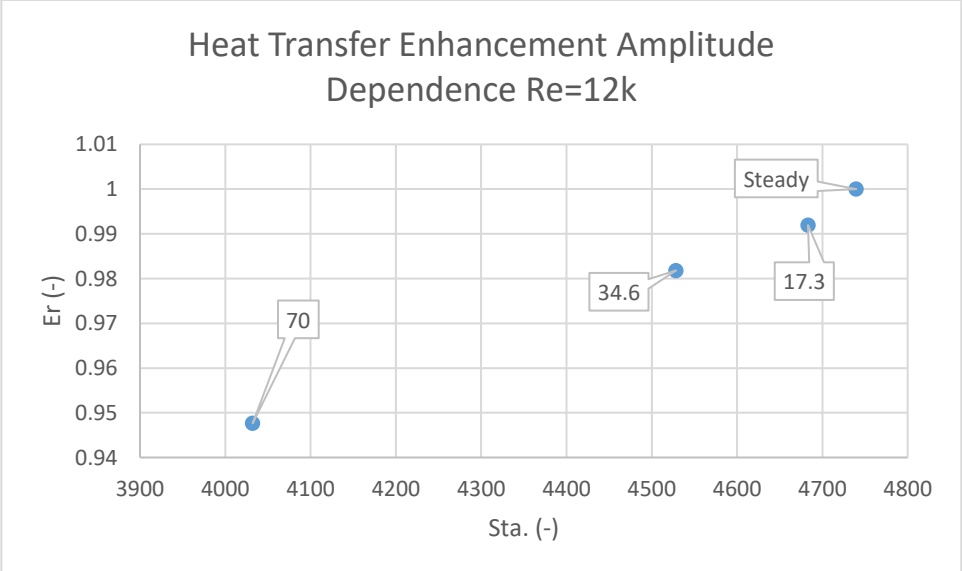

Figure 44: Amplitude influence on bulk coolant heat transfer efficiency

3. Flow Behavior

The temporal mean Mach Number distribution is given in Figure 45. The region of highest Mach number occurs in the nozzles with a mean Ma <0.2. The temporal mean pressure distribution presented in Figure 45 shows circulation induced pressure drops on edge of the nozzle entrance and high pressure at the stagnation region as the flow impinges on the surface and changes to a radial direction. Figure 47 presents the velocity distribution on a stream-wise section intersecting one inner jet row. Important flow patterns include entrained vortex pair between the two upstream jets, the presence of the stagnation zone, and the development of the wall jet. A notable occurrence is seen in the decrease in entrained vortices between jets with downstream progression. This decrease indicates the deflection of downstream jets is not due to the presence of the vortices but rather the increase in mass flow with downstream progression that deflects the jets.

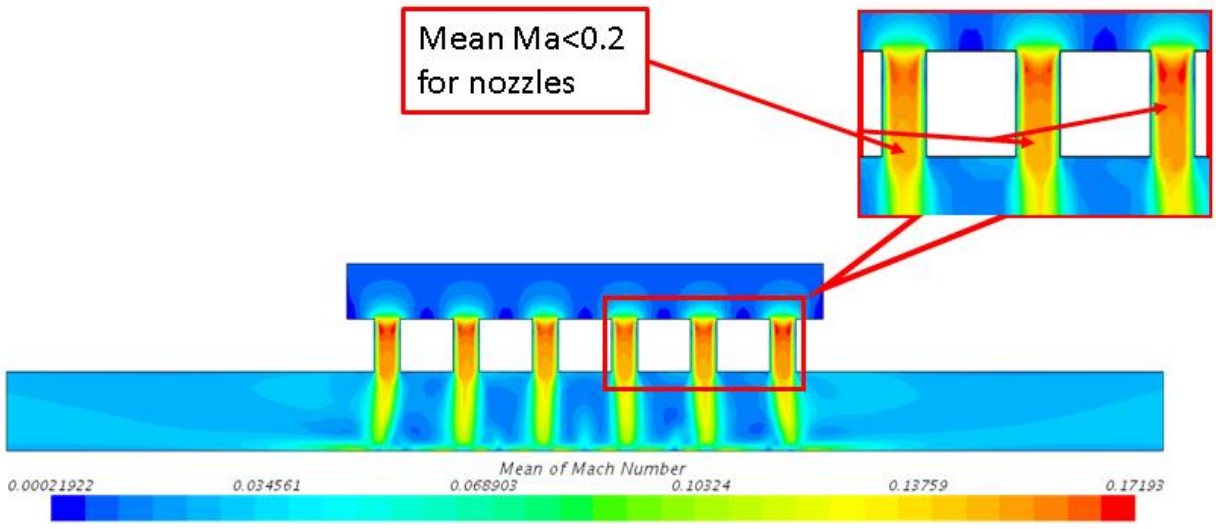

Figure 45: Sectional Mach distribution, Re=12k, steady flow

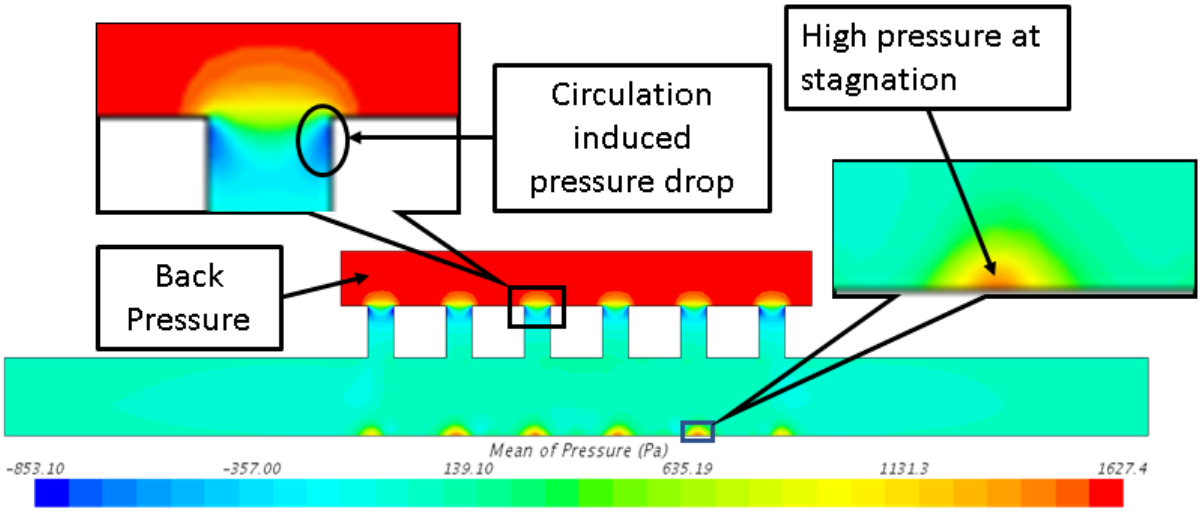

Figure 46: Sectional Pressure distribution, Re=12k, steady flow

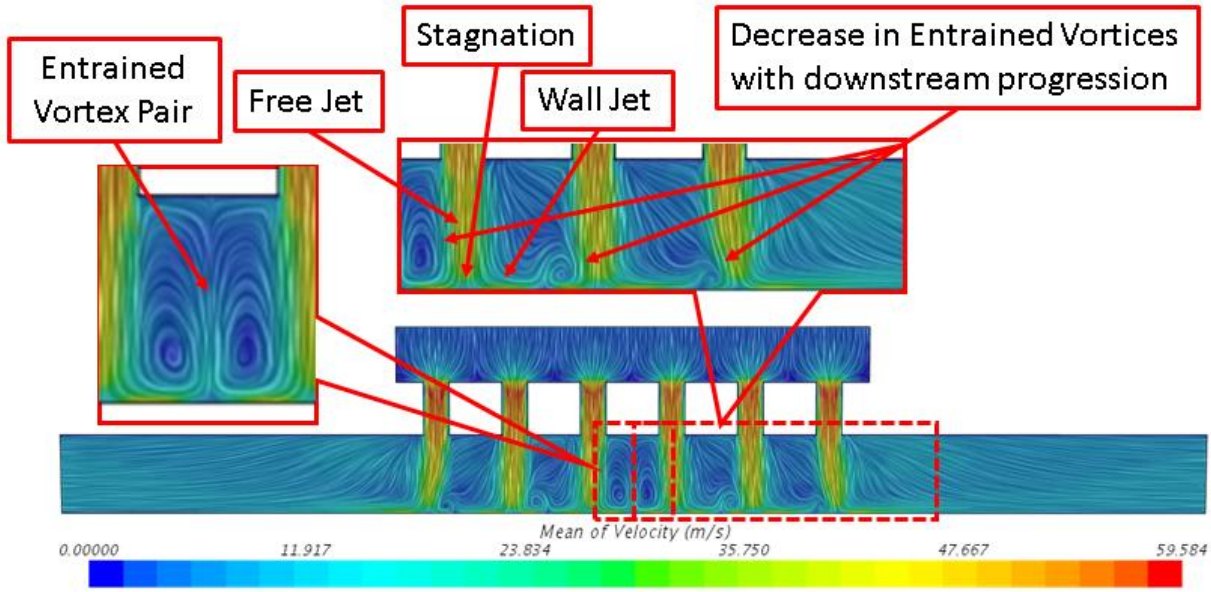

Figure 47: Sectional Velocity distribution, Re=12k, steady flow

Figure 48 gives maximum Ma with the $Nu_{s,ave}$ for varied AR. Since the maximum Ma for the for the extreme case is no greater than 0.3 compressibility is not expected to a large factor for this flow configuration. The decrease $Nu_{s,ave}$ in increase in Ma is due to the max Ma occurring at the peak of the mass flow wave. An additional evaluation of Mach number influence on impingement heat transfer for Re=12k is given if Figure 49 through Figure 51 where the mean

target surface Nu is plot with the max Ma for three cycles. The Nu is seen to behave proportionately to Ma which indicates that no variation from Nu highly dependent on the jets velocities.

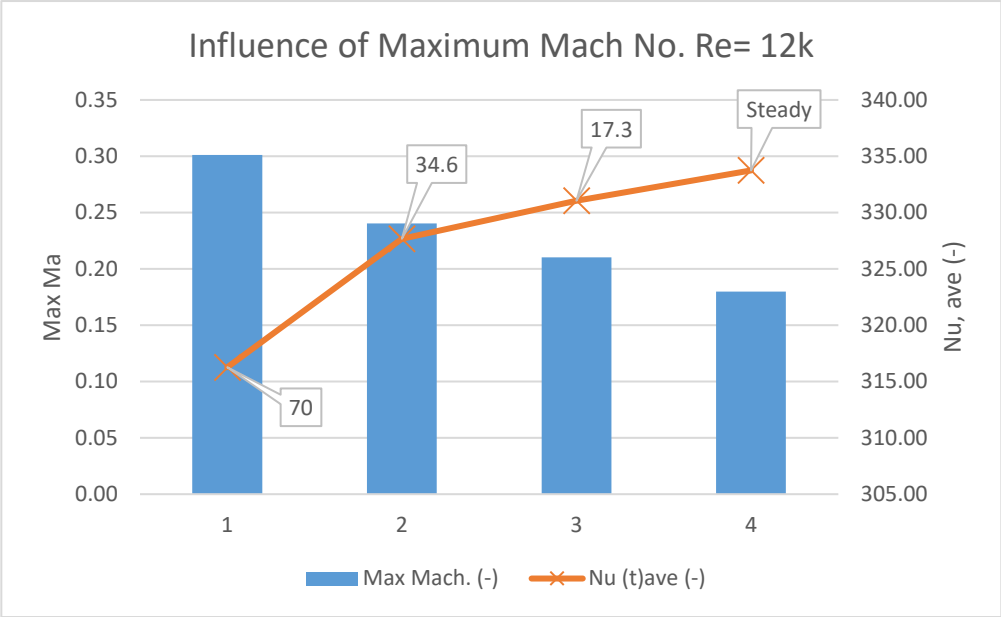

Figure 48: Influence of Mach No. on heat transfer; Re=12k, 10Hz

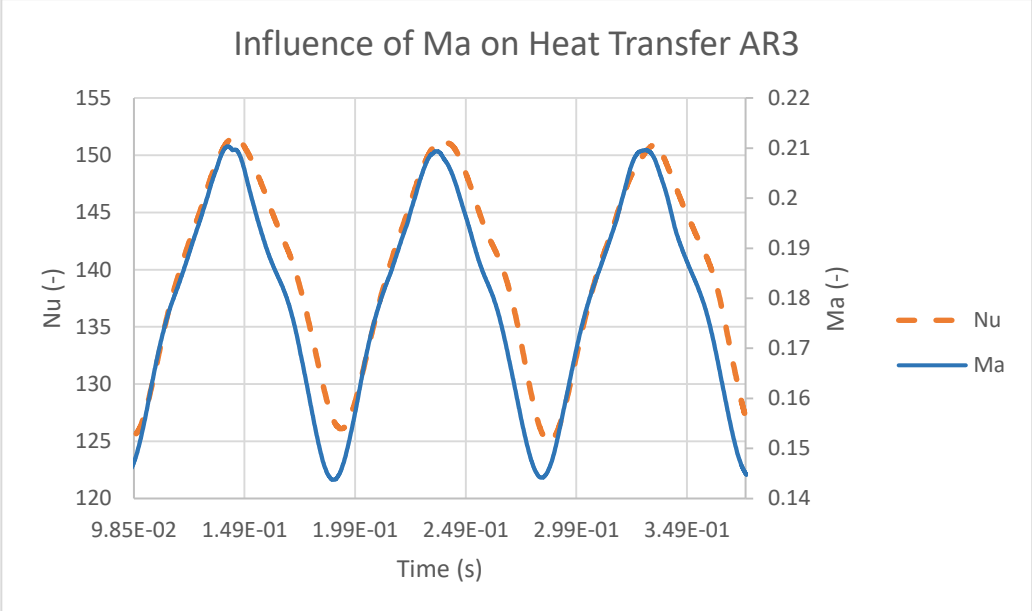

Figure 49: Influence of Ma on Heat Transfer; Re=12k, 10Hz, AR=17.3

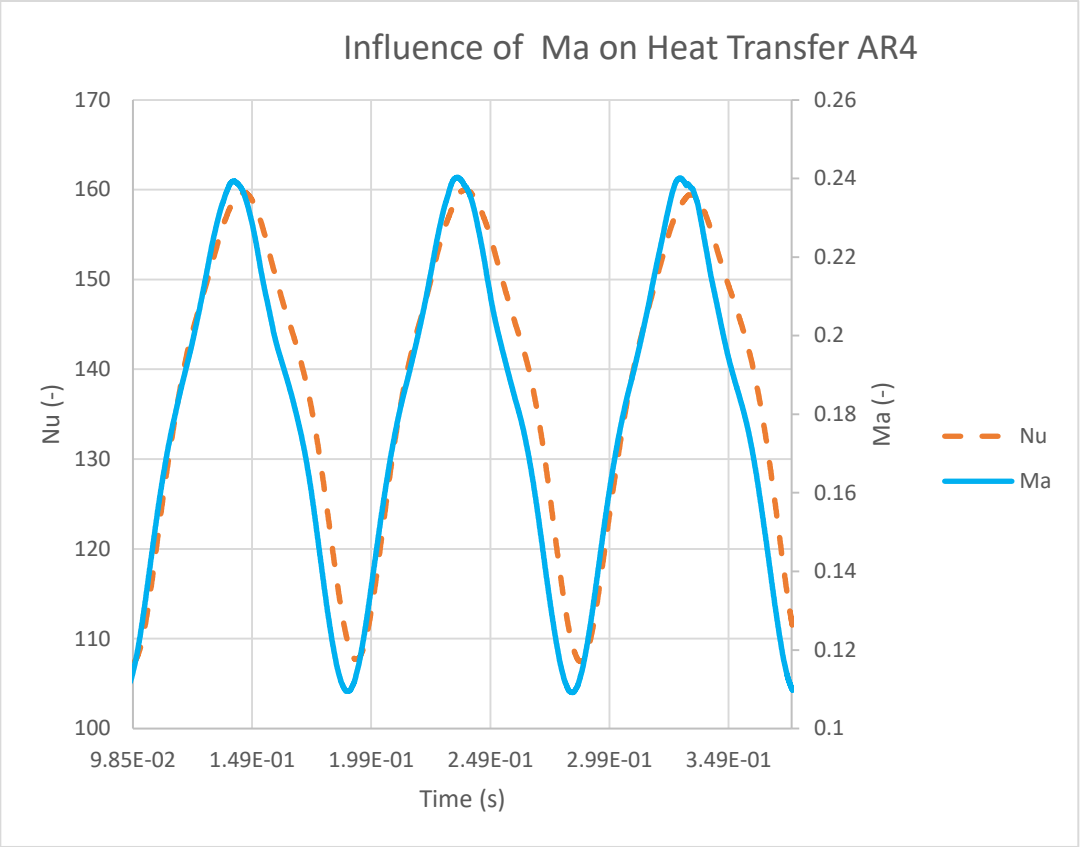

Figure 50: Influence of Ma on Heat Transfer; Re=12k, 10Hz, AR=34.6

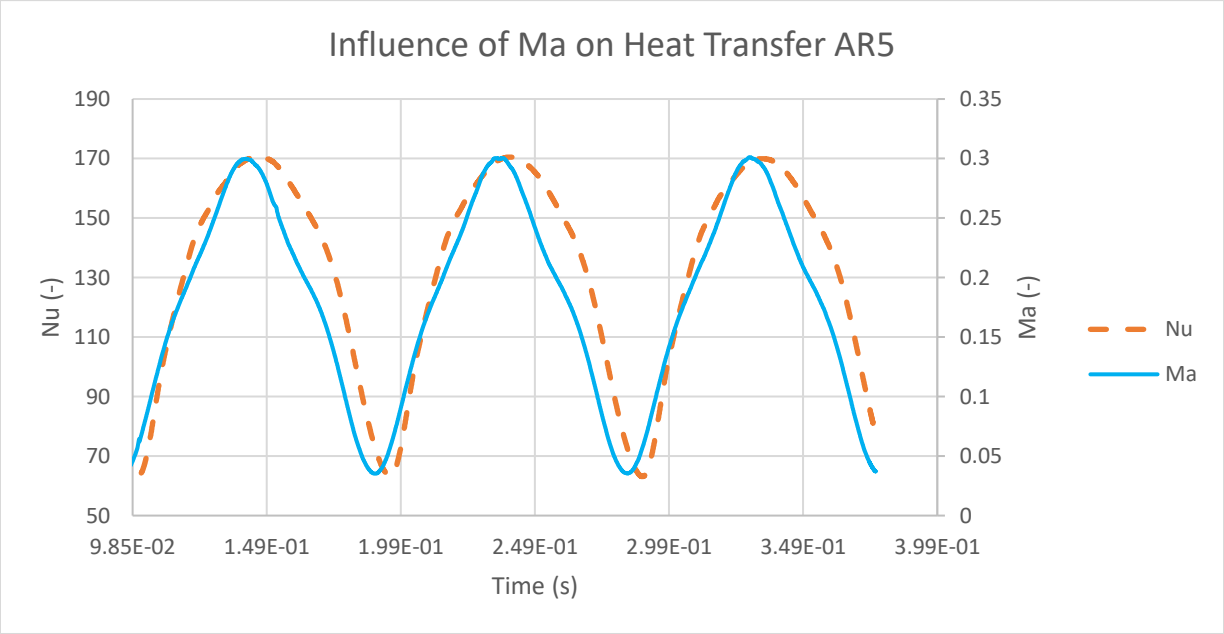

Figure 51: Influence of Ma on Heat Transfer; Re=12k, 10Hz, AR=70%

B. Results at Re=30,000

This section presents CFD results for impingement array heat transfer of mean Re=30k. Table 7 gives the varied parameters for the inlet and target surface boundaries.

Table 7: Re=30k CFD conditions

Cases	Re_{ave} (-)	f (Hz)	AR (%)	x/D (-)	y/D (-)	z/D (-)	q" (W/m)	T_i (k)
Re30k 10Hz AR(70%)	30,000	10	70	3	3	3	5.80E+03	300
Re30k 10Hz AR(34.6%)	30,000	10	34.6	3	3	3	5.80E+03	300
Re30k 10Hz AR(17.3%)	30,000	10	17.3	3	3	3	5.80E+03	300
Re30k 20Hz AR(17.3%)	30,000	20	17.3	3	3	3	5.80E+03	300
Re 30k 5Hz AR(17.3%)	30,000	5	17.3	3	3	3	5.80E+03	300
Re 30k 2Hz AR(17.3%)	30,000	2	17.3	3	3	3	5.80E+03	300
Re 30k Steady	30,000	0	0	3	3	3	5.80E+03	300

1. Influence of Frequency

Four coolant flow frequency variations are compared to steady coolant flow conditions for determining the effectiveness of frequency on heat transfer efficiency. Coolant flow frequencies of 2Hz, 5Hz, 10Hz, and 20Hz are presented with steady flow in Figure 52. The presence of pulsed flow for frequencies less than 20Hz is seen to marginally decrease the heat transfer and 20Hz pulsed flow shows a negligible increase in span-wise Nu.

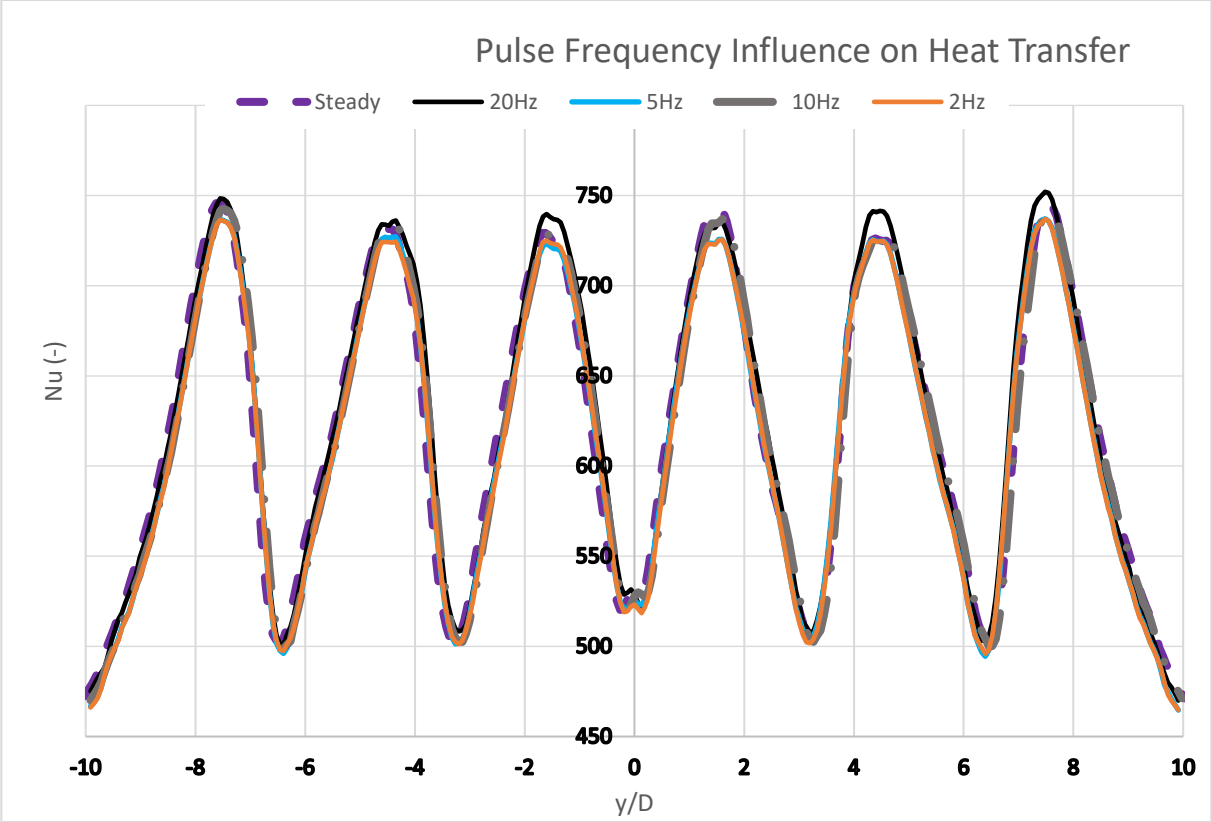

Figure 52: Influence of frequency on Nu, Re=30k, AR=17.3%

Figure 53 presents the area averaged Nu and PCR as a function of pulse frequency. The span-wise Nu is seen to decrease sharply at a frequency of 2Hz and rise with a further increase of frequency. The presence of pulsed flow introduces an increased power consumption of over 35% and appears to decay slowly as frequency is increased. The maximum increase in Nu occurs at 20Hz and is equivalent to nearly 1% of the steady flow Nu. This 1% increase in Nu comes at the cost of a 35% increase in required power to produce the pulse effect. The ER is given in Figure 54. ER is shown to decrease at low Str. (for Str.=2.9e-4 corresponding to 2Hz pulsed flow) and increases with the further increase of pulse frequency until it reaches a maximum at 20Hz.

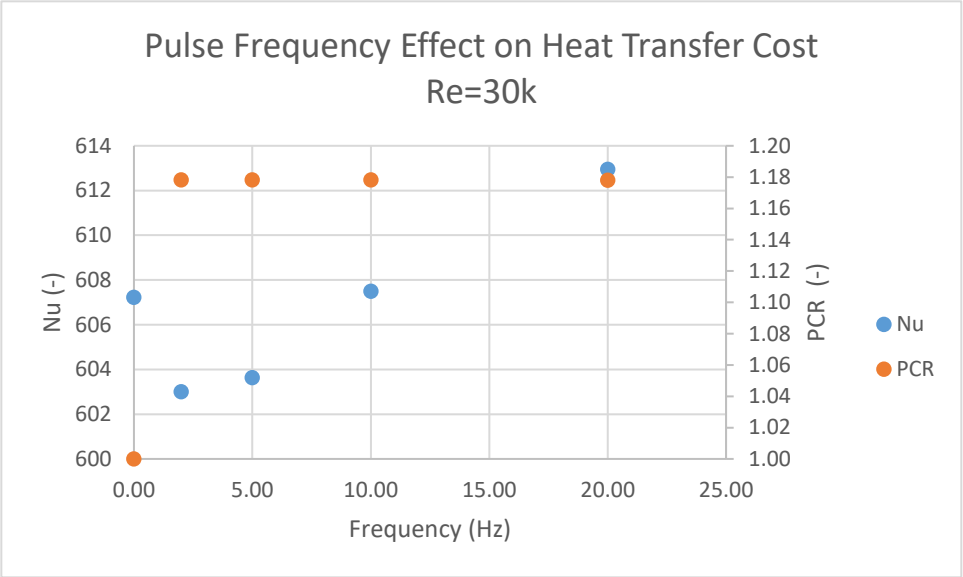

Figure 53: Coolant frequency influence on heat transfer; Re=30k, AR=17.3%

Figure 55 (a)-(e) shows the temporal averaged Nu plots for the frequency cases. Each case shows regions of Nu minimum between strong jet pairs with adjacent weak jets.

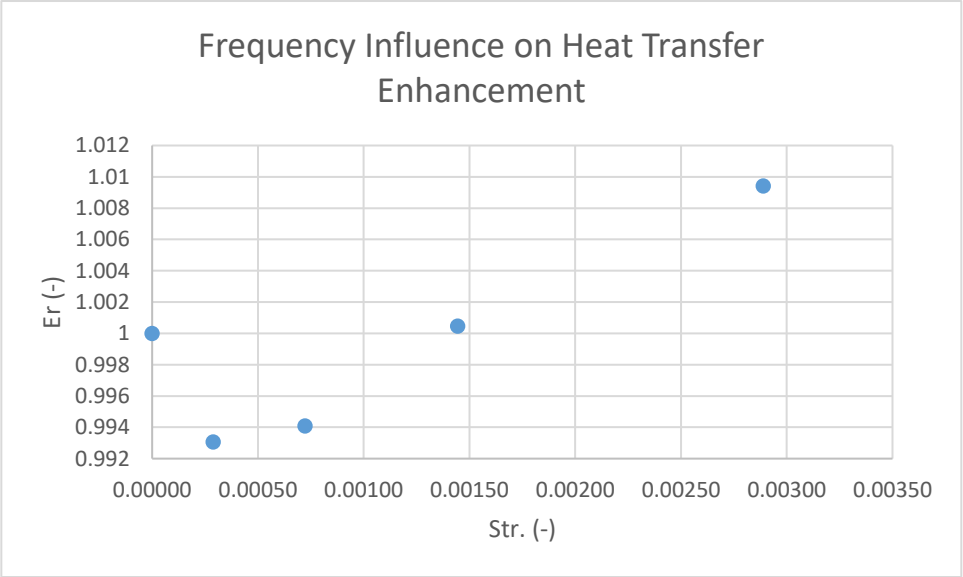

Figure 54: Pulse frequency effect on Heat Enhancement Ratio; Re=30k, AR=17.3%

a)

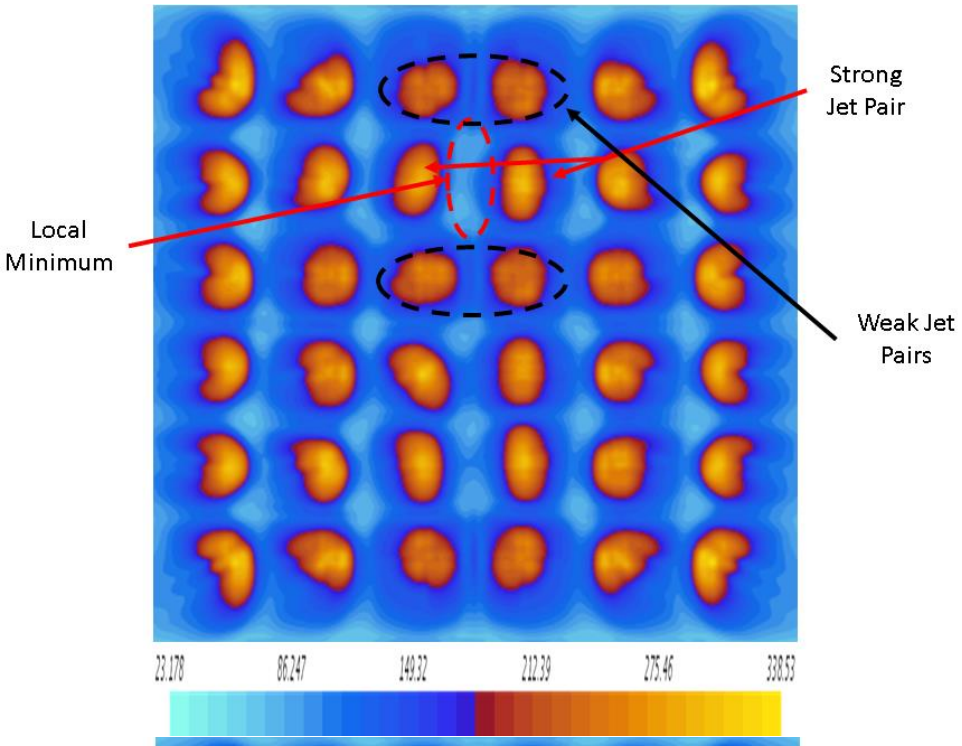
Strong
Jet Pair
Local
Minimum
Weak Jet
Pairs
23.178
86.247
149.32
212.39
275.46
338.53

b)

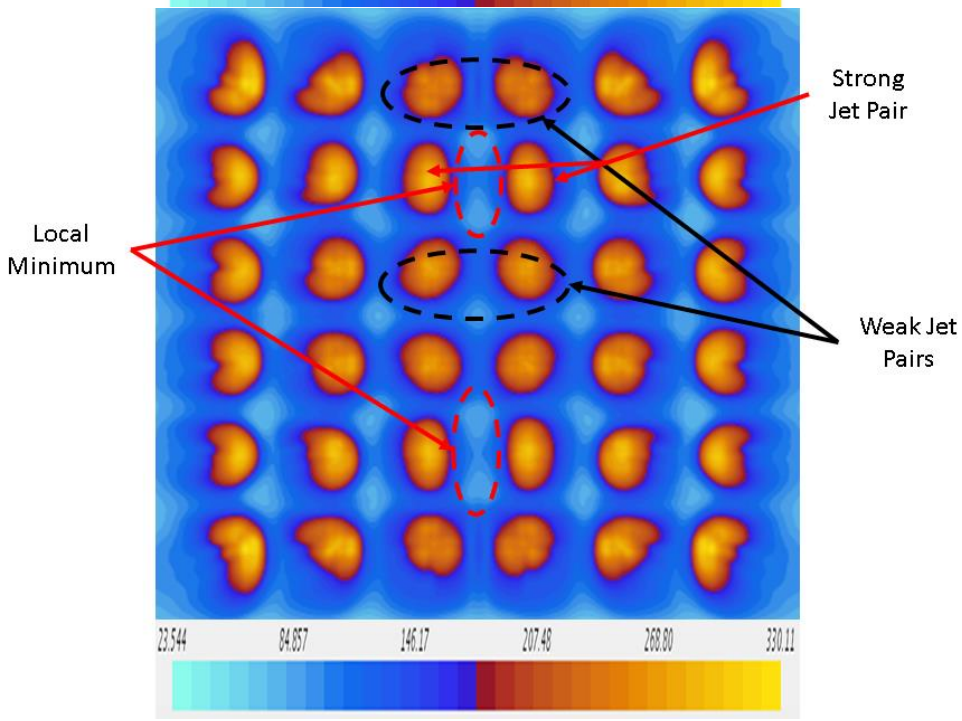
Strong
Jet Pair
Local
Minimum
Weak Jet
Pairs
23.544
84.857
146.17
207.48
268.80
330.11

c)

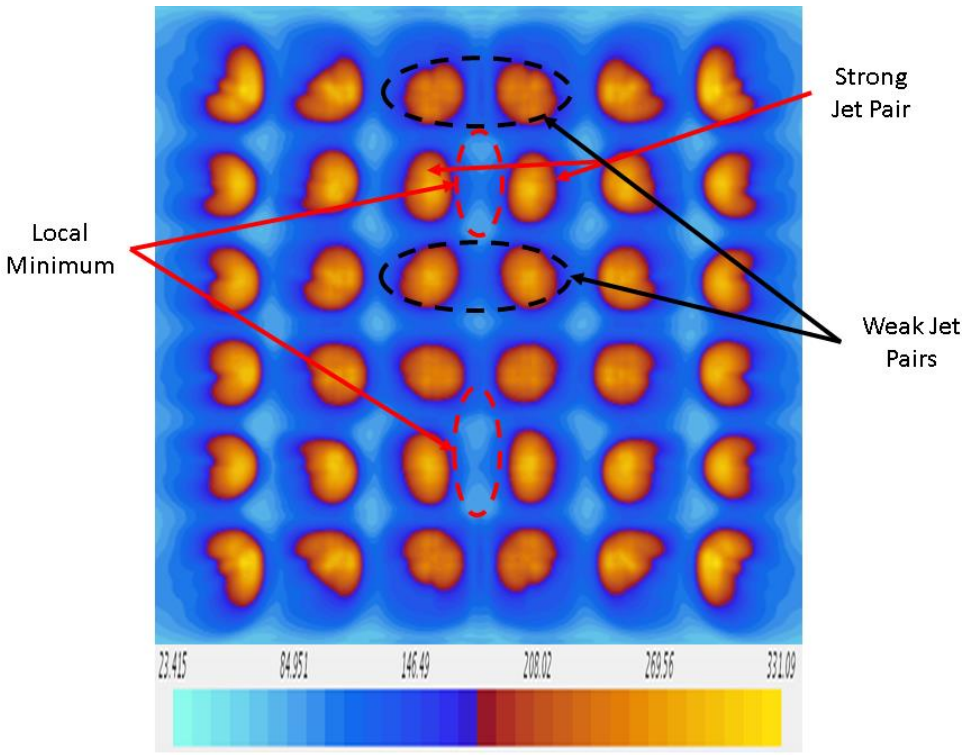
Strong
Jet Pair
Local
Minimum
Weak Jet
Pairs
23.415
84.951
146.49
208.02
269.56
331.09

d)

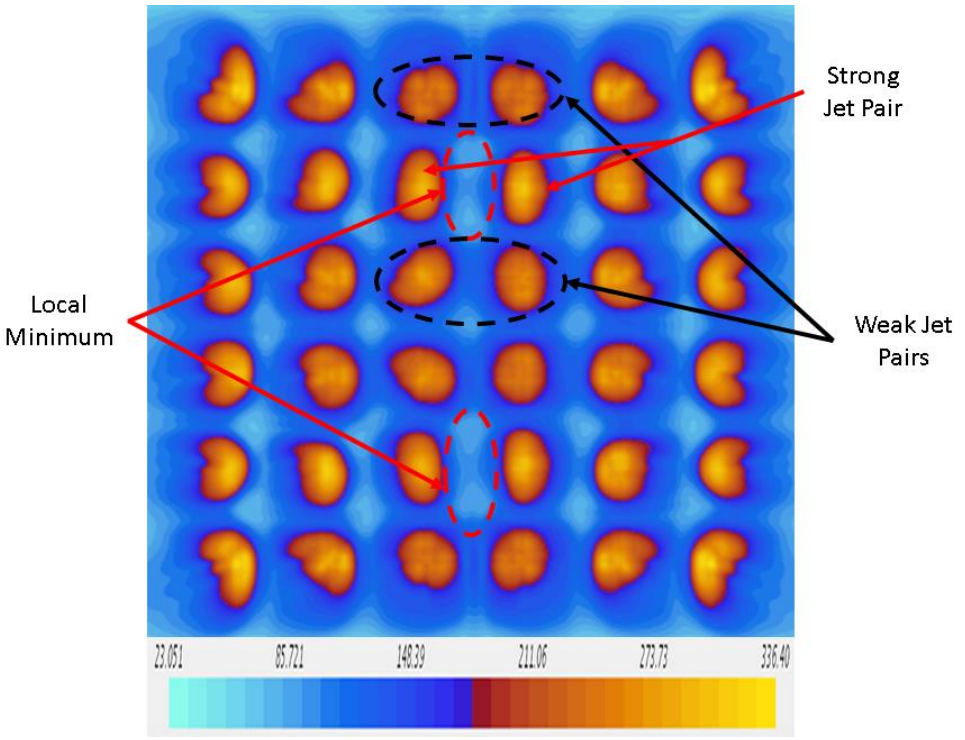
Strong
Jet Pair
Local
Minimum
Weak Jet
Pairs
23.051
85.721
148.39
211.06
273.73
336.40

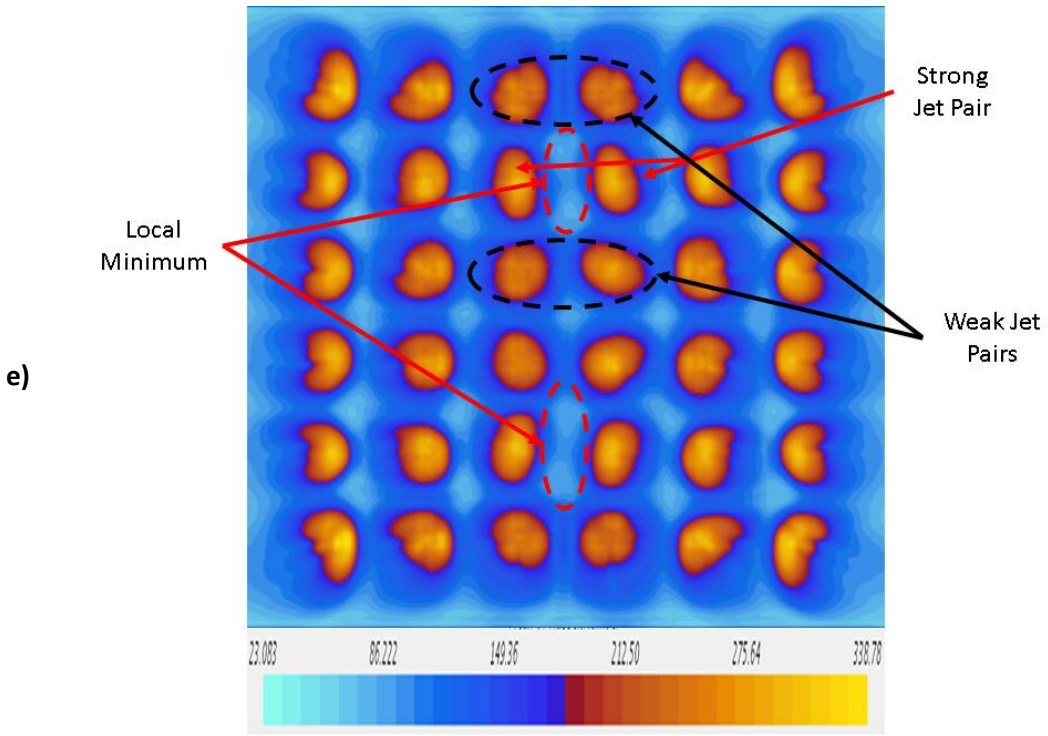

Figure 55: Temporal average Nu varied frequencies, Re=30k, AR=17.2%; (a) Steady flow, (b) 2Hz, (c) 5Hz, (d) 10Hz, and (e) 20Hz

2. Influence of Amplitude

Three simulation cases with varied amplitude ratios are compared with steady coolant flow to evaluate the influence of pulse flow on impingement heat transfer. Amplitude ratios of 17.3, 34.6, and 70. The amplitude studies were performed at a pulse frequency of 10Hz and are compared on a temporal average Nu basis for a span-wise average distribution as shown in Figure 56. The AR(17.3%) case is observed to have nearly identical Nu performance as the steady flow case. The increase in amplitude to AR(34.6%) brings a general rise in Span-wise Nu. Further increase of AR to 70% produces an approximate decrease in Nu of 20% from steady flow conditions. The Sta. values indicate the heat transfer performance in relation to the thermal capacity of the coolant. The coolant thermal capacity on a temporal average basis was constant between each case while a sharp decrease in Nu,ave resulted in the reduction in Sta.

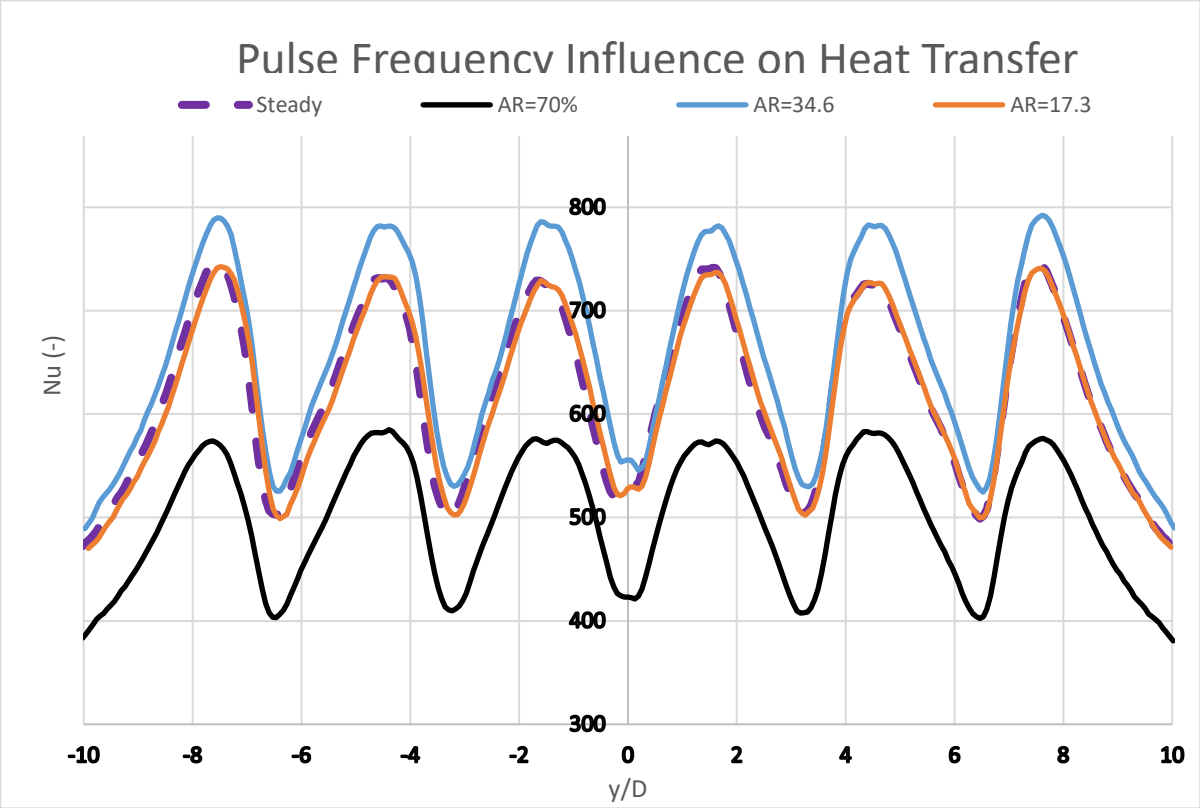

Figure 56: Influence of Amplitude on heat transfer efficiency, Re=30k, Steady and 10Hz

Figure 57 gives the temporal and area averaged Nu and PCR for the variation of pulse amplitude. A linear increase in PCR is seen with an increase in amplitude ratio. Creating pulsed flow with an AR(17.%) pulse amplitude ratio shows negligible in temporal and area averaged Nu. Increasing the amplitude ratio to 34.6% gives a modest increase of 4.32% but this increase is achieved at a 44% increase in PCR. Increasing AR to 70% increases PCR by 98% and results in a 21. 8% decrease in the temporal area averaged Nu. The ER plot for variation of amplitude is given in Figure 58 and more readily displays the negative impact of pulsed flow on heat transfer. No increase is seen for AR(17.3%) with a minimal increase of nearly 4% as the amplitude is increased to AR(34.6%). Further increase of flow amplitude leads to a sharp decrease in ER as seen with AR(70%).

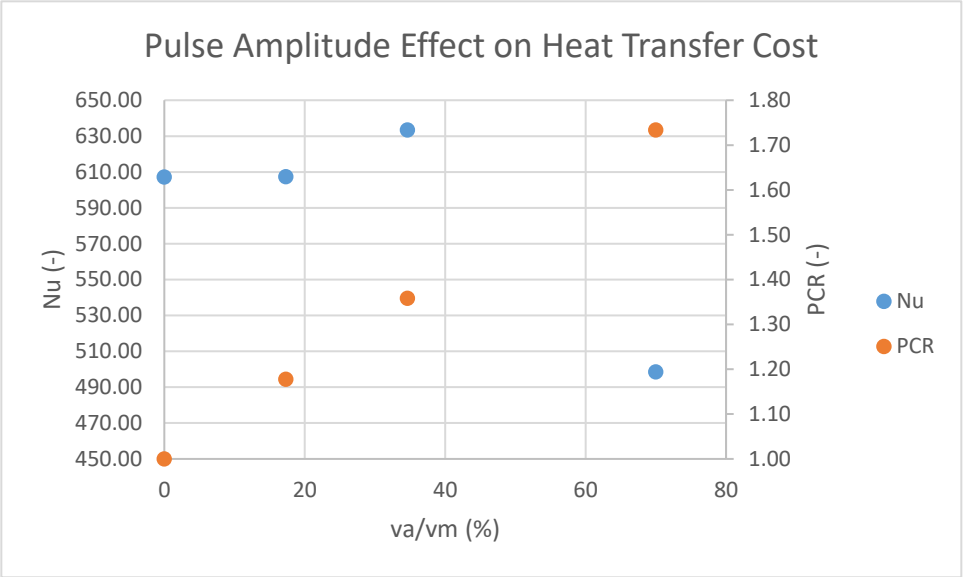

Figure 57: Bulk coolant heat transfer efficiency amplitude dependence; Re=30k, 10Hz

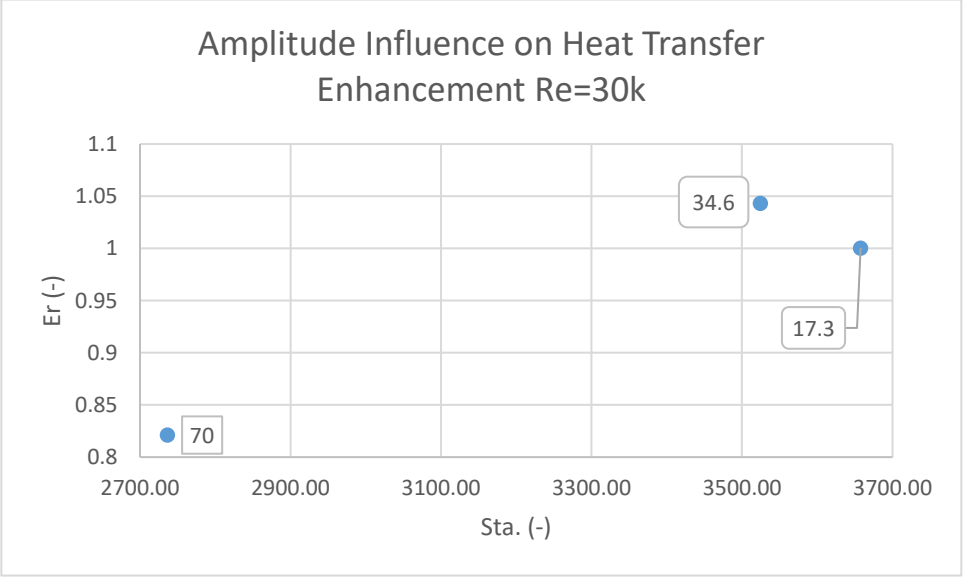

Figure 58: Amplitude influence on Heat Transfer Efficiency; Re=30k, Steady and 10Hz

The temporal averaged Nu plots for amplitude influence amplitude rations 0-70% are given Figure 59 (a)-(d). The presence of regions of Nu minimums between upstream strong jets is clearly shown for each Nu plot. The minimums in Figure 59 (c) shift down a row and Figure 59 (d) has only one Nu minimum.

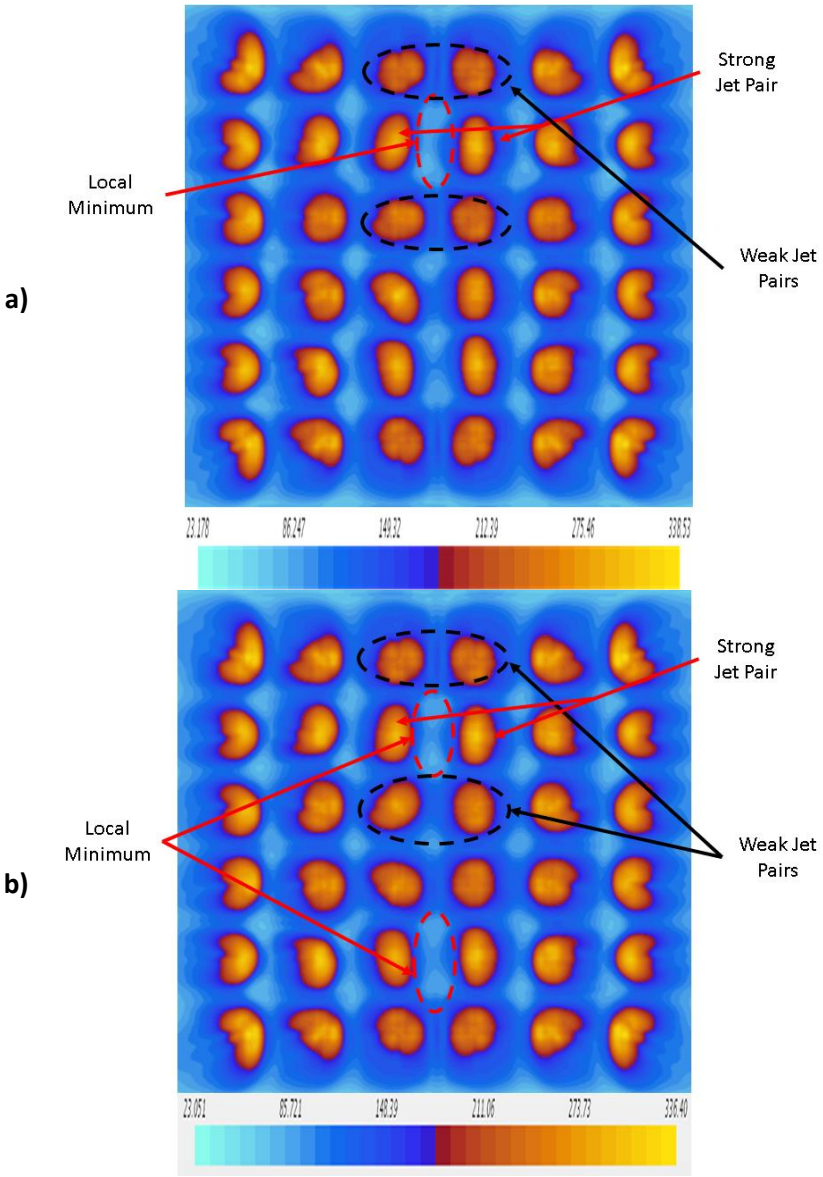
a)
Strong
Jet Pair
Local
Minimum
Weak Jet
Pairs
23.178
86.247
149.32
212.39
275.46
338.53
b)
Strong
Jet Pair
Local
Minimum
Weak Jet
Pairs
23.051
85.721
148.39
211.06
273.73
336.40

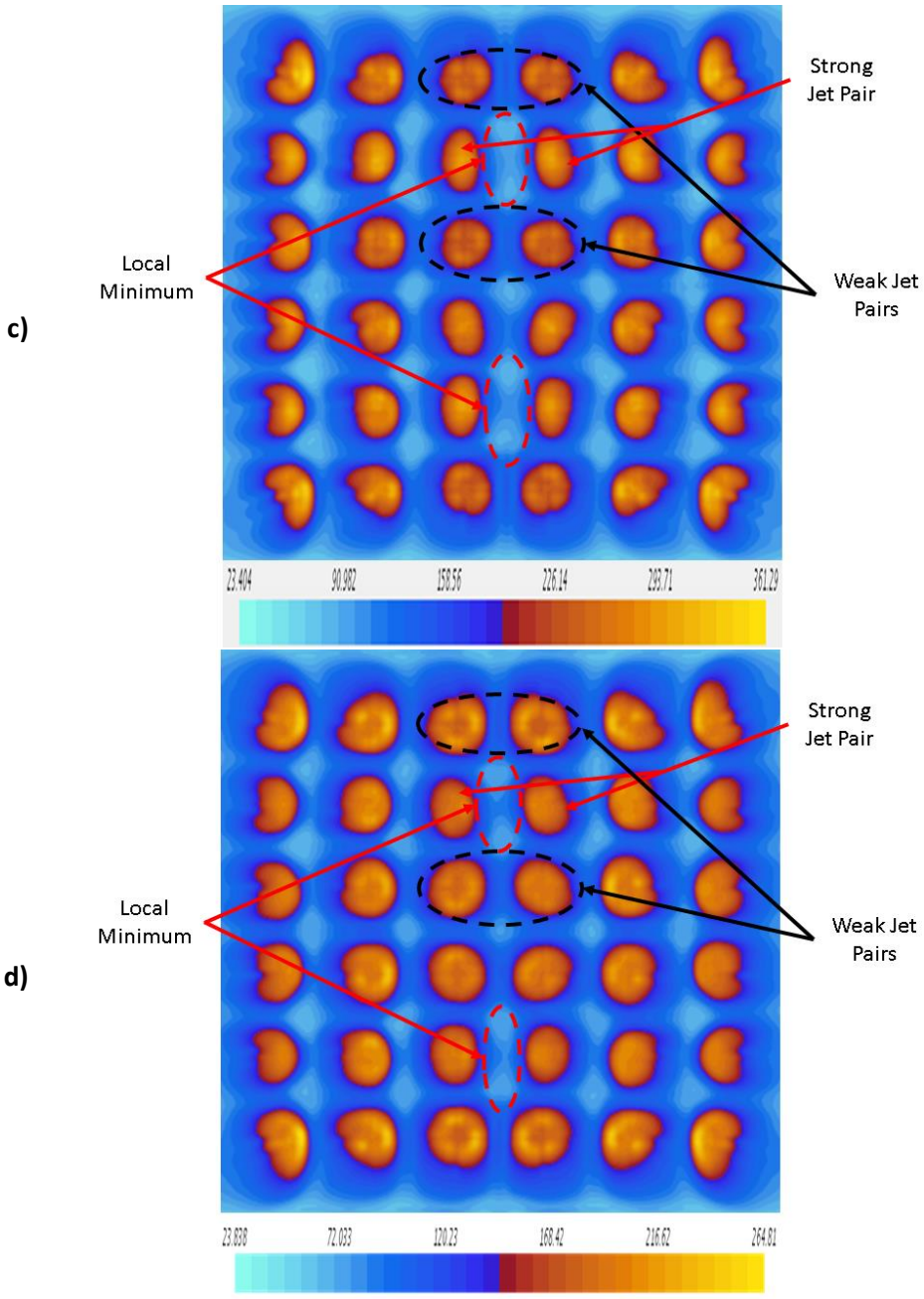

Figure 59: Temporal averaged Nu with varied amplitudes, Re=30k; frequency flows at 10Hz, (a) Steady flow, (b) AR(17.3), (c) AR(34.6), (d) AR(70)

3. Flow Behavior

The temporal mean distribution of the Mach Number is given in igure 60. The region of highest Mach number occurs in the nozzles with a mean Ma >0.3 indicating the coolant air is expected to no longer behave strictly as an incompressible fluid. The temporal-mean pressure

distribution presented in igure 60 shows circulation induced pressure drops on the edge of the nozzle entrance and high pressure at the stagnation region as the flow impinges on the surface and changes to a radial direction. Figure 62 presents the velocity distribution on a stream-wise section intersecting one inner jet row. Important flow patterns include entrained vortex pair between the two upstream jets, the presence of the stagnation zone, and the development of the wall jet. A notable occurrence is seen in the decrease in entrained vortices between jets with downstream progression. This decrease indicates the deflection of downstream jets is not due to the presence of the vortices but rather the increase in mass flow with the downstream progression that deflects the jets.

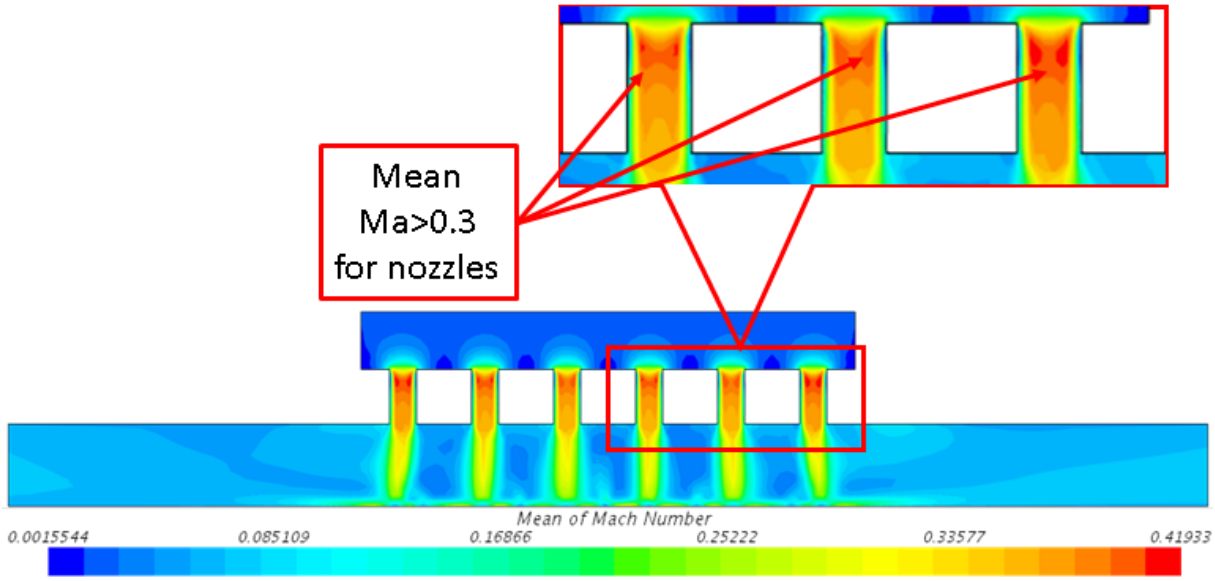

igure 60: Sectional distribution of mean Ma. Number, Re=30k, steady flow

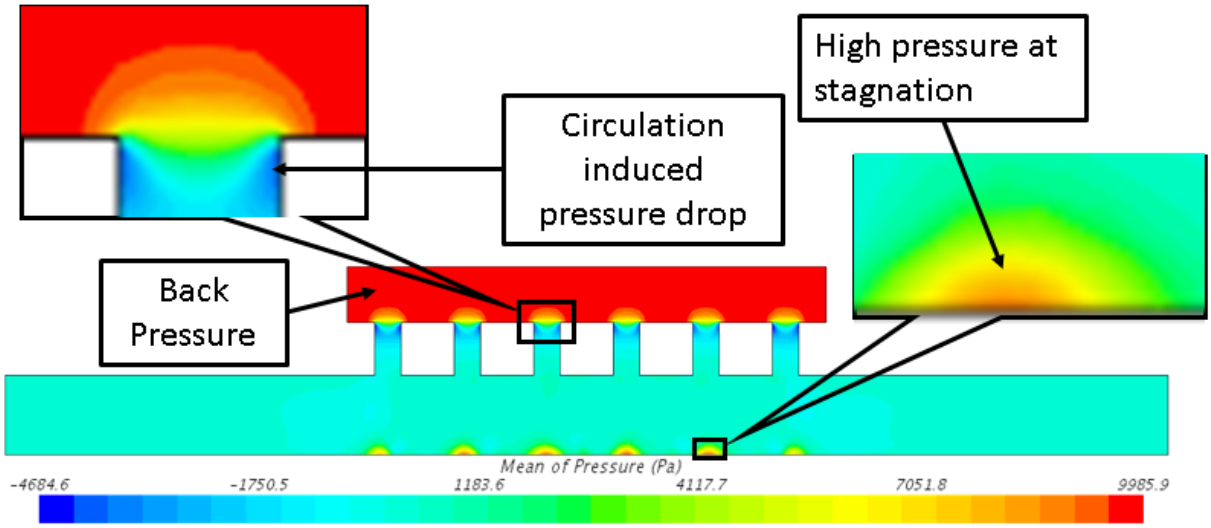

Figure 61: Sectional pressure distribution: Re=30k, steady flow

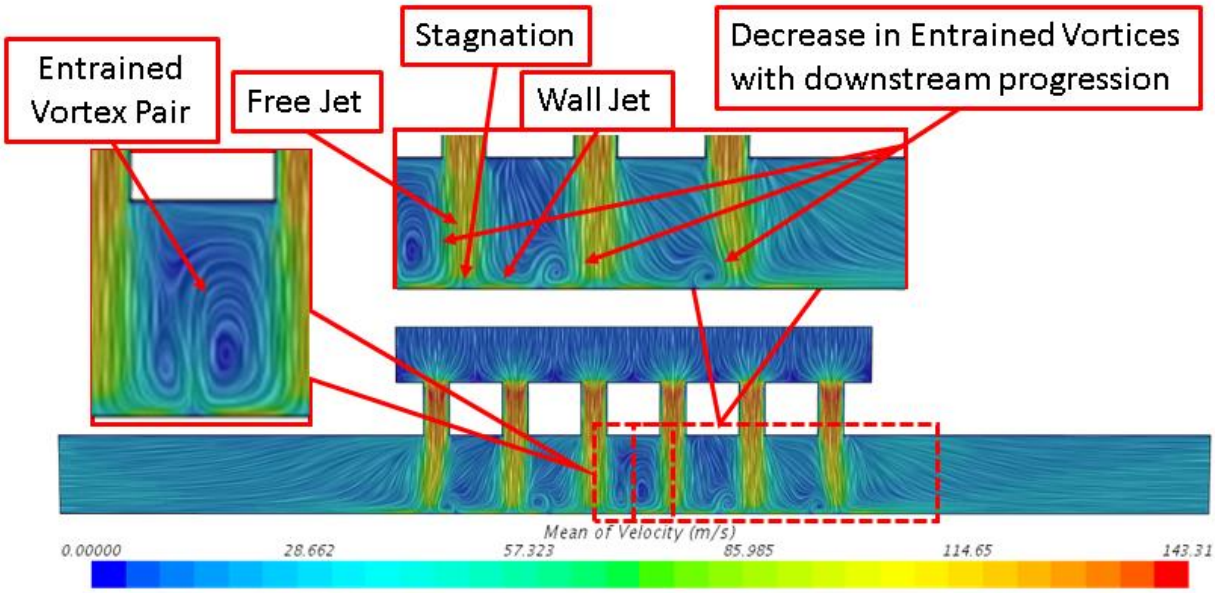

Figure 62: Sectional velocity distribution, Re=30k, steady flow

The temporal mean span-wise Nu and Max Nu are given in Figure 63 for various ARs. Nearly a 20% increase in Nu is seen by decreasing AR by roughly 50% then a decrease in Nu is seen for AR=17.3 which returns to steady coolant Nu levels. The Ma corresponding to the low Nu for AR=70 exceeds 0.7 indicating compressibility may be a factor in the decrease in Nu. Figure 64 through Figure 66 plot the maximum Ma with $Nu_{s,ave}$ as a function of time. The mean Nu here is

taken over the entire target surface boundary rather than in the impingement region and is given merely as qualitative. A more in-depth description of the change in heat transfer behavior with the increase of Ma is given through temporal plots of Nu and Ma for the varied amplitude cases in Figure 64 through Figure 66. The first unique behavior is seen in Figure 64 where the Nu is no longer proportionate to the temporal magnitude of the mass flow waveform as indicated by the inverse behavior compared with the Ma and Nu temporal plots for mean Re=30k. As AR is increased from 17.3 to 34.6 the resulting increase in Ma variation is shown in Figure 65 to produce increased complexity in the Nu relation to max Ma. Through evaluation of the two Nu cycle maximums and one minimum the behavior appears to be related certain Ma values that would indicate either the dominance of compressibility or incompressible flow. The cycle begins with Nu decreasing and Ma at its' minimum. As Ma increases to near 0.29 Nu hits a minimum and increases with increase in mass flow rate. As Ma reaches 0.35 Nu hits maximum and begins to decrease. Nu continues to decrease until Ma reaches its' peak and then Nu increase in proportionl to the decrease in mass flow. Nu increases to a maximum when Ma reaches 0.33 then decreases to finish the cycle. This maximum at 0.33 would indicate that the effect of compressibility ceases and a decrease in mass flow begins to dominate the heat transfer interaction. Similar behavior is shown in Figure 66 where the cycle with Ma at its' minimum with Nu rapidly decreasing. Nu reaches its' first minimum with a short lag behind Ma. Nu increases in the increase in mass flow until Ma reaches about 0.4 where the effects of compressibility cause Nu to decrease. Nu reaches another minimum as Ma peaks. Nu continue to rise until compressibility ceases to influence heat transfer as Ma reaches 0.3. Nu decreases to finish the cycle.

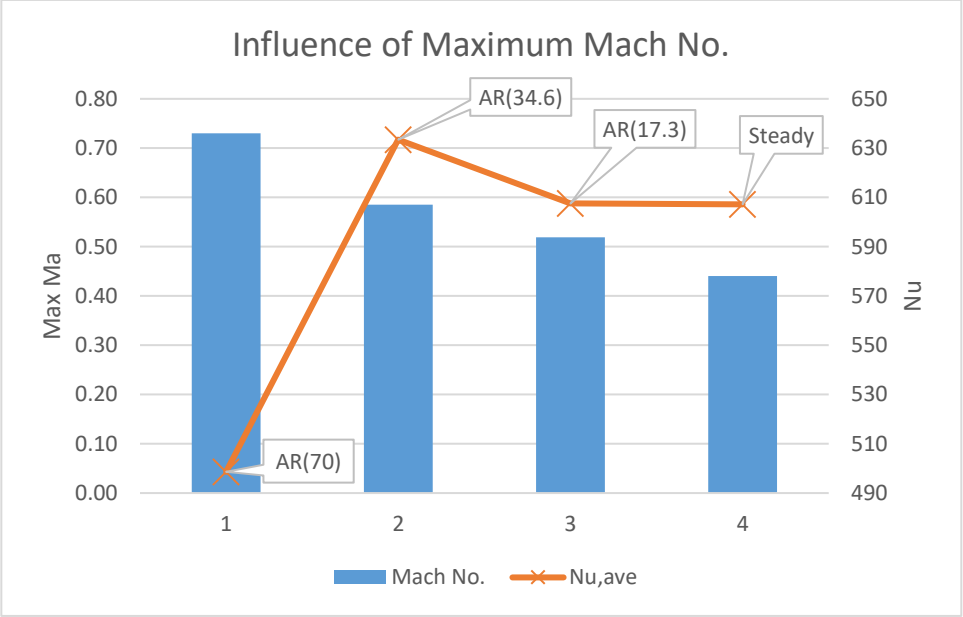

Figure 63: Influence of Ma on heat transfer; Re=30k, 10Hz

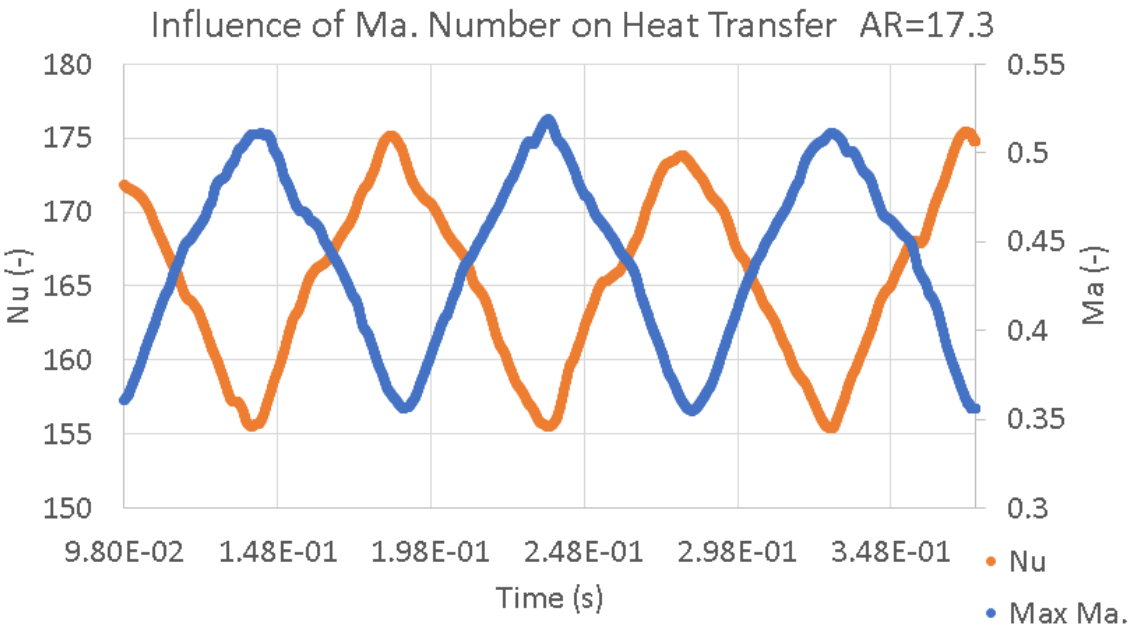

Figure 64: Ma Influence on Heat Transfer; Re=30k, 10Hz, AR=17.3

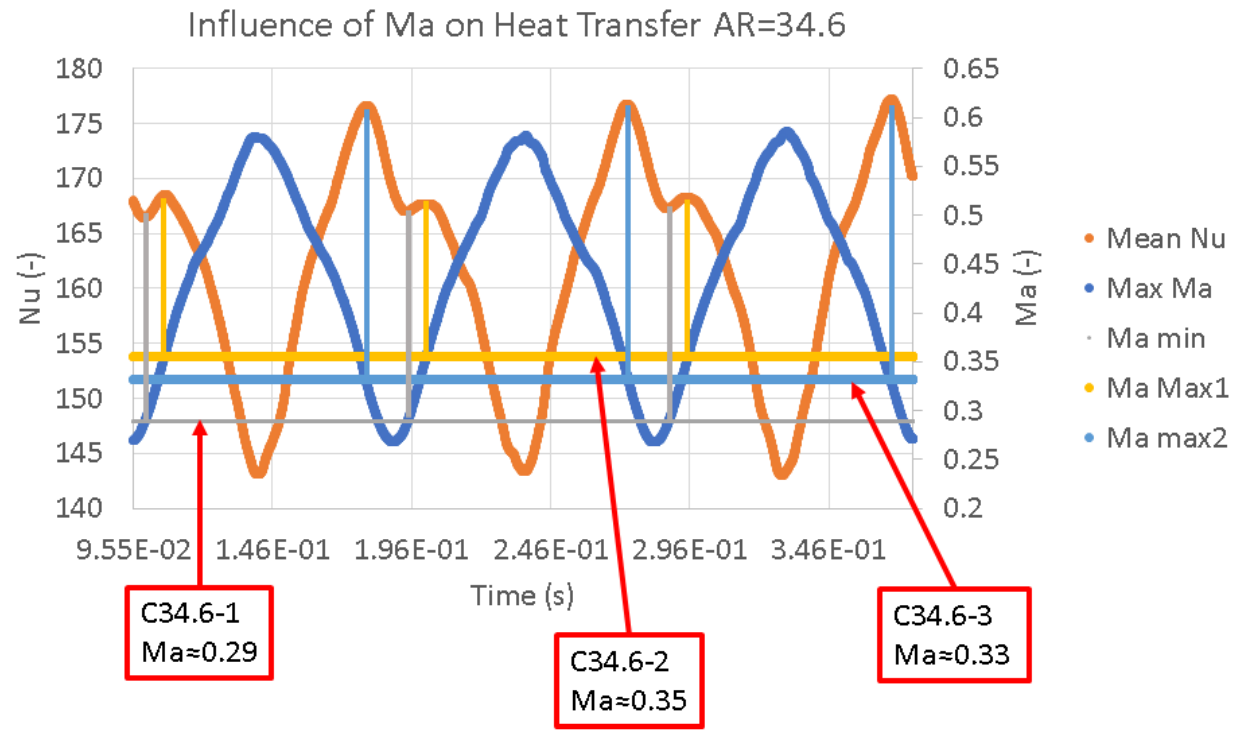

Figure 65: Ma influence on Heat Transfer; Re=30k, 10Hz, AR=34.6

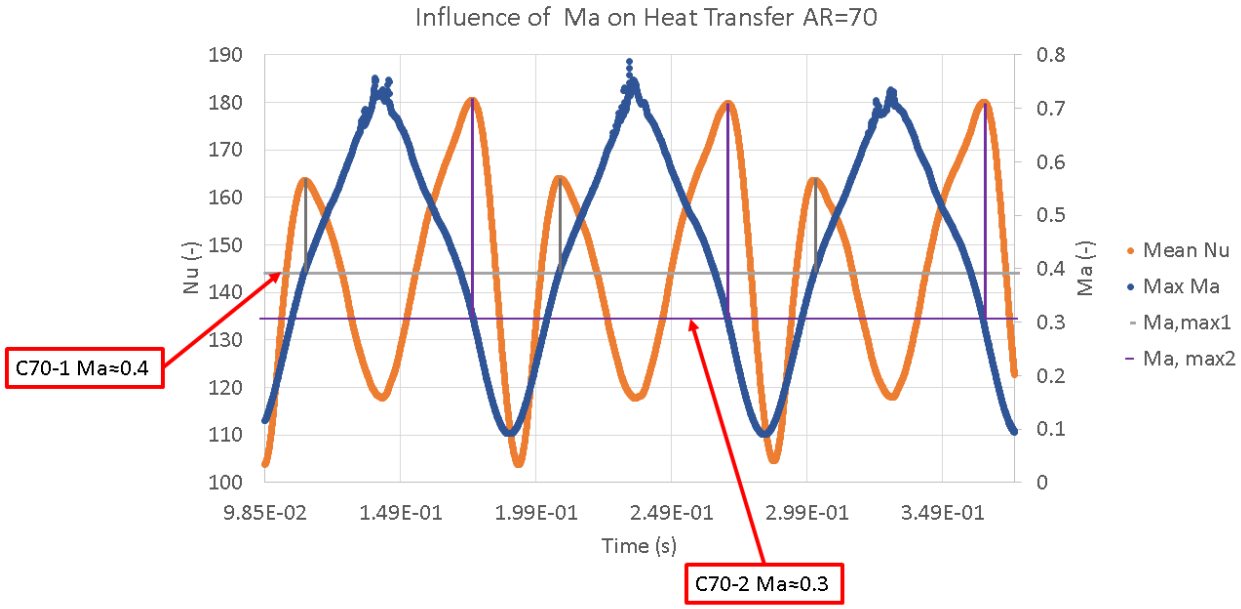

Figure 66: Influence of Ma on Heat Transfer; Re=30k, 10Hz, AR=70

V. Conclusions

Much interest has been placed in researching Jet Impingement Cooling in an effort to produce new impingement cooling schemes that provide more efficient means for removing heat from thermally critical surfaces. Some recent developments in impinging research have sought to demonstrate the possibility of increasing heat transfer efficiency by introducing various pulse coolant flow configurations. Some qualitative research has shown what appears as promising results in enhanced heat transfer through introducing pulse coolant flows. This study and others do not observe promising results for increased heat transfer, but observe reductions in heat transfer efficiency with the introduction of pulsed flow.

The operating range for which the results of this research are applicable applies to pulse coolant jet impingement flows with semi-confined configurations. The applicable flow extends to temporal averaged Reynolds flows of 12,000 and 30,000 with a damped pulse waveform. The applicable wave properties include frequencies ranging 0-20Hz and amplitude ratios 0-70.

The specific concluding remarks from this research are as follows:

1. Theoretical square or intermittent waveforms are unrealistic for coolant mass flow boundary conditions for pulse impingement flows for approaching 1Hz and greater. The physical influence of system drag forces, fluid inertia, and fluid capacitance degrades the waveform beyond representation of the original waveform. A decayed pulse waveform was introduced as a boundary specification for pulse coolant configuration. This has significant implications for the merit of impingement flows since square waveforms were found to be favorable in several CFD studies investigating pulsed flows.

2. Past research in pulse jet impingement cooling has not adequately accounted for the increase in energy consumption as consequence of generating the pulsed flow. A new evaluation parameter is introduced addressing this issue. The Power Consumption Ratio compares the ideal required the fluid power of pulsed flows with temporal averaged equivalent steady flows.
3. The widespread practice of using nozzle diameters as the characteristic dimension for Nu definition in jet impingement flows leads to the introduction of bias in the comparison of convective heat transfer efficiency when nozzle diameter varies. Using the standoff distance as the characteristic dimension would mitigate this bias. Additionally, it would introduce consistency with the use of the Strouhal number since the standoff distance limits the size of vortices generated in the impingement channel.
4. Improvements in heat transfer efficiency due to pulse coolant flow schemes must be quantifiable. Quantifiable defined as follows:
    a. Must report temporal-area averaged heat transfer characteristics.
    b. Must demonstrate quantified increase to account for geometric and mechanical system effects due to the addition of pulse coolant schemes
        i. Added components introduce volume and mass mitigating factors
        ii. Pulsed flow system requires increased pressure ratio compared to equivalent steady flow systems.
    c. Must account for the increased lifecycle costs:
        i. Manufacturing due to pulse mechanism and affected components
        ii. Increased maintenance due to presence of the pulse mechanism.

5. Introduction of pulsed flows for temporal averaged flows of Re=12,000 and Re=30,000 show decreased heat transfer efficiency.
    a. For Re=12,000:
        i. A general decrease in heat transfer efficiency was observed as frequency increased. This case against pulsed flows at Re=12,000 is further strengthened by the increase in power consumption of nearly 18% for the lower amplitude cases.
        ii. Increase in fluid amplitude ratio produced an decreased heat transfer efficiency. The increase in amplitude was also seen to increase the PCR.
        iii. Local regions of temporal averaged Nu minimums between strong jet along the upstream centerline. Local minimums had adjacent weak jets and shifted stream-wise with a change in frequency and amplitude ratio. The creation of local minimums and alteration of weak and strong jets is likely due to the presence of flow instabilities and structures in the impingement domain.
    b. Flows of Re=30,000 showed that:
        i. The addition of pulsed flow caused a decrease in heat transfer efficiency at low frequencies a trend that reversed with increase in frequencies above 10Hz. This deviation from steady flow efficiency was less than 1% for increased and decreased exacerbated by increasing the pulse frequency. A sharp drop in heat transfer efficiency. The introduction of

pulse flow increased the power consumption by approximately 18% for the lower amplitude cases.

ii. The heat transfer efficiency response to pulse amplitude showed negligible affect at low amplitude ratio of 17.3%. An increase in heat transfer efficiency of approximately 4% was observed as the amplitude ratio increased to 34.6%. This increase in heat transfer efficiency mitigated by a 36% increase in power consumption. Further increase of amplitude ratio to 70% resulted in a decrease in heat transfer efficiency of nearly 18%.

iii. Local regions of temporal averaged Nusselt Number minimums between strong jet along the upstream centerline. Local minimums had adjacent weak jets and shifted stream-wise with a change in frequency and amplitude ratio. The creation of local minimums and alteration of weak and strong jets is likely due to the presence of flow instabilities and structures in the impingement domain.

iv. The relationship of heat transfer to mass flow amplitude rate was seen to change from purely proportional behavior to an alteration between proportional and inverse based on Mach number magnitude.

VI. References

[1] N. Zuckerman and N. Lior, "Impingement Heat transfer: Correlations and Numerical Modeling," *Journal of Heat Transfer,* vol. 127, pp. 544-552, 2005.

[2] B. Han and R. J. Goldstein, "Jet-Impingement Heat Transfer in Gas Turbine Systems," in *Annals New York Academy of Science*, 2001, pp. 147-161.

[3] T. O'Donovan and D. Murry, "Jet Impingement Heat Transfer--Part I: Mean and Root-Mean-Square Heat Transfer adn velocity Distributions," *International Journal of Heat and Mass Transfer,* vol. 50, pp. 3291-3301, 2007.

[4] K. Jambunathan, E. Lai, M. A. Moss and B. L. Button, "A Review of Heat Transfer Data for Single Circular Jet Impingement," *International Journal of Heat and Fluid Flow.*

[5] M. Goodro, J. Park, P. Ligrani, M. Fox and H. Moon, "Effects of Mach number and Reynolds number on jet array impingement heat transfer," *International Journal of Jeat and Mass Transfer,* vol. 50, pp. 367-380, 2007.

[6] R. Vinze, S. Chandel, M. Limaye and M. Prabhu, "Effect of Compressibility and Nozzle Configuration on Heat Transfer bt Impinging Air Jet Over a Smooth Plate," *Applied Thermal Engineering,* vol. 101, pp. 293-307, 2016.

[7] Z. Liu and Z. Feng, "Numerical simulation on the effect of jet nozzle position on impingement cooling of gas turbine blade leading edge," *International Journal of Heat and Mass Transfer,* vol. 54, no. 23-24, pp. 4949-4959, 2011.

[8] E. I. Esposito, "Jet Impingement Cooling Configurations for Gas Turbine Combustion," Louisiana State University, 2006.

[9] U. Ghia, A. Schroder and S. Ou, "Experimental Study of an Impingement Cooling Jet Array Using an Infrared Thermography Technique," *Journal of Thermophysics and Heat Transfer,* vol. 26, no. 4, pp. 590-597, 2012.

[10] L. Hai-yong, L. Song-ling, Q. Hong-fu and L. Cun-liang, "Aerodynamic investigation of impingement cooling in a confined channel with staggered jet array arrangement," *Experimental Thermal and Fluid Science,* vol. 48, pp. 184-197, 2013.

[11] M. Fox, J. Lee, P. Ligrani, H. Moon and Z. Ren, "Crossflows from jet array impingement cooling: Hole spacing, target plate distance, Reynolds number effects," *International Journal of Thermal Sciences,* vol. 88, pp. 7-18, 2015.

[12] R. &. S. K. Zulkifli, "Studies on pulse jet impingement heat transfer: flow profile and effect of pulse frequencies on heat transfer," *nternational Journal of Engineering and Technology,* vol. 4, no. 1, pp. 86-94, 2007.

[13] J. L. R. C. K. Victor J. Zimmer, "The Influence of Coolant Unsteadiness on Impingement Heat Transfer," in *ASME Turbo Expo*, Dusseldorf, 2014.

[14] V. T. M. Pakhomov, "Effect of Pulse Frequency on Heat Transfer at the Stagnation Point of an Impinging Turbulent Jet," *Heat And Mass Transfer And Physical Gasdynamics,* pp. 256-261, 2012.

[15] J. Mohammadpour, M. Rajabi-Zargarabadi and A. Mujum, "Effect of Intermittent and Sinusoidal Pulsed Flows on Impingement Heat Transfer from a Concave Surface," *International Journal of Thermal Sciences,* vol. 76, pp. 118-127, 2014.

[16] K. Womack and M. Schultz, "Combined Effects of Wakes and Jet Pulsing on Film Cooling," *Journal of Turbo Machinery,* vol. 130, pp. 041010-1 041010-12, 2008.

[17] M. Fox, J. Haegele, J. Jin, J. Lee, P. Ligrani, H.-k. Moon, G. Potts and . Z. Ren, "Effects of Jet-to-Target Plate Distance and Reynolds Number on Jet Array Impingement Heat Transfer," vol. 136, 2014.

[18] M. Goodro, J. Park, L. P. M. Fox and H. Moon, "Effect of Temperature Ratio on Jet Array Impingement Heat Transfer," *Journal of Heat Transfer,* vol. 131, pp. 012201-1, 012201-10, 2009.

[19] R. Brakmann, L. Chen, B. Weigand and M. Crawford, "Experimental and Numerical Heat Transfer Investigation of an Impinging Jet Array on a Target Plate Roughened by Cubic Micro Pin Fins," *Journal of Turbomachinery,* vol. 138, pp. 111010-1 111010-9, 2016.

[20] P. Penumadu and A. Rao, "Numerical Investigations of Heat Transfer and Pressure Drop Characteristics in Multiple Jet Impingement System," *Applied Thermal Engineering,* vol. 110, pp. 1511-1524, 2017.

[21] M. Can, B. Etemoglu and A. Avci, "Experimental Study of Convective Heat Transfer Under Arrays of Impinging Air Jets from Slots and Circular Holes," *Heat and Mass Transfer,* vol. 38, pp. 251-259, 2002.

[22] FLIR, "Download Manuals and Drawings," 2017. [Online]. Available: http://flir.custhelp.com/app/account/fl_download_manuals/session/L3RpbWUvMTUwNzE3MjIxNi9zaWQvZlV4SFhrVDUzSjJja2hxekxDMk5JODZyeVZ0WCU3RVY3eE1zczFwcHpwQnB2Smtia1hKbER1N0dyUmZMNSU3RWthZHNqN3o5NWRXc1JDZGJWT0VkbWt6RVg1R3gyU3VFNVRYd3U2al84VTRaa2NydGJXU2lrJTdFY3. [Accessed Febrary 2017].

[23] Y. A. Cengel and A. J. Ghajar, Heat and Mass Transfer: Fundamentals & Applications, New York: McGraw Hill, 2011.

[24] MathWorks Inc, *MATLAB 2016 &2017,* Natick, 2017.

[25] M. Paz and B. Jubran, "Numerical Modeling of Multi Micro Jet Impingement Cooling of a Three Dimensional Turbine Vane," *Heat Mass Transfer,* vol. 47, pp. 1561-1579, 2011.

[26] R. Moffat, "Describing the Uncertainties in Experimental Results," *Experimental Thermal and Fluid Science,* vol. 52, pp. 3-17, 1088.

[27] SIEMENS, "STAR-CCM+," SIEMENS, 2017. [Online]. Available: https://mdx.plm.automation.siemens.com/star-ccm-plus.

[28] V. Zimmer, J. Rutledge, C. Knieriem and S. Ou, "The Influence of Coolant Unsteadiness on Impingement Heat Transfer," in *ASME Turbo Expo*, Dusseldorf, 2014.

[29] M. Keenan, R. Amano and S. Ou, "Study of an Impingement Cooling Array for Turbine Blade Cooling with Single and Double Exit Cases," in *ASME Turbo Expo*, Aan Antonio, 2013.

[30] P. Cohen, M. Herniou and J. Weng, "Camera Calibration with Distortion Models and Accuracy Evaluation," *IEEE Transactions On Pattern Analysis and Machine Intelligence,* vol. 14, no. 10, pp. 965-979, 1992.

VII. Appendix A: Calibration

1. Camera Calibration Procedure

Camera Lens Distortion Calibration Procedure and Calibration Sets

2. Why is Lens Calibration Necessary?

Manufacturing processes of camera and lenses lead to the distortion of real images [30]. The A35 FLIR research camera is observed to have lens construction or assembly defects evidenced through negative geometric image distortion (or barrel distortion). Figure 67 shows the radial distortion of a square checkered patterned sticker.

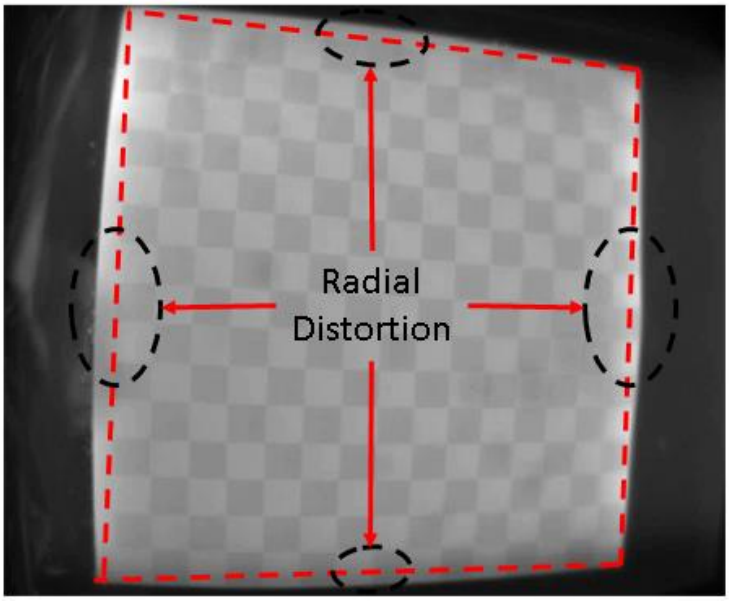

Figure 67:Checkerboard image distortion example; radial distortion annotated

3. Overview of Infrared lens calibration process

The following is a description of processed developed to calibrate and undistort the images taken by the A35 FLIR camera.

4. Physical setup and preparation

The accuracy of camera calibration parameters is improved through using images from several different camera orientations. Three different orientations were used for this calibration as shown in Figure 68.

The following sequence was used to perform the calibration:

1. The camera lens was cleaned using a damp gauss with 70% isopropyl rubbing alcohol. The lens was allowed to set for several minutes till the alcohol had completely evaporated.
2. The camera was positioned in orientation (1).
3. The lens was adjusted to bring the target surface into focus. Note: the lens was not adjusted after this point since the target surface remained in focus at the other orientations.
4. The camera was allowed to reaching operating conditions. A minimum of five minutes was used as recommended by FLIR Systems.
5. The target surface was brought to an elevated temperature equilibrium. The power source was turned on and the surface temperature was monitored until the target surface temperature stopped rising.
6. A video clip was captured using FLIR's IR research software and exported for processing. Note: each video segment was cataloged according to the camera orientation.
7. The video files were segmented into individual images using Photron's FASTCAM Viewer.

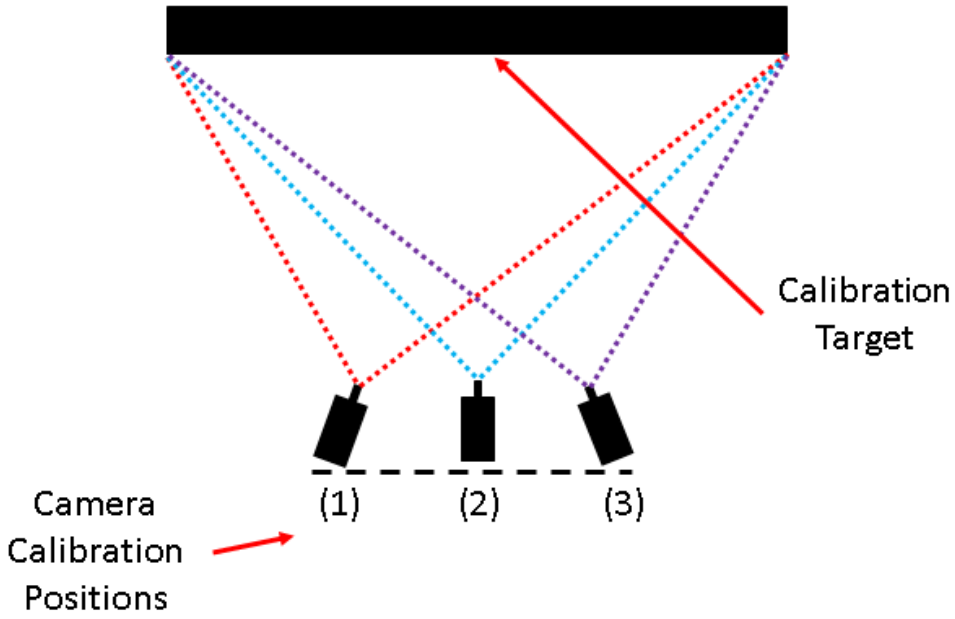

Figure 68: Calibration setup

5. Calibration set results and evaluations

The following discusses the calibration sets used in the Jet Impingement Research

Calibration set February 09 2017

Target and camera configuration

The calibration surface was created using 304 Stainless Steel foil as the heated surface. The foil surface was cleaned using Isopropyl rubbing alcohol before applying the checker pattern. The checker pattern was generated using a checker pattern stencil and several coats of Krylon's Ultra-Flat black paint. Following the painting process the excess paint was removed to produce a defined checker pattern. Figure 69 shows the finished checker pattern used for the calibration. Three sets of images were obtained for three different orientations as described in the calibration setup procedure.

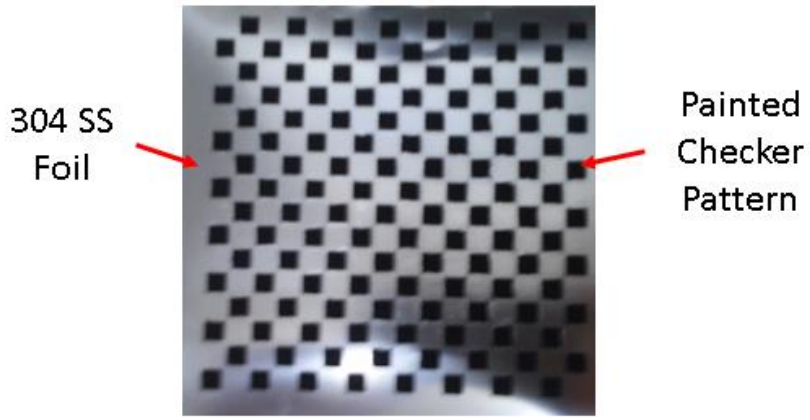

Figure 69: Calibration surface

The images were processed using MATLAB's calibration app. The resulting mean pixel error for the calibration was 0.21% which is less than half the recommended mean pixel error of 0.5%.

A test was conducted to evaluate the effectiveness of the calibration images. Using the same setup procedure used in the calibration tests, an IR video recording of a uniform black surface was taken. Note the surface given in Figure 70 has a rectangular form with a few irregularities on the edges.

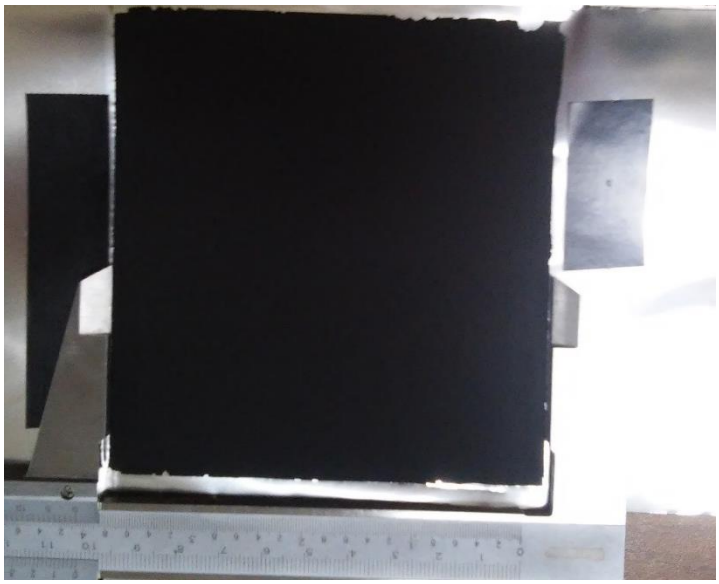

Figure 70:Test solid black pattern

Calibration implementation

The resulting images were processed using the MATLAB user script above. Figure 71 shows a distorted image for evaluating the calibration's effectiveness. It is obvious that radial distortion is present in this images by the barreled edges which should be effectively straight. The undistorted image is given in Figure 72. The edges no longer have a barreled look and the profiles is a reasonable match of edge profile shown in Figure 70.

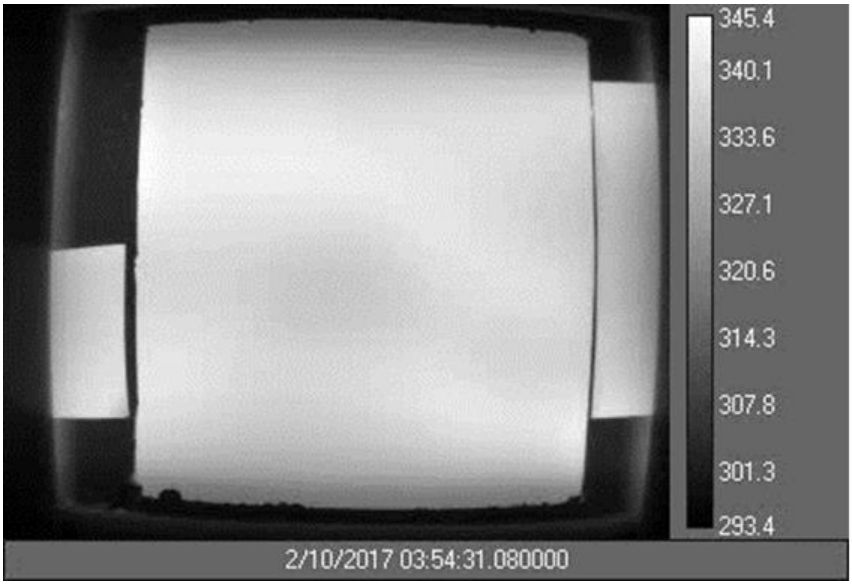

Figure 71:Distorted test image

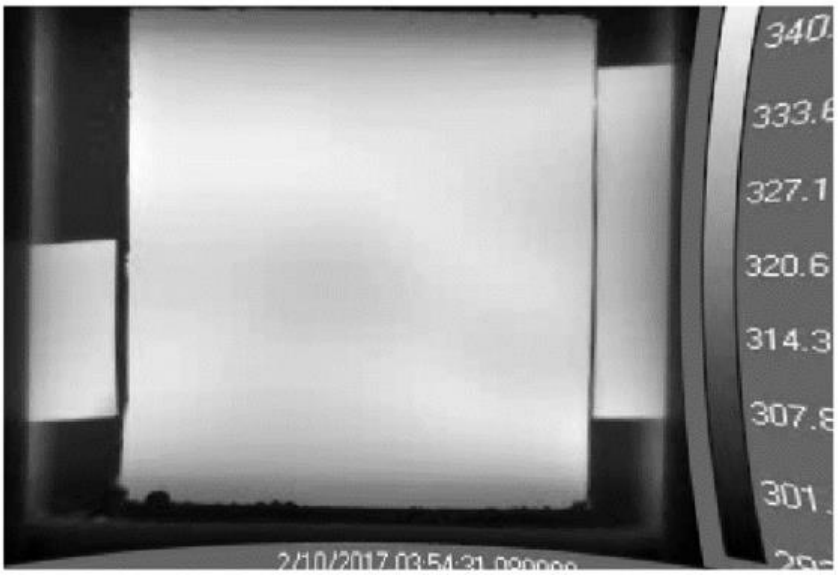

Figure 72:Undistorted test image

An experimental test was conducted to evaluate the effectiveness of the calibration script with the emissivity corrected impingement images. Figure 73 shows a temperature distribution as captured. The radial distortion is clear in this image. In Figure 74 the radial distort is largely removed. The improvement in distortion is sufficient for conducting future experimental test.

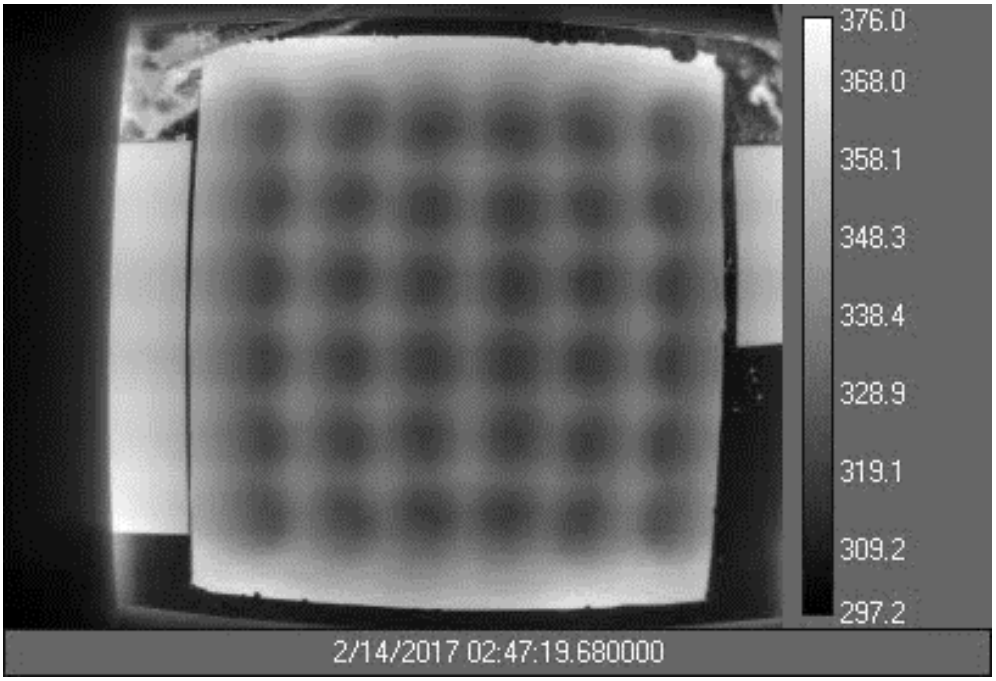

Figure 73:Impingement temperature distribution before correcting radial distortion

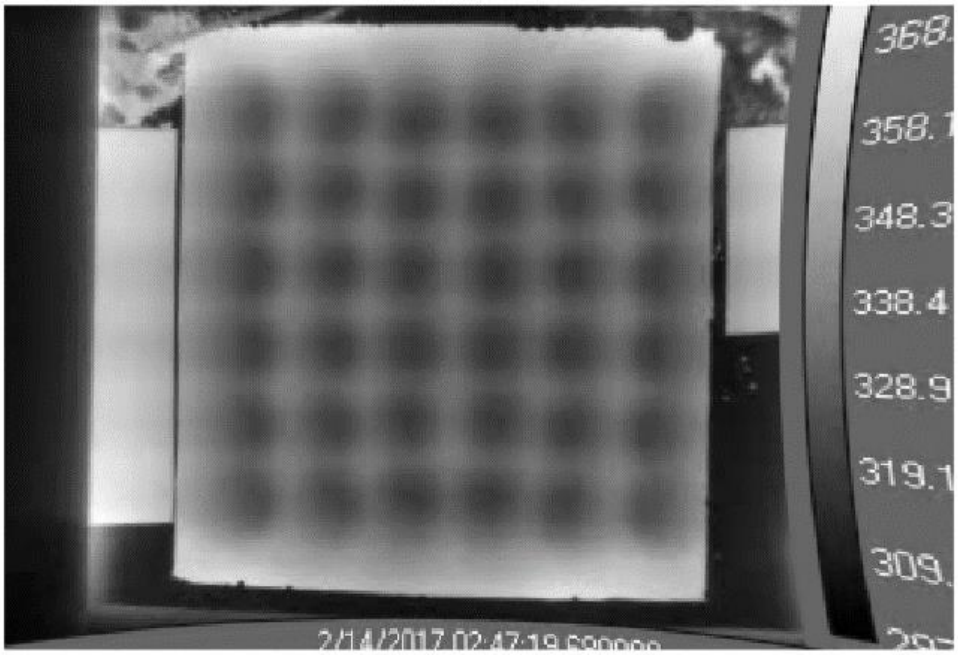

Figure 74: Impingement temperature distribution after correcting for radial distortion

VIII. Appendix B: Data Analysis Codes

1. Lens Undistortion Codes

```
function JetIimpingement_03
% Define images to process
imageFileNames = {'Calibration Images Path Here'};

% Detect checkerboards in images
[imagePoints, boardSize, imagesUsed] =
detectCheckerboardPoints(imageFileNames);
imageFileNames = imageFileNames(imagesUsed);

% Generate world coordinates of the corners of the squares
squareSize = 5;  % in units of 'mm'
worldPoints = generateCheckerboardPoints(boardSize, squareSize);

% Calibrate the camera
[cameraParams, imagesUsed, estimationErrors] =
estimateCameraParameters(imagePoints, worldPoints, ...
    'EstimateSkew', false, 'EstimateTangentialDistortion', false, ...
    'NumRadialDistortionCoefficients', 2, 'WorldUnits', 'mm', ...
    'InitialIntrinsicMatrix', [], 'InitialRadialDistortion', []);

% View reprojection errors
%h1=figure; showReprojectionErrors(cameraParams);

% Visualize pattern locations
%h2=figure; showExtrinsics(cameraParams, 'CameraCentric');

% Display parameter estimation errors
%displayErrors(estimationErrors, cameraParams);

sdirectory='(insert directory for image files)';
jjffbb=dir([sdirectory '/*bmp']);

for i=1:length(jjffbb);
    filename=[sdirectory '/' jjffbb(i).name];
    I=imread(filename);
%originalImage = imread(imageFileNames{1});
J = undistortImage(I, cameraParams);
b=J;
    c=im2double(b);
    d=(395-299)*c+299;
    e=mat2gray(d);
imshow(e);
filename=sprintf('0228_Pulsated%d.bmp',i);
saveas(gcf,filename,'bmp');
end
end
```

2. General Heat Transfer Analysis Codes

```
function JetImpingement_01_0228
%           This script performs analysis on experimental images.
```

```
clear,clc
sdirectory='C:\Users\Michael Hamman\Documents\Experimental
Results\EXP022817\Pulsated Flow\Processed';
jjffbb=dir([sdirectory '/*bmp']);
%%  Preallocating matrices indices
ll=length(jjffbb);
ResultsA=zeros(ll,1);ResultsB=zeros(ll,1);ResultsC=zeros(11,1);ResultsD=zeros
(ll,1);ResultsF=zeros(11,1);ResultsG=zeros(ll,1);
beta1=zeros(ll,1);beta2=zeros(ll,1);beta3=zeros(ll,1);
beta4=zeros(ll,1);beta5=zeros(ll,1);beta6=zeros(ll,1);
T_m=zeros(ll,1);

Alpha=zeros(331);
Alpha_Span=zeros(ll,331);
HH_Nu=zeros(ll,331);
 %       Cropping of image to remove regions of noninterest
x1=0; x2=60; x3=113;x4=164; x5=214; x6=272; x7=331; y1=0; y2=331;
crop=[x1,x2,x3,x4,x5,x6,x7,y1,y2];
%%      Runs analysis on each image
for i = 1:length(jjffbb)
    filename =[sdirectory '/' jjffbb(i).name];
    Processed_Frame = imread(filename);
    pj1=size(Processed_Frame);
    pj2=pj1(1)*pj1(2);
    Alpha_Frame=rgb2gray(Processed_Frame);
    tt=1; T_fl=299.54; em_2=.932; T_ref=299.35;
%       Calls HT analysis function and provides function input
%       Function produces relevent output for further analysis and data
%       exporting
[Nu_FCG_m,Q_FCG_m, M_gen, M_rad,M_Nu_nc,Nu_FCG_p, Nu_CF,Nu_FC_p,T_mean]=
HT_Analysis_01_0228(Alpha_Frame,tt,T_fl,em_2, T_ref,crop,pj2);
%       Adds output parameters to arrays for saving
ResultsA(i)=Nu_FCG_m;   %Global Nu forced convection
ResultsB(i)=Q_FCG_m;
ResultsC(i)=M_gen;
ResultsD(i)=M_rad;
%               Area averaged span-wise Nu centered on nozzle columns
beta1(i)=Nu_CF(1);
beta2(i)=Nu_CF(2);
beta3(i)=Nu_CF(3);
beta4(i)=Nu_CF(4);
beta5(i)=Nu_CF(5);
beta6(i)=Nu_CF(6);

ResultsF(i)=M_Nu_nc;
ResultsG(i)=Nu_FCG_p;
Mem(:,:,i)=Alpha+Nu_FC_p(:,:);
Alpha=Mem(:,:,i);
T_m(i)=T_mean;

end
%%      Prepares parameters for exporting
Alpha_Mem=(1/length(jjffbb)).*Alpha;%       Time averaged Nu distribution
pp=ResultsA;
qq=ResultsB;
```

```
rr=ResultsC;
ss=ResultsD;
uu=ResultsF;
vv=ResultsG;

ww=beta1;
xx=beta2;
yy=beta3;
zz=beta4;
aaa=beta5;
bbb=beta6;
AFT=[vv,ww, xx, yy, zz, aaa,bbb,T_m];
filename_p='HT_Data_022817p';
filename_m='Nu_FC_P_022817p';

csvwrite(filename_m,Alpha_Mem);%        Saves time averaged Nu dist. for
further analysis
xlswrite(filename_p,AFT);%              Saves HT analysis parameters for data
analysis
end
```

Nusselt Number Analysis Function

```
%function [Q_FCG_m, M_gen, M_rad,M_Nu_nc,Nu_FCG_p,Nu_FC_p,T_mean,Nu_FCs] =
HT_Analysis_01(Alpha_Frame,tt,T_fl,em_2, T_ref,crop,pj2)%
function [Nu_FCG_m,Q_FCG_m, M_gen, M_rad,M_Nu_nc,Nu_FCG_p,
Nu_CF,Nu_FC_p,T_mean] = HT_Analysis_01_0228(Alpha_Frame,tt,T_fl,em_2,
T_ref,crop,pj2)
%               This function takes processed Infrared images and applies
%               heat transfer analysis.
%
%
%               Processed_Frame, tt, T_fl, emiss_2 are the processed image
frame,
%               and iteration number identification, coolant temp, and
%               emissivity of the under side of the target
%               surface(painted side opposite of the impingement
side)temperature required
%%      Assigns data to variable
a=Alpha_Frame;

%%      Cropping
b=a(90:420,235:565);
pj3=size(b); pj4=pj3(1)*pj3(2);%               to perform the analysis.
%%
%%variables
g= 9.81;
RT= 299.35; %room temperature
PL=3.03e-4;
Ap=PL^2;%m^2 pixel surface area
Af= pj4*Ap; %m^2 HT surface area of interest
L1=.12; %m
L2=0.1288; % m Voltage Drop Distance
AVD=L1*L2;
Perimeter= 4*PL;
Lc= Af/Perimeter;
Tinf_b=RT; % K Room temperature (mean below foil)
Sig=5.6703e-8; %Stefan Boltzman Constant
```

```
%em_f=.17; %Emissivity of foil
D=.00476; %m nozzle diameter
%%   Cropping for reducing computation, producing a square matrix for matrix
operations, dividing of experimental domain for analysis
x1=crop(1,1);x2=crop(1,2);x3=crop(1,3);
x4=crop(1,4);x5=crop(1,5);x6=crop(1,6);x7=crop(1,7);
y1=crop(1,8);y2=crop(1,9);

%%      Electrical and Flow Properties
I=49.28; %Amps
DV=.83; %Volts
%from table A15
k= 0.02625;
v= 0.00001655;
Pr= 0.7268;
%%      Converts to double precision
c=im2double(b);
%%      Assigns temperature value to grayscale
d=(395-299)*c+299;
%%      Creations equation inputs for matices
Tf=(d+T_ref)./2;                %Underside fluid temperature in degrees C
aa=mean(mean(Tf));
Beta=1/aa;                      %Expansion coefficient
T_dm=mean(mean(d));
Ra=(g*Lc^3*Pr/v^2)*Beta*(T_dm-T_ref);   %Rayliegh number
Nu_NC=.27*Ra.^.25;                  %Nu for Natural convection from the
underside of the foil
bb=Ap*k/Lc;
%%      Computes the natural convection heat flux
Q_NC=bb*(Nu_NC*(Tf-Tinf_b));
%%      Computes the radiation heat flux on the painted side of the target
plate
Q_Rad=em_2*Ap*Sig.*(d.^4-Tinf_b^4);
%%      Computes the thermal energy generation due to electrical power
dissipation
[rows,col]=size(b);
aaa=ones(rows,col);
bbb=rows*col;
Q_gen=I*DV*(Af/AVD);
Q_gen_p=(Q_gen/pj4)*aaa;
%%      Computes the forced convection heat transfer due to the impingement
cooling jets

Snc=sum(sum(Q_NC));
Srad=sum(sum(Q_Rad));
Q_FC=real(Q_gen-Snc-Srad);
Q_FC_p=real(Q_gen_p-Q_NC-Q_Rad);
%Q_FC=real(Q_GEN);

T_mean=mean(mean(d));
T_flmean=mean(mean(T_fl));

Nu_FC=((D/Af)/k)/(T_mean-T_flmean)*Q_FC;%       Global appproximation of Nu
Nu_FC_p=((D/Ap)/k)*Q_FC_p./(d-T_fl);
%       Area averaged Nu
Nu_FC_1=Nu_FC_p(1:(x2-x1),:);
```

```
Nu_FC_2=Nu_FC_p((x2-x1+1):(x3-x1),:);
Nu_FC_3=Nu_FC_p((x3-x1+1):(x4-x1),:);
Nu_FC_4=Nu_FC_p((x4-x1+1):(x5-x1),:);
Nu_FC_5=Nu_FC_p((x5-x1+1):(x6-x1),:);
Nu_FC_6=Nu_FC_p((x6-x1+1):(x7-x1),:);
Nu_FC_a1=mean(mean(Nu_FC_1));
Nu_FC_a2=mean(mean(Nu_FC_2));
Nu_FC_a3=mean(mean(Nu_FC_3));
Nu_FC_a4=mean(mean(Nu_FC_4));
Nu_FC_a5=mean(mean(Nu_FC_5));
Nu_FC_a6=mean(mean(Nu_FC_6));
Nu_CF=[Nu_FC_a1, Nu_FC_a2, Nu_FC_a3, Nu_FC_a4, Nu_FC_a5, Nu_FC_a6];
Nu_FCs=mean(Nu_FC_p);
%%      Creates output variables
Nu_FCG_m=sum(Nu_FC)/length(Nu_CF);    %Global mean forced convection Nu
Nu_FCG_p=mean(mean(Nu_FC_p));
Q_FCG_m=mean(mean(Q_FC));      %Global mean forced convection heat flux
M_gen=Q_gen;
M_rad=Srad;
M_Nu_nc=Nu_NC;
%Nu_FCG_max=max(max(Nu_FC));
end
```